Article
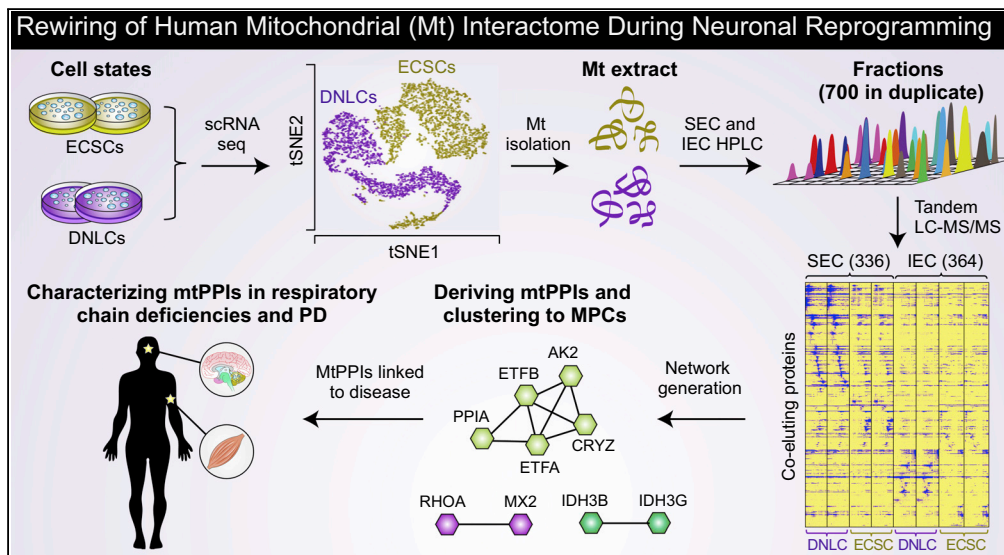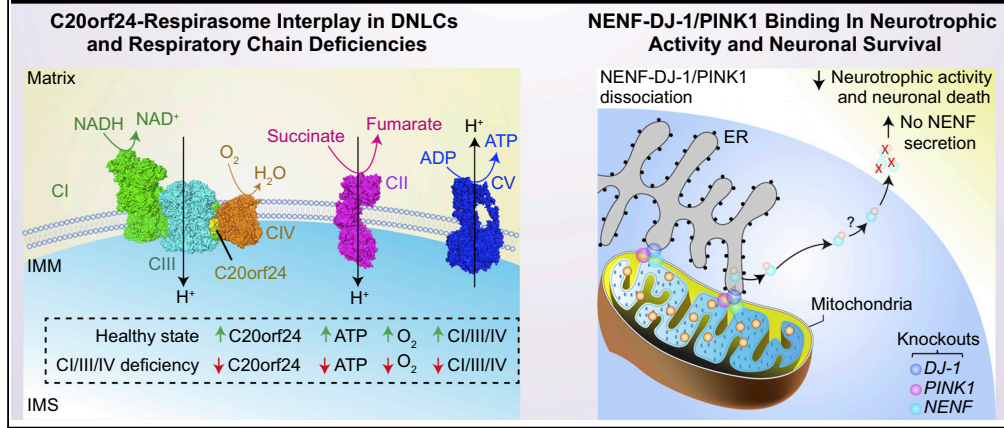
Rewiring of the Human Mitochondrial Interactome during Neuronal Reprogramming Reveals Regulators of the Respirasome and Neurogenesis

Rewiring of Human Mitochondrial (Mt) Interactome During Neuronal Reprogramming

New Mechanisms for Mt proteins in Respirasome, Neuronal function, and Mt Disease

Mohamed Taha
Moutaoufik, Ramy
Malty, Shahreen
Amin, ..., Gary D.
Bader, Francisco
S. Cayabyab,
Mohan Babu

mohan.babu@uregina.ca

HIGHLIGHTS

Rewiring of mitochondrial
(mt) protein interaction
network in distinct cell
states

Dramatic changes in site-
specific phosphorylation
during neuronal
differentiation

C20orf24 is a respirasome
assembly factor depleted
in patients deficient in CIV

NENF binding with DJ-1/
PINK1 promotes
neurotrophic activity and
neuronal survival

Article

Rewiring of the Human Mitochondrial Interactome during Neuronal Reprogramming Reveals Regulators of the Respirasome and Neurogenesis

Mohamed Taha Moutaoufik,[1,12] Ramy Malty,[1,12] Shahreen Amin,[1,12] Qingzhou Zhang,[1,12] Sadhna Phanse,[1] Alla Gagarinova,[2] Mara Zilocchi,[1] Larissa Hoell,[1] Zoran Minic,[1] Maria Gagarinova,[1] Hiroyuki Aoki,[1] Jocelyn Stockwell,[3] Matthew Jessulat,[1] Florian Goebels,[4] Kirsten Broderick,[1] Nichollas E. Scott,[5] James Vlasblom,[1] Gabriel Musso,[6] Bhanu Prasad,[7] Eleonora Lamantea,[8] Barbara Garavaglia,[8] Alex Rajput,[9] Kei Murayama,[10] Yasushi Okazaki,[11] Leonard J. Foster,[5] Gary D. Bader,[4] Francisco S. Cayabyab,[3] and Mohan Babu[1,13,*]

SUMMARY

Mitochondrial protein (MP) assemblies undergo alterations during neurogenesis, a complex process vital in brain homeostasis and disease. Yet which MP assemblies remodel during differentiation remains unclear. Here, using mass spectrometry-based co-fractionation profiles and phosphoproteomics, we generated mitochondrial interaction maps of human pluripotent embryonal carcinoma stem cells and differentiated neuronal-like cells, which presented as two discrete cell populations by single-cell RNA sequencing. The resulting networks, encompassing 6,442 high-quality associations among 600 MPs, revealed widespread changes in mitochondrial interactions and site-specific phosphorylation during neuronal differentiation. By leveraging the networks, we show the orphan C20orf24 as a respirasome assembly factor whose disruption markedly reduces respiratory chain activity in patients deficient in complex IV. We also find that a heme-containing neurotrophic factor, neuron-derived neurotrophic factor [NENF], couples with Parkinson disease-related proteins to promote neurotrophic activity. Our results provide insights into the dynamic reorganization of mitochondrial networks during neuronal differentiation and highlights mechanisms for MPs in respirasome, neuronal function, and mitochondrial diseases.

INTRODUCTION

Mitochondria (mt) are dynamic organelles crucial for a number of essential cellular functions in neurons, including oxidative phosphorylation (OXPHOS), neuronal differentiation, and synapse formation (Nunnari and Suomalainen, 2012). Disruptions of mt functions can cause neuronal degeneration, leading to rare inherited metabolic (e.g., complex IV [CIV] or cytochrome *c* oxidase deficiency) or neurodegenerative (e.g., Parkinson disease [PD]) disorders (DiMauro and Schon, 2008). In normally functioning neurons, mt are crucial for neurogenesis, a dynamic process in which neural stem cells differentiate into neurons via a neurogenic gene expression program (Khacho et al., 2018). Conversely, the decline in neurogenesis leads to cognitive impairment associated with various degenerative disorders, and impaired mt may contribute to such deterioration (Fernandez et al., 2019; Khacho et al., 2018); however, the underlying mechanisms triggering these changes are poorly understood.

Global changes in gene expression (Busskamp et al., 2014) and proteome dynamics (Frese et al., 2017) have been observed across various stages of neuronal development in multiple cell types. Large-scale protein-protein interaction (PPI) networks generated by several proteomic methods (Hein et al., 2015; Huttlin et al., 2017; Wan et al., 2015) from whole cell, nuclear, or cytosolic extracts have provided a glimpse of the stably associated human complexome in non-neuronal cells. Yet, the physiological functions of mt proteins (MPs), as well as the organization of the full repertoire of cell-context-dependent, native human mtPPIs and resulting multiprotein complexes (MPCs) before and after neuronal differentiation are far from complete.

Accumulating evidence suggests that post-translational modifications (PTMs), including phosphorylation or dephosphorylation, regulate many aspects of mt processes (Grimsrud et al., 2012). Mass spectrometry

[1]Department of Biochemistry, University of Regina, Regina, SK S4S 0A2, Canada

[2]Department of Biochemistry, University of Saskatchewan, Saskatoon, SK S7N 5E5, Canada

[3]Department of Surgery, Neuroscience Research Group, College of Medicine, University of Saskatchewan, Saskatoon, SK S7N 5E5, Canada

[4]The Donnelly Centre, University of Toronto, Toronto, ON M5S 3E1, Canada

[5]Department of Biochemistry and Molecular Biology, University of British Columbia, Vancouver, BC V6T 1Z3, Canada

[6]Department of Medicine, Harvard Medical School and Cardiovascular Division, Brigham and Women's Hospital, Boston, MA 02115, USA

[7]Department of Medicine, Regina Qu'Appelle Health Region, Regina, SK S4P 0W5, Canada

[8]Medical Genetics and Neurogenetics Unit, Fondazione IRCCS Instituto Neurologico Carlo Besta, via L. Temolo, 4, 20126 Milan, Italy

[9]Department of Medicine, Division of Neurology, College of Medicine, University of Saskatchewan, Saskatoon, SK S7N 5E5, Canada

(MS)-based proteomics has allowed the identification of the human mt proteome that is phosphorylated, as well as mt kinases that phosphorylate a number of different cellular protein substrates, and enabled the monitoring of changes in the phosphoproteome of human embryonic stem cells upon differentiation (Grimsrud et al., 2012; Van Hoof et al., 2009). Although these efforts in tissues and cell lines have enhanced our knowledge of the regulation of human proteins by PTMs, much remains to be learned about alterations in phosphorylation during neuronal differentiation. This includes how phosphorylation sites are distributed within MP complexes and which sites are targeted by mt kinases during neuronal differentiation.

Here, we address these gaps by performing an extensive biochemical fractionation (BF) with in-depth MS profiling in both mt extracts of cultured human NTera2 embryonal carcinoma stem cells (ECSCs or undifferentiated state) and retinoic acid (RA)-induced differentiated neuronal-like cells (DNLCs), two cell populations differentiable using single-cell RNA sequencing (scRNA-seq). The resulting network reveals that the majority of observed native mtPPIs were previously unreported and undergo considerable changes upon differentiation. Also, phosphoproteome characterization in the mt extracts from ECSCs and DNLCs shows a sizable fraction of MPs to be phosphorylated at serine residues and that the activity of mt pyruvate dehydrogenase E1α 2 subunit (PDHA2), phosphorylated on S291/S293 residues in ECSCs, is increased in DNLCs via dephosphorylation.

By leveraging the high-quality mtPPI network, we provide evidence that the orphan MP C20orf24, which has a less frequent heterozygous 3′ UTR variant in patients with mt respiratory chain deficiencies, functions as an assembly factor, causing a marked reduction in respirasome levels when disrupted. As well, we establish that the binding between a neuron-derived neurotrophic factor (NENF) and the PD-associated proteins (DJ-1/PARK7, PINK1), required for loading heme from mt, enhances neurotrophic activity to promote neuronal survival. Overall, this experimentally derived catalog of human mtPPIs assembled during the reprogramming of ECSCs to DNLCs will enhance our understanding of the functional significance of the mt in the intricate process of human neurogenesis and in the manifestation of mt diseases.

RESULTS

BF/MS Co-elution Profiles from mt Extracts of NTera2 ECSCs and RA-Induced DNLCs

To establish a map of native human mt macromolecular assemblies involved in neurogenesis, we applied our BF/MS strategy (Havugimana et al., 2012) to mt extracts isolated from chemically cross-linked (i.e., dithiobis-succinimidyl propionate, which allows identification of weak or transient PPIs; Malty et al., 2017) cultures of NTera2 ECSCs and DNLCs (Figure 1A). This human cell line was chosen because it is widely used in the study of neurogenesis and neurodegenerative disorders as an attractive progenitor that retains many human embryonic stem cell features, with the capacity to generate DNLCs (Gonzalez-Burguera et al., 2016). Besides confirming the expression of stemness and/or neuronal markers in ECSCs and DNLCs by immunoblotting (Figure 1B), immunofluorescence assays exhibited typical neuronal morphology for TAU-positive axons and MAP2-positive dendrites in DNLCs (Figures S1A and S1B).

We next assessed the global changes in transcriptome profiles during differentiation by performing bulk RNA sequencing (RNA-seq) in biological triplicates from ECSCs and DNLCs. The average correlation of transcriptomic profiles between replicates in each cell state was high ($r = 0.99$; Figure S1C), indicating good reproducibility. In total, we found that 10% (1,889) of the total transcripts (19,587) in DNLCs were significantly ($q \leq 0.01$; Table S1) altered with a more than 2-fold change in expression when compared with ECSCs, resulting in 1,176 downregulated and 713 upregulated genes. Key pluripotency (*POU5F1*, *POU2F1*, *NANOG*, *TDGF1*, *LIN28A*) and stem cell maintenance (*SOX2*, *SOX5*) genes were downregulated, whereas neuronal cytoskeletal elements (*NEFM*, *TUBB3*) or regulators of neural precursors (*PAX6*, *NYAP2*, *NRN1*) exhibited an increase (3.4- to 8.1-fold, $q = 4.5 \times 10^{-2}$ to 1.7×10^{-6}) in transcription (Figure 1C). These events suggest that NTera2 cells can faithfully model *in vivo* neuronal differentiation.

As incomplete differentiation from ECSCs to DNLCs or other causes of cell heterogeneity within a population of DNLCs can confound observation of interactions that are cell type specific, we performed scRNA-seq on live DNLCs relative to ECSCs and examined the gene expression dynamics of individual subpopulations. After processing the cells for quality control (see Transparent Methods), the sequenced data showed an average depth of 76,473 reads per cell and detected a median of 3,831 genes per cell. Cells analyzed in a two-dimensional t-distributed stochastic neighbor embedding (Figure 1A) plot showed a

[10]Department of Metabolism, Chiba Children's Hospital, 579-1 Heta-cho, Midori, Chiba 266-0007, Japan

[11]Graduate School of Medicine, Intractable Disease Research Center, Juntendo University, Hongo 2-1-1, Bunkyo-ku, Tokyo 113-8421, Japan

[12]These authors contributed equally

[13]Lead Contact

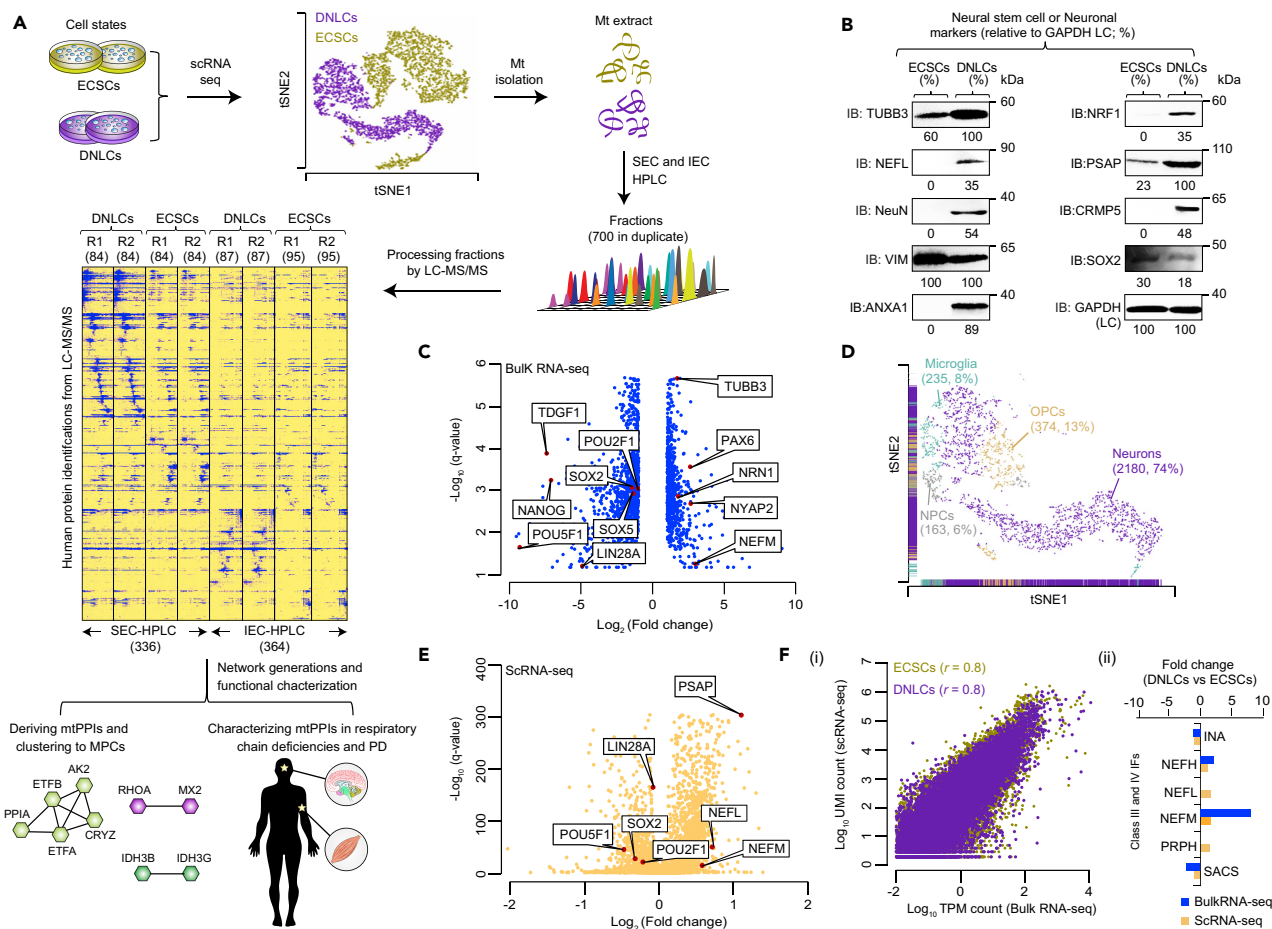*Correspondence: mohan.babu@uregina.ca

Figure 1. Experimental Workflow and Characterization of Cell States

(A) BF/MS methodology to identify mtPPI changes (Tables S2 and S3) in ECSCs and DNLCs, which was characterized by scRNA-seq showing clear cell state separation by t-SNE (t-distributed stochastic neighbor embedding) plot. Heatmaps of co-eluting protein profiles of SEC- or IEC-high-performance liquid chromatography recorded by MS (unique peptide counts in blue) in duplicate experiments of each cell state. Numbers in parentheses indicate total fractions from each technique.

(B) Immunoblotting (IB) showing the expression of indicated stemness/neuronal markers with respective protein-specific antibodies in ECSCs and DNLCs.

(C and E) Volcano plots representing significant transcripts altered in DNLCs over ECSCs. Red dots indicate significantly up- or downregulated genes in DNLCs. Fold change was determined based on average TPM (transcripts per million; C) or UMI (unique molecular identifier; E) counts for each significant transcript in DNLCs over ECSCs. Q-value, false discovery rate (corrected by Benjamini-Hochberg)-adjusted p value.

(D) t-SNE plot of 2,952 DNLCs, annotated by cell type identity. OPC, oligodendrocyte precursor cells; NPC, neural progenitor cells.

(F) Scatterplot of $\log_{10}$ values (TPM or UMI counts) of all genes in each cell state (i), and transcriptional changes (fold change; DNLCs versus ECSCs) for classes III and IV intermediate filament (IF; ii) genes measured in RNA-seq and scRNA-seq.

See also Figure S1 and Table S1.

clear separation of cell states as two discrete populations, with 3,631 single cells from ECSCs and 2,952 from DNLCs.

Although RA exposure to ECSCs essentially facilitates irreversible differentiation, like any other differentiated cell lines, NTera2 DNLCs contain a mixed populations of neurons and other cell types. We therefore used previously described marker genes (Lake et al., 2016; Zhong et al., 2018) to predict cell type identity for all DNLCs, resulting in four transcriptionally distinct clusters (Table S1). Our analysis showed that three-fourths (2,180, 74%; Figure 1D) of the cells within the DNLCs correspond to the neuronal cell type (at 95% confidence by hypergeometric test); the rest identified as microglia (235, 8%), oligodendrocyte precursor (374, 13%), or neural progenitor (163, 6%) cells, suggesting that the interactions we identify in DNLCs will tend to be characteristic of the neuronal cell type.

We then performed differential gene expression analysis between DNLCs and ECSCs and identified 7,023 genes with significant ($q \leq 0.01$; Table S1) differences in expression in DNLCs (4,503 upregulated and 2,520 downregulated) when compared with ECSCs (Figures 1E and S1D). As for marker genes from immunoblotting or RNA-seq for ECSCs and DNLCs (Figures 1B and 1C), the overall average expression level of single cells correlated well ($r = 0.8$) with the bulk cell populations (Figure 1F). An illustrative example is the involvement of an ARSACS (autosomal recessive spastic ataxia of Charlevoix-Saguenay)-causing *SACS* gene in the regulation of class III (*PRPH*) and IV (*NF-L/M/H*; *INA*) intermediate filament genes expressed in neurons (Gentil et al., 2019). Consistent with this observation, bulk RNA-seq and scRNA-seq showed an increased expression of classes III and IV genes in DNLCs, except *SACS* and *INA*, which exhibited decreased expression (Figure 1F), revealing a cell type-specific outcome.

After confirming morphological and transcriptional changes as expected in ECSCs and DNLCs, we sought to co-fractionate the stably interacting proteins by performing BFs using complementary size-exclusion and ion-exchange chromatographic (SEC, IEC) separation techniques (Figure 1A). A total of 700 distinct fractions were collected in duplicate from the cross-linked mt extracts of four fractionation experiments (two ECSCs, two DNLCs). These fractions were then subjected to MS to define MP complex membership. Examination of the co-elution profiles and average correlation of proteins (peptide counts) detected by MS between replicate experiments suggested high reproducibility ($r = 0.99$; Figures 1A and S2A). As expected, elution profiles were also consistent with average molecular weights and isoelectric points by SEC and IEC methods (Figure S2B), respectively, reinforcing the utility of BF/MS approach.

Scoring and Validating Human mtPPIs in ECSCs and DNLCs

To generate high-quality mtPPIs in each cell state, the tandem MS spectra from each replicate chromatographic fraction was searched against reference human protein sequences using Sequest and several alternate search engines (X! Tandem, MS-GF+, Comet) to increase the sensitivity and accuracy of peptide identification. The resulting peptide-spectral matches were integrated into a single probability score using MSblender (Kwon et al., 2011) and then filtered to a 0.1% protein-level false discovery rate, with two or more distinct peptides used to define human proteins that reliably co-elute in each fraction. The chromatographic profiles of proteins co-eluted across collected fractions from both replicates were measured using three complementary scoring procedures (Pearson correlation coefficient, weighted cross-correlation, co-apex score, Havugimana et al., 2012) to identify pairwise protein associations. To maximize coverage and accuracy (Figure S2C), we integrated the correlation and co-apex scores from different separation techniques into a single unified log likelihood score (LLS) for each putatively interacting protein pair in ECSCs (ΣLLS_{ECSCs}) and DNLCs (ΣLLS_{DNLCs}), respectively.

High-confidence mtPPIs for each cell state were derived by eliminating associations below a stringent cutoff ($\Sigma LLS \leq 1.45$), where most of the reference mtPPIs curated in CORUM human protein complexes (Ruepp et al., 2010) were recovered, as evaluated using area under the receiver operating characteristic curve (Figure 2A). After employing an appropriate threshold, we considered as physiologically relevant the interactions between MPs, and between the cytosolic and outer mt membrane (OMM) proteins (Walther and Rapaport, 2009), for defining two static mtPPI networks. These included 3,320 interactions (2,973 between MPs; 347 between cytosolic and OMM) among 408 unique human MPs in ECSCs and 3,567 (3,233 between MPs; 334 between cytosolic and OMM) interactions among 467 MPs in DNLCs, covering 36% (600 of 1,672 MPs) of the estimated human mt proteome (Table S2).

In addition to confirming the physical associations observed in previous large-scale interaction studies in humans and other metazoans (Floyd et al., 2016; Havugimana et al., 2012; Hein et al., 2015; Huttlin et al., 2017; Liu et al., 2018; Malty et al., 2017; Schweppe et al., 2017; Wan et al., 2015) or small-scale biochemical experiments (BioGRID), we found that most of the mtPPIs in ECSCs (3,086, 93%) and DNLCs (3,199, 90%) had not been previously reported (Figure 2B). Notably, these PPIs encompassed an order of magnitude more MPs (Figure S2D) than our recent study (Malty et al., 2017) performed in differentiated SH-SY5Y human neuronal cells. The overall reliability, data quality, and biological relevance of mtPPIs in the filtered static (ECSCs, DNLCs) networks was further assessed by composites of various experimental and computational sources (Figure 2C; Table S2). Half (1,745, 53% in ECSCs; 2,014, 56% in DNLCs) of our observed interactions were verified in other cell types and/or mouse brain, or by independent experimental evaluation. These include mtPPIs supported by (1) immunoprecipitation (IP) combined with MS (IP/MS) using protein-specific antibodies in the NTera2 or SH-SY5Y DNLCs or mouse brain, (2) BF/MS in mouse brain or in both
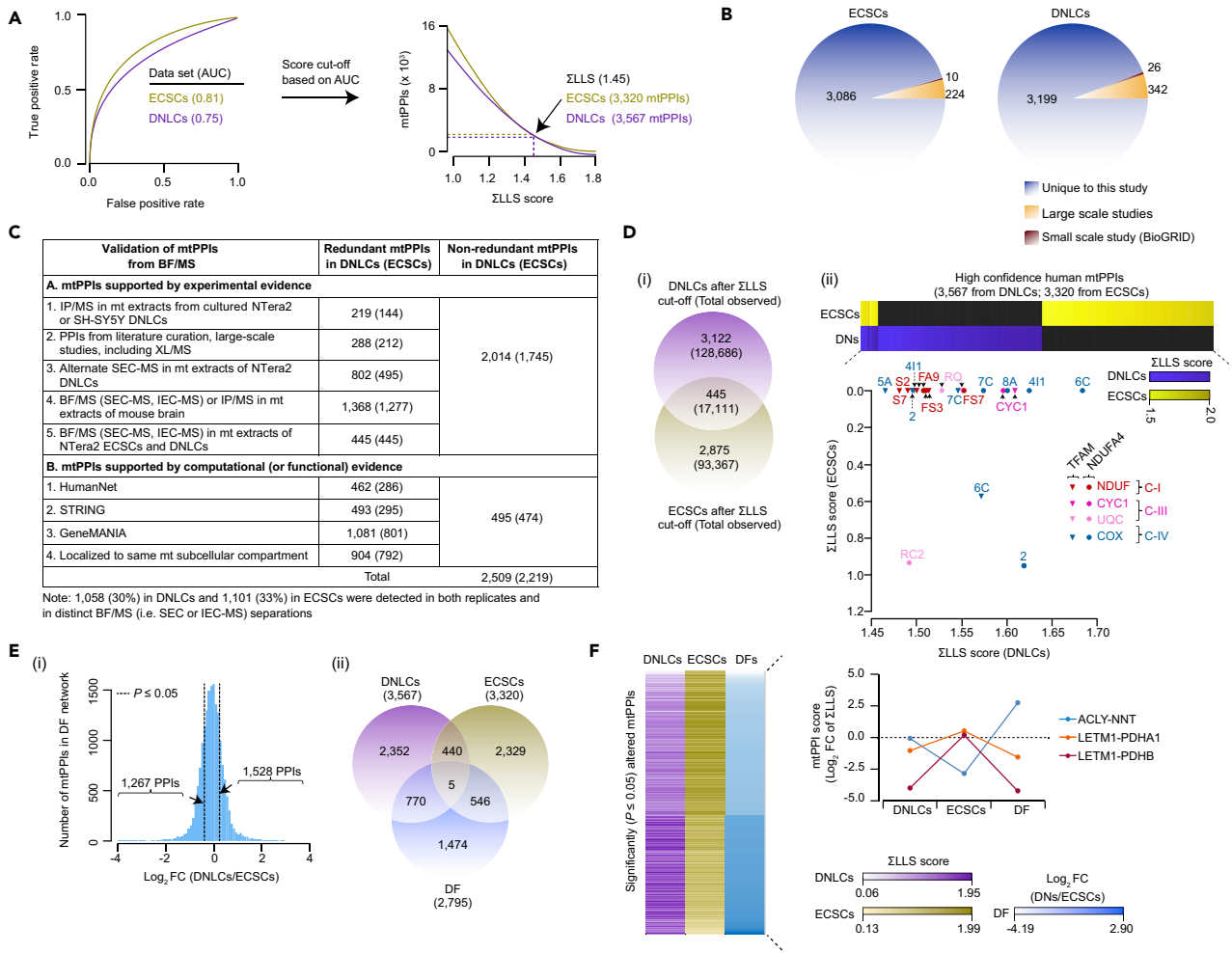
Figure 2. Benchmarking and Remodeling of mtPPIs in ECSCs and DNLCs

(A) Performance measures using AUC (area under the receiver operating characteristic curve) analysis based on estimates of true- and false-positive rates for scored mtPPIs against reference CORUM protein complexes containing mtPPIs (top). Cumulative ΣLLS score (bottom; threshold based on AUC) was computed by combining LLS score derived from SEC and IEC fractions.

(B) Overlap of high-confidence mtPPIs from ECSC and DNLC networks against the large- or small-scale (curated in BioGRID database) studies.

(C) Experimental and computational evidence supporting mtPPIs from each cell state.

(D) High-confidence (and total) mtPPIs common or specific to ECSC or DNLC networks (i). Association of CI subunit (NDUFA4) or TFAM with the components of the respirasome (ii) along with their ΣLLS scores in two static networks.

(E) Z score distribution (i) of $\log_2$ fold change (FC) for differential (DF) PPIs filtered at p value $\leq$ 0.05 ($|Z\ score| \geq 1.96$) with tails indicating significant interactions. Venn diagram (ii) showing the overlap of significant mtPPIs in static and DF networks.

(F) Heatmap displaying significantly altered mtPPIs during differentiation (left) is shown with illustrative examples (right) for static and DF profiles.
See also Figures S2 and S3, and Table S2.

NTera2 cell states, (3) alternate SEC separation and MS in NTera2 DNLCs, and (4) previous high-throughput or literature-curated interaction reports (withholding PPIs from CORUM reference set).

The validity of the remaining mtPPIs from BF/MS was further independently verified by computational approaches. Specifically, less than one-quarter (474, 14% in ECSCs; 495, 14% in DNLCs) of our interactors have shared functional associations predicted in HumanNet (Lee et al., 2011), STRING (Szklarczyk et al., 2017), or GeneMANIA (Warde-Farley et al., 2010), or are known or predicted to localize to the same mt subcellular compartment. Altogether, two-thirds (2,219, 67% in ECSCs; 2,509, 70% in DNLCs) of the total, non-redundant physical associations confirmed by these experimental or computational sources are consistent with the validation rates seen for human soluble PPIs (Havugimana et al., 2012).

When benchmarked against literature-curated interactors (CORUM), the performance measures of our mtPPI networks (using 5-fold cross-validation) showed high sensitivity and specificity (Figure S2E), when compared with previous human interaction datasets (Floyd et al., 2016; Havugimana et al., 2012; Hein et al., 2015; Huttlin et al., 2017; Wan et al., 2015). The putative interacting MPs were also significantly ($4.7 \times 10^{-64} < p < 1.9 \times 10^{-59}$) enriched for shared phenotypic annotations and higher ($7.0 \times 10^{-52} < p < 1.0 \times 10^{-14}$) functional coherence and similarity (based on Gene Ontology annotations) compared with existing large-scale PPI studies (Figure S3A). The ranked list of mtPPIs within the top or bottom 20th percentile of ΣLLS scores showed significant ($5.3 \times 10^{-46} < p < 2.6 \times 10^{-33}$) enrichment for membership in the same CORUM protein complex (Figure S3B), indicating that the subunits of these complexes were more likely to co-elute in the same biochemical fractions. MP interactors also tended to show enrichment ($3.0 \times 10^{-6} < p < 5.0 \times 10^{-2}$) for shared Pfam domains (Figure S3C; Table S2). This includes the cytochrome b_5 domain-containing proteins that function as electron carriers for membrane-bound oxygenases, and the heat shock protein (HSP70, HSP90) domain families involved in proteostasis and quality control. Finally, stably interacting proteins that co-fractionated together were strongly ($6.7 \times 10^{-131} < p < 2.2 \times 10^{-14}$; Figure S3D) co-expressed or co-translated in NTera2 (ECSCs, DNLCs) or mouse brain (Sharma et al., 2015; Zhang et al., 2014) and exhibited significantly ($8.4 \times 10^{-71} < p < 5.6 \times 10^{-42}$) positively correlated mRNA co-expression profiles (Figure S3E) in human cortical neurons (van de Leemput et al., 2014). These findings suggest a propensity of mtPPIs to have coordinated expression in neurons or brain regions.

mtPPI Network Reflects Dynamic Changes in NTera2 ECSCs and DNLCs

Although the putative physical interactions observed in both networks appeared to be corroborated by transcriptional evidence (Figure S3F), the two interaction networks were markedly different at our chosen ΣLLS threshold. Specifically, there were more mtPPIs unique to each cell state (3,122 in DNLCs; 2,875 in ECSCs) than shared in common (Figure 2D). For example, binding of the mt-encoded NADH dehydrogenase transmembrane subunit of the respiratory complex I [CI] (NDUFA4) with its members (NDUFA9, FS3, FS7), as well as with the constituents of complex III [CIII] (CYC1, UQCRC2, UQCRQ) and complex IV [CIV] (COX2, 4I1, 6C, 7C, 8A) in DNLCs supports the notion that NDUFA4 may coordinate its function as an assembly factor for respirasomes (Kadenbach, 2017) during neuronal differentiation. Similarly, the association of mt transcription factor A (TFAM) with the subunits of respiratory complexes lends support to the suggestion that TFAM regulates the respiratory chain function as it is required for the expression of the components of mt complexes (Larsson et al., 1998; Masand et al., 2018). The transitioning of mtPPIs during differentiation was further supported by the high degree of connectivity ($\geq$ 50 PPIs) of MPs that participate in mt pathways, including respiration and metabolism (Figure S4A). As these findings imply highly differential underlying networks, we next examined the validity of these observed differences.

To characterize the changes in mtPPI networks between cell states, we constructed a differential (DF) network by computing a fold change for each protein pair using the ΣLLS score from DNLCs relative to ECSCs (ΣLLS$_{DNLCs}$/ΣLLS$_{ECSCs}$). Given that DF interactome mapping can identify interactions that undergo alterations reliant on cell or tissue type, conditions, and disease state or other variants (Hosp et al., 2015; Ideker and Krogan, 2012), we focused on stringently identified differences. Based on the null distribution of the scored data, we applied thresholds corresponding to two standard deviations ($p \leq 0.05$), resulting in 2,795 mtPPIs that were significantly DF in ECSC- or DNLC-specific function (Figure 2E; Table S2). Half (51%, 1,528) of the DF mtPPIs with low ΣLLS scores in the static ECSC network became pronounced in DNLCs upon RA induction (Table S2). After filtering the significant DF network with a fold change cutoff of 2.0, 225 MP pairs were identified as likely to interact in one network but unlikely in the other (Figure 2F). For example, a high-confidence (6.9-fold) physical association between nicotinamide nucleotide transhydrogenase and ATP-citrate lyase in the DF network was reconcilable with the prediction from STRING, which suggested a functional link based on the role of these proteins in glutamine metabolism (Alberghina and Gaglio, 2014). In contrast, interaction (1.6- to 4.2-fold) between the inner mt membrane (IMM) protein (LETM1) and the mt matrix pyruvate dehydrogenase (PDH) complex subunits (PDHA1, PDHB) in ECSCs indicates that a physical coupling of these proteins may be relevant to glucose metabolism (Durigon et al., 2018; Jiang et al., 2013). These patterns in the alterations of mtPPIs in distinct cell states further suggest that many testable mechanistic hypotheses can be mined from the static or DF networks.

As proteins that associate physically tend to have similar biological functions (Oliver, 2000), the mtPPI networks from both cell states were examined to gain insight into the roles of orphan MPs (i.e., those with unclear biological significance) based on their association with annotated components. We found seven

orphans in the high-confidence static networks to be connected through 132 associations. The number of PPIs identified for each orphan in the mt networks also varied considerably, ranging from 1 (e.g., C1orf64) to 53 (e.g., C20orf24), with many MPs in the DN network interacting with an orphan protein. Among the 132 PPIs with orphan proteins, nearly three-fourths (94, 71%) were altered in response to RA-induced neuronal differentiation (Figure S4B). Overall, these observations show wide reprogramming of mtPPIs during neuronal differentiation, vastly expanding the existing mt interactome.

Endogenous MPCs Are Altered during Neuronal Differentiation

Given that the topological analysis of the PPI network can reveal clusters of densely connected proteins, we examined how macromolecular protein assemblies are reconfigured in response to RA-induced differentiation. As seen for scale-free PPI maps (Havugimana et al., 2012; Malty et al., 2017), interacting proteins in the DNLC network followed a power-law distribution, with most proteins associated to each other within five or fewer degrees of separation (Figure S4C).

To systematically define complex membership in the static DNLC network, we employed the coreMethod (Leung et al., 2009), Markov clustering (Enright et al., 2002), and ClusterONE (Nepusz et al., 2012) algorithms. Comparison of the resulting protein clusters from each of the clustering methods to the literature-curated training set of protein complexes in CORUM showed that clusters generated using the coreMethod overlapped more substantially ($p = 1.3 \times 10^{-13}$) with known complexes (Figure S4D), and as a result, we focused on the coreMethod clusters from this point forward. The coreMethod produced 139 putative multiprotein groupings with at least one MP, including 72 heterodimers (Figure 3; Table S3). Proteins interacting in one-fourth (32, 23%) of these complexes derived from DNLCs also existed in ECSCs (Table S3), whereas one-third (40, 30%) matched the reported CORUM assemblies. The remaining 99 putative complexes have not been previously characterized (Figure S4E), signifying a valuable resource for exploring the mechanistic basis of the interactions in biological contexts.

We then interrogated the 139 MPCs by comparing them with two recent mt interactome maps generated in mouse tissues by cross-linking MS (Liu et al., 2018; Schweppe et al., 2017). Through ortholog mapping we identified 55 unique cross-linked interacting protein pairs in mouse that map to 13 of our identified MPCs (Table S3). For example, 27 mouse interactors were observed in the human mt respirasome complexes (CI/III/IV); however, the association of mt fatty acid β-oxidation of 3-hydroxyacyl-CoA dehydrogenase (HADHA, B) with these complexes, which is consistent with the related role of fatty acid β-oxidation protein products in OXPHOS complex biogenesis (Lim et al., 2018), has not been previously observed in DNLCs. Similarly, the cross-linking performed in mouse tissues connected mt glutamate oxaloacetate transaminase (GOT2) and malate dehydrogenase in DNLCs (MDH2), supporting their role in malate-aspartate shuttling for energy production (Yang et al., 2015). Although the mechanism behind the interactions remains to be determined, these results suggest that the cross-linked associations from mouse were enriched in orthologs to human proteins in close spatial proximity, and are generally consistent with the limited MPC relationships observed in the DNLC network.

Because MPC subunits with correlated interaction profiles can not only lend additional evidence for predicted MPCs but also predict functional relationships between proteins (Han et al., 2017), we calculated the correlation of interaction partners between all possible pairs of proteins present in the static ECSC and DNLC networks. Consistent with the shared functionality implied by their co-grouping, the interaction profiles for proteins within the same complexes in ECSCs or DNLCs were found to be significantly ($p < 1.3 \times 10^{-86}$ to $p < 1.9 \times 10^{-7}$) more positively correlated on average than protein pairs associated between complexes (Figures S5A and S5B). Interaction profile correlations also revealed many significantly ($p \leq 0.05$) positively correlated protein pairs of the same complex to be involved in both cell states (Figures 3 and S5A). This includes the strong correlation ($r = 0.4–0.9$; Table S3) between the mt electron-transferring flavoprotein partners (ETFA, ETFB) that shuttle electrons to coenzyme Q (complex 34), as well as between the components of mt voltage-dependent anion channel (VDAC1, 2, 3) and protein translocases (TOMM5, TOMM40; complex 1), consistent with the requirement of TOMM in VDAC import (Kozjak-Pavlovic et al., 2007). Conversely, we also found positively correlated interaction profiles for MPC subunits that are preferentially detected in DNLCs (Table S3). An illustrative example is the highly correlated ($r = 0.9$) interaction profiles between the isocitrate dehydrogenase complex subunits (IDH3B, IDH3G; complex 73), as well as the positively correlated ($r = 0.9$) interacting protein profiles observed between the poorly characterized
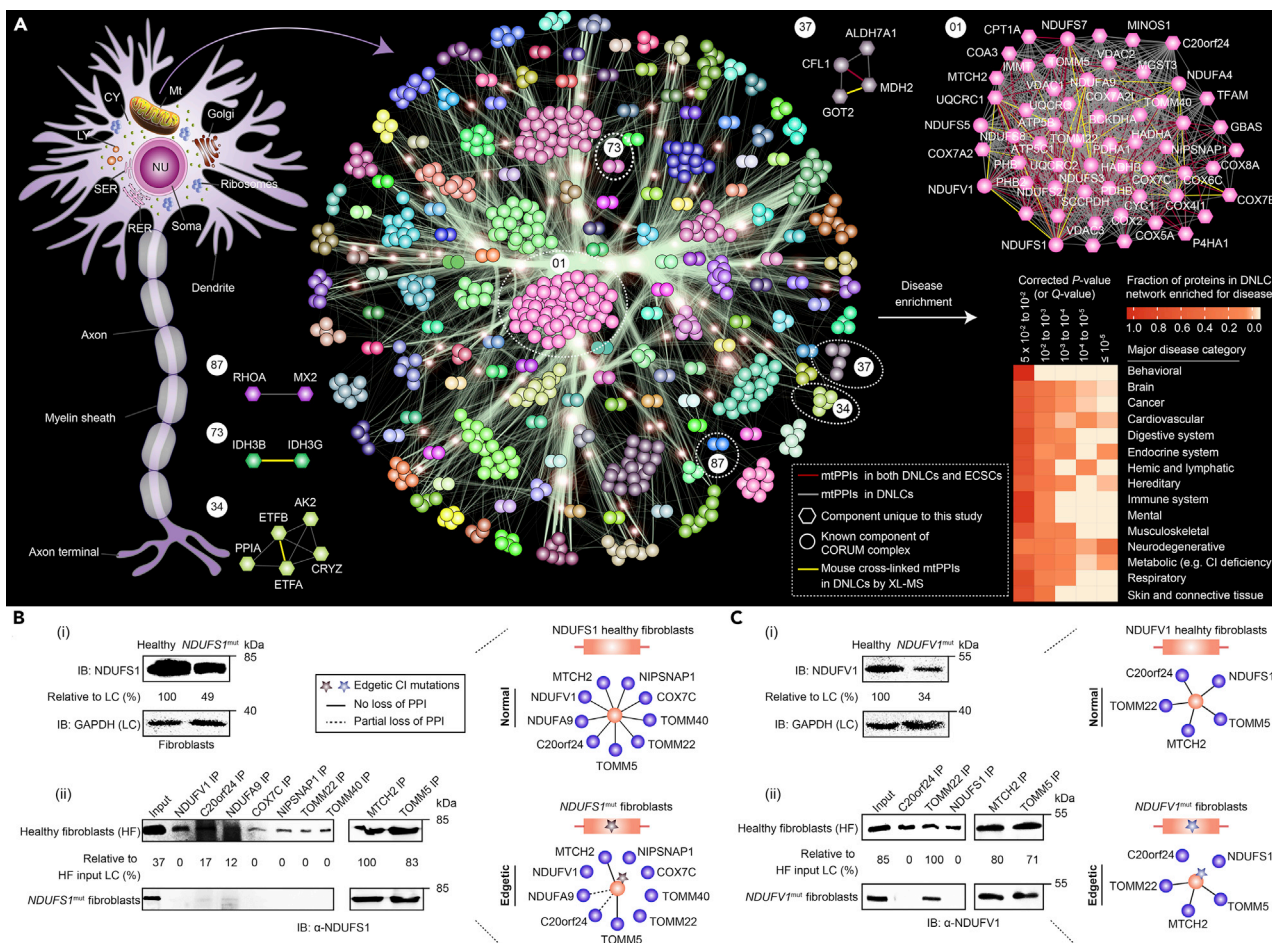
Figure 3. Human mt MPCs in DNLCs and Their Interacting Proteins to CI Deficiency

(A) Schematic of the putative MP assemblies and representative MPCs are indicated using different colored circles, and mtPPIs (edges or lines) present in both cell states (red) and specific to DNLCs (gray) are shown along with those identified by cross-linking (XL)-MS (yellow) in different mouse tissues; hexagonal nodes are unique to this study, and circles are known component of a CORUM complex. CY, cytoplasm; SER and RER, smooth and rough ER, respectively; LY, lysosome. Enrichment of mtPPIs from DNLC network linked to human diseases; false discovery rate (Benjamini-Hochberg correction)-adjusted p value (or Q-value) of the hypergeometric test.

(B and C) NDUFS1 (B-i) or V1 (C-i) levels and perturbation of select PPI pairs in the fibroblasts of healthy individual and CI-deficient subject with *NDUF* mutations (B-ii, C-ii) immunoblotted (IB) with anti-NDUFS1 or VI antibody. Band intensities were normalized to GAPDH or healthy fibroblast (HF) input loading control (LC). Molecular masses (kDa) of marker proteins are indicated.

See also Figure S4 and Table S3.

small RhoGTPase (RhoA) and MX dynamin-like GTPase (MX2; complex 87). These observations suggest that the protein pairs may have functions in neuronal processes.

MPCs in DNLCs Reveal Interactions Linked to CI Deficiency and Other mt Disorders

Disease-associated alleles have been observed in the binding interface of interacting proteins, with disruption of protein associations cited as leading to disease progression (Sahni et al., 2015). We therefore examined the DNLC network to identify the interacting subunits of MPCs relevant to human diseases. Over half (267, 57%) of MPs that make up the interactions in the MPCs have links to a spectrum of mt disorders with ~300 known disease-causing genes (Kremer et al., 2017) and are significantly enriched ($p < 1 \times 10^{-5}$ to $p < 5 \times 10^{-2}$) for multiple human disease annotations from DisGeNET (Pinero et al., 2017). One notable enrichment was the interacting proteins with associations to CI deficiency (Figure 3A), a rare inborn error of metabolism due to mutations in nuclear (or mt) genes encoding subunits of the human mt CI.

As an MPC consisting of CI subunits, *NDUFS1* and *V1,* was highly connected to 46 putatively interacting proteins in the DNLC network, we examined the potential relevance of these interactions to CI deficiency in isolated skin fibroblasts from CI-deficient children carrying pathogenic mutations (Transparent Methods) in *NDUFS1* and *V1* alleles. Although *NDUF* mutants were expressed at modest levels in the fibroblasts of patients with CI, their mutations perturbed two-thirds (9, 64%) of all (14) high-scoring tested interactions in the CI patient fibroblasts (Figures 3B and 3C). For example, mutation in the *NDUFS1* gene disrupted its interactions with OMM import receptors (*TOMM22*, *40*), consistent with the functional dependency between mt import and respiratory chain machineries (Kulawiak et al., 2013). As well, *NDUFS1* or *V1* mutations abrogated the ability of these genes to bind the subunits of CI and CIV, supporting the idea that mutations in the CI gene products may affect respirasome assembly (Floyd et al., 2016). Overall, our results suggest that known CI mutations preferentially induce edgetic perturbations.

Phosphorylation within the MPC Reveals Cell State-Specific Differences

PTMs such as phosphorylation of serine (pS), threonine (pT), and tyrosine (pY) modulate numerous functions, including for MPs involved in MPC formation, facilitation or disruption of PPIs, induction or elimination of enzyme activities, and alteration of protein conformations (Huttlin et al., 2010). We therefore hypothesized that there should be dramatic changes in site-specific phosphorylation before and after differentiation. To test this hypothesis, we surveyed the phosphorylation dynamics in mt extracts isolated from the cultured ECSCs and DNLCs, respectively. Phosphopeptides were enriched based on immobilized metal-affinity chromatography and titanium dioxide-metal oxide affinity chromatography, run in triplicate, and were then analyzed using high-resolution MS. The average correlation (r = 0.8) of phosphoproteome replicate experiments was high, and replicates were appropriately clustered by their cell state and phosphopeptide enrichment methods (Figure 4A).

After applying the Ascore algorithm with a confidence cutoff of 95% (Ascore $\geq$ 13), and retaining phosphorylated residues detected in two of the three replicates or in PhosphoSitePlus (a public protein phosphorylation repository; Figure 4B), we observed a total of 185 non-redundant phosphosites in 81 mt phosphoproteins (from a total of 190 mt phosphoproteins detected before filtering) that were localized to 121 serines, 40 threonines, and 24 tyrosines (Figure 4C). About one-quarter (38, 21%) of the phosphosites from ECSCs or DNLCs were enriched (q $\leq$ 0.05) for disease annotations including cancer, metabolic syndrome, neurological or neurodevelopmental disorders, and cardiomyopathy (Figure 4D; Table S4). Among the detected phosphosites, 30 were not previously described, and of the rest (155, 84%) that were found in the PhosphoSitePlus database, a majority (148, 95%; Table S4) have not been reported in the cell states we examined.

Most (156, 84%) of the phosphosites examined were also found to be altered between ECSCs and DNLCs (Figure 4C; Table S4). These include DN-specific phosphorylation on proteins involved in synaptic function (PSEN1 at S367), signaling (PRKACA at T198), and OXPHOS (ATP2A2 at S663, Y867). Conversely, we found several proteins to be phosphorylated only in ECSCs. These included a regulator of mt metabolism (T250/255, S253 of SIRT3), a gap junction protein functioning in stem cell maintenance (GJA1 at T326, S279/282/306/314/325/365, Y301/313), and glutamate transporter of proliferating stem cells (S74, Y71/75 of SLC1A3). A selection of cell state-specific phosphosites were confirmed by immunoblotting using antibodies that recognize phosphorylated motifs (Figure 4E). The phosphoproteomic data were then mapped onto the 139 MPCs to reveal how the interacting subunits are regulated by phosphorylation. We found 17 mt subunits in one-fifth (26, 19%; Table S4) of the MPCs to be phosphorylated during differentiation. These include MPCs containing the phosphosites on the interacting proteins of mt structure and function (CHCHD3), energy metabolism (BCKDHA, PDHA1, HACD3), and transport (VDAC1), reflecting modest capacity for post-transcriptional modification.

The dynamic phosphorylation events observed among the proteins in ECSCs or DNLCs led us to investigate which mt kinases carry out these modifications. We therefore specifically searched the mt kinases and their substrates localized in mt for all identified phosphosites by mapping known kinases defined in PhosphoSitePlus and high-confidence kinase-specific phosphosites predicted from the GPS 3.0 tool. By constructing a human mt kinase-substrate phosphorylation subnetwork in ECSCs and/or DNLCs, we could identify 3 known and 18 putative unexplored substrates for 4 different mt kinases (mTOR, CDK1, PRKACA, RPS6KB1), encompassing 31 kinase-substrate relationships (Figure 4F; Table S4). For example, a series of
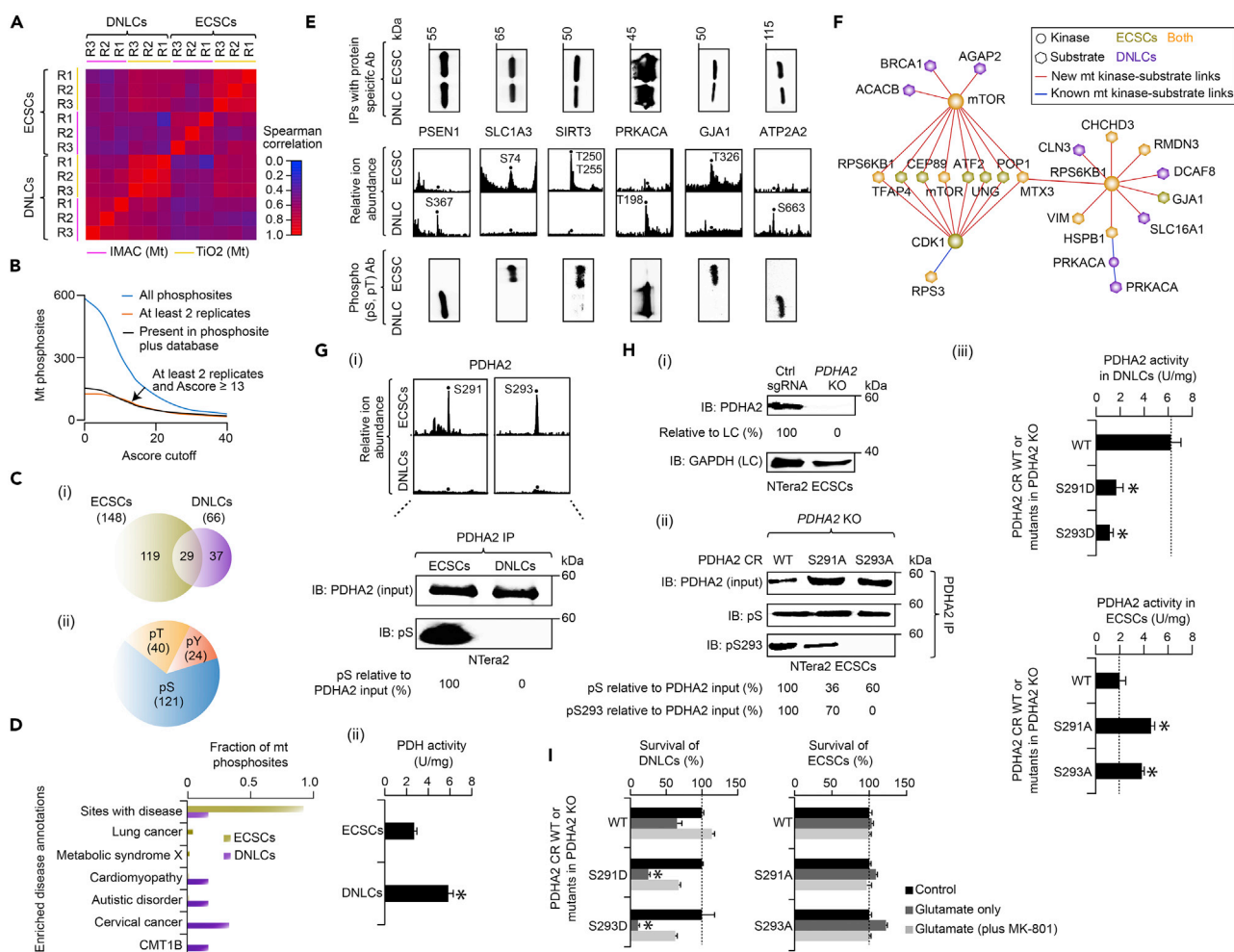
Figure 4. Identification of Phosphorylation Sites in ECSCs and DNLCs

(A) Spearman correlation profiles clustered between phosphoproteome replicate experiments (using peptide counts for each phosphorylation site) from the mt extracts of ECSCs and DNLCs using the indicated phosphopeptide enrichment methods.

(B) mt phosphosites in each cell state with various Ascore cutoff and replicate measurements.

(C) Phosphosites specific or common to each cell state (i) and their localization (ii) on serine (pS), threonine (pT), and tyrosine (pY) residues.

(D) Enrichment of all phosphosites and those associated with human diseases (few representative ones highlighted); false discovery rate (Benjamini-Hochberg correction)-adjusted p value (or Q-value) of the Fisher's exact test.

(E) Relative ion abundance for proteins indicated with cell state-specific phosphosites were immunoprecipitated and probed with protein-specific and phospho (pS, pT) antibodies.

(F) Kinase-substrate phosphorylation network (Table S4) in ECSCs and/or DNLCs is indicated with mt kinases (circle) and their mt substrates (hexagonal).

(G) Relative ion abundance of PDHA2 phosphosites in ECSCs, and immunoprecipitates of PDHA2 immunoblotted (IB) with pS antibody (i). Band intensities normalized to PDHA2. PDH activity (ii) measured after 60 min of incubation with mt extracts from ECSCs or DNLCs.

(H) PDHA2 (i) and pS or pS293 (ii) levels measured in control (ctrl) single-guide RNA (sgRNA) and *PDHA2* KO ECSCs, or in the immunoprecipitates of *PDHA2* KO ECSCs complemented with wild-type (WT) CRISPR-resistant (CR) copy of *PDHA2* and non-phosphorylatable mutants using anti-PDHA2 antibody were IB with indicated antibodies. Band intensities normalized to PDHA2. Activity of PDHA2 (iii) is shown after 60 min of incubation with the mt extracts of WT or *PDHA2* phosphomimetic and non-phosphorylatable mutants from DNLCs and ECSCs, respectively.

(I) Survival of *PDHA2* mutants and WT ECSCs or DNLCs in control salt solution, glutamate (1 mM), or glutamate plus MK-801 (300 nM). Data for (G, H, and I) are mean $\pm$ SD (n = 3 biological replicates; *p $\leq$ 0.05 by Student's t test).

See also Table S4.

cell state-specific phosphorylation sites of potential substrates involved in mt and neuronal functions (ATF2, CEP89, MTX3, POP1, TFAP4, UNG, RPS6KB1) were predicted for two (mTOR, CDK1) known kinases, highlighting the intricate mt kinase-substrate relationships involved in the process of neuronal differentiation.

Among the mt phosphoproteins detected, we found two (S291, S293) phosphorylated serine residues on PDHA2 in ECSCs, but not in DNLCs. Although PDHA2 phosphosites have been reported in PhosphoSite-Plus, little is known about their effects on PDHA2 activity during differentiation. Immunoblotting PDHA2 IPs with an anti-phosphoserine antibody in ECSCs and DNLCs confirmed a phosphorylated serine in ECSCs, and not in DNLCs. As well, we found that the mt PDH activity in DNLCs was increased when compared with ECSCs (Figure 4G). These observations led us to hypothesize that PDHA2, responsible for the conversion of pyruvate into acetyl coenzyme A, becomes dephosphorylated to increase its enzyme activity, presumably to cope with the increased energy requirements of NTera2 cells during neuronal differentiation.

To ascertain if the increased phosphorylation of serine residues in ECSCs was specific, we generated CRISPR-Cas9-mediated *PDHA2* knockouts (KOs) in ECSCs and complemented the cells with the wild-type CRISPR-resistant copy of *PDHA2* and phosphomimetic (*PDHA2* S291D, S293D) or non-phosphorylatable (*PDHA2* S291A, S293A) mutants to mimic constitutive phosphorylation and dephosphorylation, respectively. In contrast to wild-type, non-phosphorylatable mutants in ECSCs exhibited reduced phosphoserine levels using available antibodies for anti-phosphoserine or specific to PDHA2 residue phosphorylated at S293, indicating that the mutants were expressed and had the expected phosphorylation status (Figure 4H). Most notably, the non-phosphorylatable mutants in ECSCs showed a 2.0- to 2.3-fold increase in PDHA2 activity over wild-type, whereas in DNLCs the phosphomimetics significantly lowered (4- to 6-fold) the PDHA2 activity (Figure 4H). This modulation in the activity of PDHA2 by phosphorylation suggests a mechanism by which cells adapt to meet increased energy demands of neurons during differentiation. To examine this notion further, we hypothesized that the phosphomimetic *PDHA2* mutants would result in reduced survival of DNLCs in response to glutamate excitotoxicity (i.e., neuronal death caused by glutamate exposure) due to impairment in energy production. Intriguingly, exposure of phosphomimetic mutants to glutamate significantly reduced survival in DNLCs when compared with wild-type cells. This effect was specific as MK-801 (a glutamate receptor antagonist) rescued the DNLCs from glutamate cytotoxicity. Conversely, non-phosphorylatable mutants did not show any considerable effect on the ECSCs when exposed to glutamate with and without MK-801 (Figure 4I). Taken together, our results suggest that the PDHA2 dephosphorylation in DNLCs plays a role in enhancing energy production, which is required to protect from glutamate excitotoxicity, whereas phosphorylated PDHA2 is detrimental to DNLCs.

Orphan Membership within MPCs in DNLCs Reveals C20orf24-Respirasome Interplay

The importance of mt respiratory function and energy metabolism for neuronal differentiation motivated us to explore the extent to which orphan proteins with no reported functions in MPCs were enriched for physical links with proteins known to be involved in these processes. When compared with other orphans in static (ECSCs, DNLCs) or DF networks, we observed that the mt orphan C20orf24 displayed a significant ($1.8 \times 10^{-31} < p < 1.7 \times 10^{-2}$) number of associations with proteins functioning in cellular respiration, generation of precursor metabolites and energy, and metabolic processes in DNLC and DF networks (Figure S5C; Table S3). As well, C20orf24 was found to interact with several known members of the mt respirasome complexes, including CI (10 of 45), CIII (4 of 11), and CIV (7 of 13) in the DNLC network. We confirmed these interactions in NTera2 (ECSCs, DNLCs) and/or in mouse brain lysates by co-IP (Figure 5A). This is further in agreement with the molecular docking analysis (Transparent Methods) that showed the putative interaction interface between the 3D modeled structure of C20orf24 and the solved structure of the human respirasome (Guo et al., 2017), particularly with the subunits of CI (NDUFA3/C1/C2/B9/S5, MTND2/ND6), CIII (UQCR11, UQCRC1, MTCYB), and CIV (COX1/3/6A/7A; Figure 5B). We therefore hypothesized that C20orf24 acts as an assembly factor by interacting with CI/III/IV subunits, where its increased expression during neuronal differentiation in healthy individuals enhances respirasome formation, oxygen consumption, and ATP production (Figure 5A) to protect neurons from energy depletion. Conversely, altered C20orf24 expression during differentiation could result in clinical respiratory chain deficiencies.

Consistent with our hypothesis, C20orf24 levels measured by immunoblotting from the mt extracts of DNLCs were 5-fold higher than in ECSCs, similar to the increase of C20orf24 transcript levels detected in DNLCs by scRNA-seq (Figure 5C). MitoCarta 2.0, an updated inventory of human MPs, predicted C20orf24 to localize to mt (Calvo et al., 2016), whereas amino acid sequence analysis using Phobius (a membrane protein topology method) predicted C20orf24 as having two helical transmembrane domains (Figure S6A), suggesting that it is likely to reside in the IMM. Consistent with these results, we observed the association of C20orf24 in the mitoplasts (IMM and matrix) of mouse brain (or in DNLCs) and in the
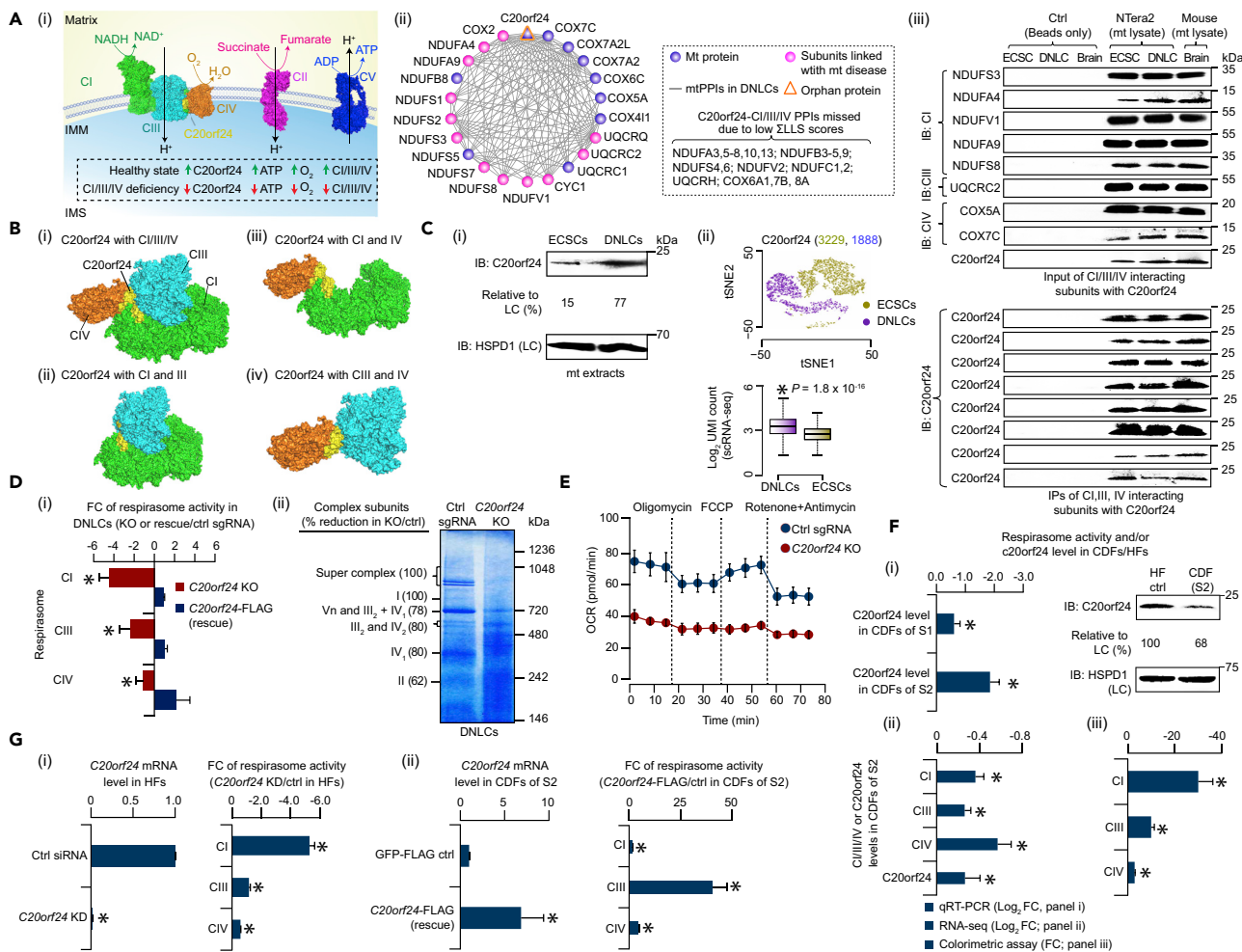
Figure 5. C20orf24 is Required for Respirasome Assembly

(A) Model of C20orf24-respirasome interplay in healthy individuals versus patients with respiratory chain defects (i). Sub-network of C20orf24 link with CI/III/IV subunits in DNLCs (gray lines; ii). CI/III/IV-specific antibody immunoprecipitates and input from the mt extracts of ECSCs, DNLCs, and mouse brain immunoblotted (IB; iii) with antibody raised against C20orf24 and its interacting proteins; protein G beads alone (without antibody) served as negative control.

(B) Docking of C20orf24 (yellow) on the human respirasome CI (green), CIII (cyan), and CIV (orange) structures (i) is shown as a zoom-in where C20orf24 can be seen at the interface with indicated structures of respiratory complex subunits (ii–iv).

(C) Endogenous C20orf24 level in ECSCs and DNLCs with anti-C20orf24 (i). Band intensities normalized to HSPD1 loading control (LC). t-SNE (t-distributed stochastic neighbor embedding) plot (ii; number of single cells shown in parentheses) and $\log_2$ UMI (unique molecular identifier) counts (ii; *p value by Wilcoxon rank-sum test) of the C20orf24 transcript in DNLCs over ECSCs.

(D) Respirasome activity (fold change, FC) of *C20orf24* KO or complemented with FLAG-tagged C20orf24 (rescue) versus control (ctrl) single-guide RNA (sgRNA) in DNLCs (i). Respirasome complexes in control and *C20orf24* KO DNLCs by BN-PAGE (ii); percent reduction of respirasome complex subunits in KO over control is shown after subtracting background signals from each band.

(E) Oxygen consumption rate (OCR) measured in control and KO DNLCs under basal conditions followed by the sequential addition of oligomycin (1 μM), FCCP (0.25 μM; carbonyl cyanide-p-trifluoromethoxyphenylhydrazone), as well as rotenone and antimycin A (0.5 μM).

(F) C20orf24 mRNA or respirasome activity measured by qRT-PCR (i; FC, fold change), RNA sequencing (ii), or colorimetric assay (iii) in the CIV-deficient fibroblasts (CDFs) of two subjects (S1, S2) versus healthy fibroblasts (HFs). Immunoblotting (i) of endogenous C20orf24 level in HFs or CDFs (S2) with anti-C20orf24. Band intensities normalized to HSPD1 loading control (LC).

(G) C20orf24 mRNA or respirasome activity measured by qRT-PCR or colorimetric assay in *C20orf24* knockdown (KD) versus control (ctrl) of HFs (i) or CDFs of S2 complemented with C20orf24-FLAG (rescue) versus GFP-FLAG control (ii). Data for (D, E, F, and G) are mean ± SD (n = 3 technical replicates; *p ≤ 0.05 by Student's t test).

See also Figure S5 and Table S1.

membrane pellet fraction of mt extracts with NaCl or Na_2CO_3, as did IMM, intermembrane space (IMS), and OMM marker proteins (Figure S6B; data for mouse brain shown), indicating membrane localization.

To further establish the subcellular mt localization of C20orf24, we examined mt isolated from mouse brain using proteinase K treatment. If C20orf24 is localized on the IMM, we expect it to be protected from proteinase K digestion. Indeed, in contrast to the OMM marker protein (MFF), we found C20orf24 to be resistant to protease digestion, as were the matrix (HSPD1), IMM (NDUFA4), and IMS (OPA1) marker proteins. Alternately, when the mt was treated with proteinase K in the presence of osmotic shock to selectively open the OMM, C20orf24, like NDUFA4 and HSPD1, was still protected (Figure S6B), whereas OPA1 and MFF were degraded, indicating C20orf24 as an integral IMM protein. Also, the interaction of C20orf24 with the members of the TOMM40 complex (made up of a receptor protein TOMM22, pore-forming subunit TOMM40, and one of the three small TOMM proteins, TOMM5; Figure 3A) further suggests that despite the absence of an mt-targeting signal sequence, C20orf24, like other nuclear-encoded MPs (Kojima et al., 2016), is reliant on translocase activity to reach the IMM.

If C20orf24 expression is elevated in DNLCs and genuinely associated with the subunits of respiratory complexes, its loss of function is likely to affect respirasome activity. To assess this, we created *C20orf24* KOs (Figure S6C) in DNLCs and monitored the stability and activity of respirasome complexes using colorimetric and blue native polyacrylamide gel electrophoresis (BN-PAGE) assays. In both these methods, loss of *C20orf24* in DNLCs consistently reduced respirasome subunit levels (Figure 5D), as well as mt respiratory chain functions (Figure S6D), including the oxygen consumption rate under basal conditions and upon stimulation with FCCP (carbonyl cyanide-p-trifluoromethoxyphenylhydrazone, an uncoupler of OXPHOS; Figure 5E), with no corresponding change in extracellular acidification rate (an indicator of glycolytic activity; Figure S6D). Remarkably, complementation of exogenous FLAG-tagged C20orf24 in the stable *C20orf24* KO DNLCs restored the respirasome levels (Figure 5D), supporting the hypothesis that C20orf24 is a previously unknown assembly factor associated with the respirasome.

Alignment of the C20orf24 protein sequence against the subunits of the respirasome complex showed that C20orf24 shared more than 20% amino acid sequence identity with the CIV subunit COX6C (Figure S6E), whereas the sequence identity dropped below 20% with all other respirasome components. This observation, and the association of C20orf24 with the CIV subunits, inspired us to decipher the role of C20orf24 in CIV deficiency. Although reduced C20orf24 mRNA was observed in CIV-deficient fibroblasts (CDFs) from two unrelated subjects using quantitative real-time PCR (qRT-PCR; Figure 5F), a marked decrease of C20orf24 in the CDFs of one of the subjects led us to examine its level and respirasome activity in this sample using other measures. As with reduced C20orf24 mRNA (or protein), respirasome activity was also significantly ($p \leq 0.05$) depleted in this patient's CDFs using RNA-seq and CI/III/IV colorimetric assays (Figure 5F), suggesting that reduced C20orf24 lessens respirasome function.

Next, we performed two assays to determine if the reduction of C20orf24 mRNA can result in the phenotypic characteristics observed in CIV-deficient patient cells (Figure 5G). First, using an small interfering RNA (siRNA)-mediated *C20orf24* knockdown in healthy fibroblasts, we found that reduction in C20orf24 mRNA significantly ($p \leq 0.05$) lowered respirasome levels compared with a non-targeting siRNA control. Second, C20orf24 mRNA expression and respirasome activity was fully restored in CDFs expressing wild-type C20orf24, suggesting that C20orf24 plays a key role in maintaining respirasome activity in patients deficient in CIV. Whole-exome sequencing analyses of 295 Japanese patients with childhood-onset mt respiratory chain complex deficiencies, including 55 with defects in CIV, revealed that 29 patients carried 2 homozygous and 12 heterozygous variants in the C20orf24 region: 7 intronic and 5 in the 3′ UTR (Table S1). Existing exome or genome aggregation databases were used to identify the frequency of these alleles in the overall population, and classify them as common (with a minor allelic frequency [MAF] > 5%), less frequent (MAF 1%–5%), or rare (MAF <1%). Among the 14 variants, 16 patients (6 with CI, 1 with CIII, 3 with CIV, 6 with com­bined respiratory chain complex deficiencies) carried a less frequent heterozygous variant in the 3′ UTR of C20orf24 (GenBank: NM_199483.2 [c.*226G > A]; NM_001199534.1 [c.*402G > A]; NM_018840.4 [c.*398G > A]). We therefore pursued the principal C20orf24 transcript variant (c.*398G > A) for further analysis of its functional effect on respirasome activity.

As 3′ UTRs are a convergence point for gene expression regulation by microRNAs (miRNAs), we hypothesized that in patients with CIV deficiency, miRNAs differentially regulate respirasome levels via

C20orf24. To investigate this, we identified two human miRNA species using miRTarbase (hsa-miR-452-3p, -532-3p), binding in regions of the variant c.*398G > A. The miRIDIAN hairpin inhibitors designed specifically to target the two selected miRNAs in treated CDFs (of second subject) increased the C20orf24 mRNA and respirasome activity compared with a non-targeting miRIDIAN miRNA hairpin inhibitor control (Figure S6F). To ascertain if the observed increase of C20orf24 mRNA and respirasome activity in CDFs is due to the 3′ UTR of the C20orf24 variant affected by miRNAs, we ectopically expressed the wild-type (c.398G > G) and variant (c.*398G > A found in the patients with CIV deficiency) 3′ UTR of C20orf24 in healthy fibroblasts downstream of the C20orf24 coding sequence. We found that the variant showed considerable reduction of C20orf24 mRNA and respirasome activity relative to wild-type (Figure S6G). Conversely, the healthy fibroblasts containing the C20orf24 variant significantly ($p \leq 0.05$) increased C20orf24 mRNA expression and respirasome activity when treated with a select miRIDIAN hairpin inhibitor (hsa-miR-452-3p), when compared with healthy fibroblasts transfected with wild-type or with variant and control inhibitor (Figure S6G), indicating that the *C20orf24* variant in respirasome function for patients with CIV-deficiency is via miRNA-mediated gene silencing. Jointly, based on its interaction with CI/III/IV subunits and its role in respiratory function, we propose to rename C20orf24 as RCAF1 (respirasome complex assembly factor 1), a candidate gene for respirasome and human respiratory complex chain deficiencies.

NENF Binding with DJ-1 and PINK1 Is Vital for Neurotrophic Activity in DNLCs

Another interesting interaction observed in our DNLC network (Figure 6A) was between an NENF protein involved in neuronal differentiation and survival (Kimura et al., 2008) and a PD-causing protein (DJ-1, the product of *PARK7* gene) implicated in the maintenance of mt homeostasis (Ottolini et al., 2013). Although neurotrophic activity of NENF is dependent on heme binding, the mechanism by which heme interacts with NENF still remains unclear (Kimura et al., 2013). Association of NENF with DJ-1 therefore led us to examine its role in binding with heme to promote neurotrophic activity and neuronal survival.

NENF, which is endogenously expressed in mouse brain (Kimura et al., 2008), including in rat or human substantia nigra (SN) and CA1 hippocampal regions (Figures S7A and S7B), contains a secretory signal peptide and mt-targeting sequence (predicted by Phobius, Target P1.1). Immunoblots of subcellular fractions and immunocytochemical analyses of NTera2 cells and mouse or rat brain regions (SN, hippocampal) showed an accumulation of NENF in the mt, endoplasmic reticulum (ER), and mitochondria-associated membrane (MAM) fractions (Figures 6B and S7C; data for SN shown). As with DJ-1 (Ottolini et al., 2013; Zhang et al., 2005), the presence of NENF in the mt and MAM fractions allowed us to further explore if NENF and DJ-1 co-localized between mt and ER. Using co-IP and/or immunocytochemistry in NTera2 (ECSCs, DNLCs), mouse brain, and rat CA1 hippocampal or SN lysates, we found that NENF preferentially binds with DJ-1 in the mt, ER, and MAM fractions (Figures 6B, 6C, and S7D; data for SN shown). Similarly, NENF was found to interact with a PD-contributing protein, PINK1 (PTEN-induced putative kinase 1; Figure 6B), that localizes to MAM (Gelmetti et al., 2017) and physically associates with DJ-1 (Tang et al., 2006). Consistent with this finding, we observed NENF to be associated with DJ-1 and PINK1 in the SN of healthy subjects and those with sporadic PD (Figure S7B), suggesting this binding to occur both in the healthy human brain and in PD.

Based on our observations, we postulated that NENF binding with DJ-1 and PINK1 facilitates the loading of heme from mt, which promotes neuronal survival because of the increased neurotrophic activity of NENF. However, dissociation of the NENF-DJ-1 (or PINK1) interaction might impede the loading of heme into NENF, resulting in neuronal cell death due to reduced neurotrophic activity of NENF (Figure 6A). To investigate this, we attempted to detect endogenous NENF secretion in ECSCs and DNLCs and found that NENF was discernible in conditioned culture medium and cell lysates (Figure 6D), as previously reported in mouse neuroblastoma cells (Kimura et al., 2008). However, as in *NENF* KO, the endogenously secreted *NENF* was significantly ($p \leq 0.05$) less prominent in the conditioned medium of ECSCs or DNLCs with *DJ-1* and *PINK1* KOs compared with control cells (Figures 6E and S7E). This finding prompted us to examine if DJ-1 and PINK1 have any underlying role in the localization of NENF in mt, ER, and MAM compartments. We therefore performed immunoblotting using an anti-NENF antibody to detect the endogenous NENF in mt, ER, and MAM extracts of DNLCs with *DJ-1* or *PINK1* KOs, and fibroblasts derived from subjects with PD with a *PINK1* mutation. In contrast to control DNLCs or fibroblasts from healthy subjects, NENF association with DJ-1 and PINK1 was disrupted at different degrees in the mt, ER, and MAM fractions of *DJ-1* and *PINK1* KO cells, in a manner analogous to that seen in the fibroblasts of subjects with PD with a *PINK1* mutation
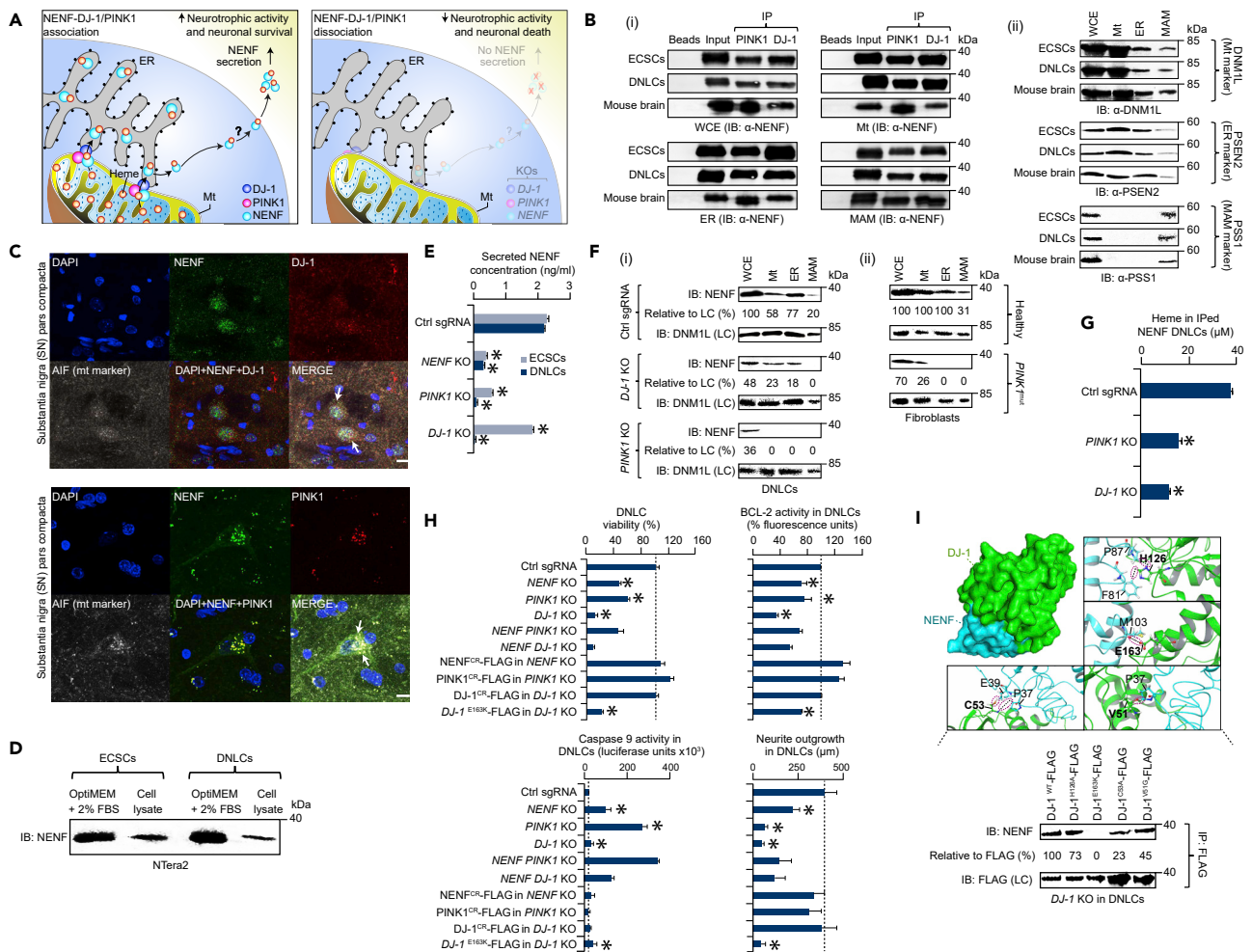
Figure 6. NENF Association with DJ-1 and PINK1 in Neurogenesis

(A) Model of NENF role with DJ-1 and PINK1 in neurotrophic activity and neuronal survival/death; question mark indicates the mechanistic pathway in which NENF secreted is unclear.

(B) PINK1 and DJ-1 immunoprecipitates in whole-cell extract (WCE) as well as in mt, ER, and MAM lysates from ECSCs, DNLCs, and mouse brain using anti-PINK1 and DJ-1 antibodies immunoblotted (IB) with anti-NENF antibody (i). mt, ER, and MAM markers (ii) used as internal control.

(C) Representative confocal micrographs of NENF co-localization (arrow heads) with DJ-1 and PINK1 in the rat SN region using antibodies specific to these native proteins and mt marker (AIF, apoptosis-inducing factor); DNA visualized by DAPI (blue), scale bar, 20 μm.

(D) NENF secretion in the conditioned medium and cell lysates immunoblotted (IB) with anti-NENF antibody.

(E) Secreted NENF measured in control (ctrl) single-guide RNA (sgRNA) and single KOs of ECSCs or DNLCs.

(F) Disruption of NENF association with DJ-1 and PINK1 in the indicated fractions of KOs versus control sgRNA in DNLCs (i) or in the fibroblasts of patients with PD with *PINK1* mutation versus healthy control (ii). Band intensities normalized to loading control (LC).

(G) Heme measured in DNLCs of control sgRNA and indicated KOs with NENF immunoprecipitates.

(H) Neurotrophic (cell viability, neurite outgrowth) and apoptotic activities (BCL-2, caspase-9) in control versus KOs, CRISPR-resistant (CR) genes fused with FLAG in indicated KOs versus control, or DJ-1 wild-type (WT) versus catalytic (E163K) mutant fused with FLAG in *DJ-1* KO DNLCs. Data in (E, G, and H) are mean ± SD (n = 3 biological replicates; *control versus single KOs or DJ-1 WT versus variant (E163K) with p ≤ 0.05 by Student's t test).

(I) DJ-1 (PDB ID: 3SF8) with potential interface residues (bold) binding with NENF. Immunoprecipitates of DJ-1 WT or catalytic mutants fused with FLAG in *DJ-1* KO DNLCs using anti-FLAG antibody IB with anti-NENF or FLAG antibody. Band intensities normalized to LC.

See also Figure S6.

(Figure 6F). The amount of heme in immuniprecipitated NENF was also significantly (p ≤ 0.05) reduced in *DJ-1* and *PINK1* KOs (Figure 6G), when compared with control DNLCs.

To establish if the dissociation of NENF coupling with DJ-1 and PINK1 has any effect on neurotrophic and apoptotic activities, we examined *NENF* and *DJ-1* or *PINK1* single and double KOs in DNLCs. We found

that when compared with control DNLCs, the inhibition of endogenous *NENF* significantly (p ≤ 0.05) reduced cell viability, neurite outgrowth, and expression of an anti-apoptotic BCL-2, with increased pro-apoptotic caspase-9 activity, similar to that observed with *DJ-1* or *PINK1* KOs. Exogenous expression of CRISPR-resistant NENF, PINK1, or DJ-1 fully rescued these phenotypic defects in the respective KO lines (Figure 6H). However, inhibition of both *NENF* and *DJ-1* or *PINK1* did not enhance the effects, suggesting functional cooperation between these proteins in the neurotrophic and apoptotic activities of NENF.

We next predicted the amino acid residue sites of the NENF-DJ-1 association using the available crystal structures of these interacting partners in the Protein DataBank. Specifically, we searched for known mutations on residues located at or near the interaction interface of these proteins, finding four (C53, E163, H126, V51) at the DJ-1 interaction interface (Figure 6I). These four mutations have been previously shown to abrogate the protective activity of DJ-1 (Chen et al., 2010; Shendelman et al., 2004; Taira et al., 2004), with one in particular (homozygous mutation in exon 7, E163) having been identified in an Italian family with three brothers affected by early-onset parkinsonism, dementia, and amyotrophic lateral sclerosis (Annesi et al., 2005). Further assessment of these *DJ-1* mutations showed that E163K (of the four mutant *DJ-1* FLAG variants tested) impaired the NENF-DJ-1 association in DNLCs (Figure 6I), resulting in significant (p ≤ 0.05) reduction in neurotrophic and increase in pro-apoptotic (or decrease in anti-apoptotic) activities similar to that observed in *DJ-1* KO cells (Figure 6H). Although the findings open further avenues to explore the mechanistic pathway in which NENF is secreted, our results support a model where NENF-DJ-1-PINK1 association mediates heme loading from mt, which is essential for neurotrophic activity and neuronal survival, whereas perturbations to these interactions result in neuronal death and may be implicated in PD.

DISCUSSION

Although mapping human cellular interaction networks has continued to reveal important insights into protein function, the full repertoire of cell-context-dependent, native human mtPPIs and phosphorylation sites in MPs that control specific molecular events during neuronal differentiation or how the mtPPI networks change in physiological cell states remains unknown. Our systematic BF/MS approach presented here furthers our understanding of the modular architecture of MPs and the reshuffling of their physical associations as an adaptive response to the physiological cues of neurogenesis.

After rigorously benchmarking and validating mtPPIs from two static (ECSCs, DNLCs) networks using complementary experimental approaches, we identified several unexpected mtPPIs and MPCs annotated to processes critical for neuronal function. Furthermore, the static networks implicated distinct mt hub proteins or interactions for specific cell states, roles for orphan proteins in mt function, subunits of MPCs linked to a spectrum of mt disorders, and CI deficiency-specific perturbations of mtPPIs for a testable disease-relevant outcome. As well, phosphoproteome analysis revealed (1) phosphosites that were not previously reported in the pluripotent state and upon differentiation, (2) distinct phosphosites within the MPCs, (3) cell state-specific mt kinase-substrate pairs, and (4) PDHA2 S291/S293 as an important phosphorylation target that decreased PDHA2 activity in ECSCs, and increased it in DNLCs by dephosphorylation, possibly to support energy requirements for neurons.

Although many identified cell state-dependent PPIs can lend further opportunities to interrogate underlying molecular mechanisms, we focused on two disease-relevant findings from our DNLC network using fibroblasts derived from patients with PD or CIV deficiency. First, the interaction between C20orf24 and CI/III/IV subunits in DNLCs revealed (1) the role of C20orf24 as an assembly factor in stabilizing the activity of respiratory complexes, (2) a relationship between *C20orf24* expression and respirasome levels in DNLCs and healthy fibroblasts, (3) correction of CIV deficiency in patients with reduced respirasome activity through C20orf24 transfection in fibroblasts, (4) a less frequent heterozygous genetic variant c.398G > A in the 3′ UTR of C20orf24 in 16 of the 295 unsolved patients with respiratory chain complex deficiencies, and (5) restoration of respirasome levels by inhibition of two miRNA species targeting the site of c.398G > A in CDFs, suggesting miRNA-mediated regulation of C20orf24 as a contributor to respirasome defects. Although our work provides an in-depth evaluation of C20orf24, much remains to be learned about the contribution of the C20orf24 3′ UTR variant toward respiratory chain deficiencies, and the molecular mechanism by which C20orf24 enhances respirasome formation and activity.

In our second model we observed NENF binding with DJ-1 and PINK1 in the DNLCs and SNs of rat brain or healthy individuals and patients with PD. Abrogation of NENF binding by *PINK1* mutation in the fibroblasts

of a patient with PD, or PD-related *DJ-1* variant (E163K) in DNLCs, implicates this interaction in the disease. We also noticed as in *NENF* KOs, reduced heme production, neuronal viability, neurite outgrowth, and anti-apoptotic activities in the absence of *DJ-1* and *PINK1*, providing mechanistic evidence that the association of NENF with DJ-1 and PINK1 is required for localization of NENF at MAMs, and for loading heme from mt to enhance neurotrophic activity and neuronal survival. Beyond establishing the mechanistic role for PPIs of interest, all constructs (Addgene) and data (http://tap.med.utoronto.ca/HsMTProt; PRIDE communal repository: PXD009831-34) have been released as a resource to create avenues for further exploration of MP function in neurogenesis. Through continued examination, we can also identify MPs linked with PD and respiratory chain deficiencies as targets to ameliorate mt dysfunction and consequent neurogenesis-dependent cognitive and metabolic defects.

Limitations of the Study

As our cross-linker-based BF/MS strategy preferentially detected more stable, higher abundance, and transient mt interactions in native physiological conditions, we may not have captured all relevant human neuronal protein assemblies in the model cell line used. As well, detergent solubilization of the mt membrane may have disrupted interactions with hydrophobic proteins. Mapping interactions of the DNLC network to scRNA-seq indicated that three-fourths (2,455, 69%) of the interacting proteins found to co-elute are primarily from a neuronal cell type, and the remaining are from mixed cell-type populations (Table S2). While these protein associations suggest their requirement for neuronal maintenance and function, their binding within the same or in distinct cell types could be either direct or indirect. Thus the current study could be expanded by performing BF/MS on different cell types at the single-cell level after fluorescence-activated cell sorting from heterogeneous cell populations. Nevertheless, the high-quality mtPPIs we report will be a valuable resource in detailing molecular mechanisms of MPs critical for neurodevelopment, brain function, and mt disease.

METHODS

All methods can be found in the accompanying Transparent Methods supplemental file.

SUPPLEMENTAL INFORMATION

Supplemental Information can be found online at https://doi.org/10.1016/j.isci.2019.08.057.

AUTHOR CONTRIBUTIONS

M.B. designed, conceived, and supervised the study. M.T.M., R.M., S.A., M.Z., J.S., M.G., E.L., and K.B performed cell cultures, human skin fibroblast cultures, co-IPs, immunoblotting, immunocytochemistry, confocal imaging, and functional assays. R.M. laid out the experimental models, generated variants and CRISPR KOs, and designed miRNA inhibitors. M.T.M. carried out structural modeling. M.T.M., L.H., H.A., Z.M., S.A., and N.E.S. performed phosphoproteomics and BF/MS. Q.Z., S.P., and A.G. performed data analyses, with input from M.B. S.P. performed database and PTM searches and created the web portal. M.T.M., R.M., and M.B. wrote the manuscript, with input from others authors. All read and approved the manuscript.

iScience

CellPress

DECLARATION OF INTERESTS

The authors declare no competing interests.

REFERENCES

Alberghina, L., and Gaglio, D. (2014). Redox control of glutamine utilization in cancer. Cell Death Dis. 5, e1561.

Annesi, G., Savettieri, G., Pugliese, P., D'Amelio, M., Tarantino, P., Ragonese, P., La Bella, V., Piccoli, T., Civitelli, D., Annesi, F., et al. (2005). DJ-1 mutations and parkinsonism-dementia-amyotrophic lateral sclerosis complex. Ann. Neurol. 58, 803–807.

Busskamp, V., Lewis, N.E., Guye, P., Ng, A.H., Shipman, S.L., Byrne, S.M., Sanjana, N.E., Murn, J., Li, Y., Li, S., et al. (2014). Rapid neurogenesis through transcriptional activation in human stem cells. Mol. Syst. Biol. 10, 760.

Calvo, S.E., Clauser, K.R., and Mootha, V.K. (2016). MitoCarta2.0: an updated inventory of mammalian mitochondrial proteins. Nucleic Acids Res. 44, D1251–D1257.

Chen, J., Li, L., and Chin, L.S. (2010). Parkinson disease protein DJ-1 converts from a zymogen to a protease by carboxyl-terminal cleavage. Hum. Mol. Genet. 19, 2395–2408.

DiMauro, S., and Schon, E.A. (2008). Mitochondrial disorders in the nervous system. Annu. Rev. Neurosci. 31, 91–123.

Durigon, R., Mitchell, A.L., Jones, A.W., Manole, A., Mennuni, M., Hirst, E.M., Houlden, H., Maragni, G., Lattante, S., Doronzio, P.N., et al. (2018, e8550). LETM1 couples mitochondrial DNA metabolism and nutrient preference. EMBO Mol. Med. 10, e8550.

Enright, A.J., Van Dongen, S., and Ouzounis, C.A. (2002). An efficient algorithm for large-scale detection of protein families. Nucleic Acids Res. 30, 1575–1584.

Fernandez, A., Meechan, D.W., Karpinski, B.A., Paronett, E.M., Bryan, C.A., Rutz, H.L., Radin, E.A., Lubin, N., Bonner, E.R., Popratiloff, A., et al. (2019). Mitochondrial dysfunction leads to cortical under-connectivity and cognitive impairment. Neuron 102, 1127–1142.e3.

Floyd, B.J., Wilkerson, E.M., Veling, M.T., Minogue, C.E., Xia, C., Beebe, E.T., Wrobel, R.L., Cho, H., Kremer, L.S., Alston, C.L., et al. (2016). Mitochondrial protein interaction mapping identifies regulators of respiratory chain function. Mol. Cell 63, 621–632.

Frese, C.K., Mikhaylova, M., Stucchi, R., Gautier, V., Liu, Q., Mohammed, S., Heck, A.J., Altelaar, A.F., and Hoogenraad, C.C. (2017). Quantitative map of proteome dynamics during neuronal differentiation. Cell Rep. 18, 1527–1542.

Gelmetti, V., De Rosa, P., Torosantucci, L., Marini, E.S., Romagnoli, A., Di Rienzo, M., Arena, G.,

Vignone, D., Fimia, G.M., and Valente, E.M. (2017). PINK1 and BECN1 relocalize at mitochondria-associated membranes during mitophagy and promote ER-mitochondria tethering and autophagosome formation. Autophagy 13, 654–669.

Gentil, B.J., Lai, G.T., Menade, M., Lariviere, R., Minotti, S., Gehring, K., Chapple, J.P., Brais, B., and Durham, H.D. (2019). Sacsin, mutated in the ataxia ARSACS, regulates intermediate filament assembly and dynamics. FASEB J. 33, 2982–2994.

Gonzalez-Burguera, I., Ricobaraza, A., Aretxabala, X., Barrondo, S., Garcia del Cano, G., Lopez de Jesus, M., and Salles, J. (2016). Highly efficient generation of glutamatergic/cholinergic NT2-derived postmitotic human neurons by short-term treatment with the nucleoside analogue cytosine beta-D-arabinofuranoside. Stem Cell Res. 16, 541–551.

Grimsrud, P.A., Carson, J.J., Hebert, A.S., Hubler, S.L., Niemi, N.M., Bailey, D.J., Jochem, A., Stapleton, D.S., Keller, M.P., Westphall, M.S., et al. (2012). A quantitative map of the liver mitochondrial phosphoproteome reveals posttranslational control of ketogenesis. Cell Metab. 16, 672–683.

Guo, R., Zong, S., Wu, M., Gu, J., and Yang, M. (2017). Architecture of human mitochondrial respiratory megacomplex I2III2IV2. Cell 170, 1247–1257.e12.

Han, H., Braunschweig, U., Gonatopoulos-Pournatzis, T., Weatheritt, R.J., Hirsch, C.L., Ha, K.C.H., Radovani, E., Nabeel-Shah, S., Sterne-Weiler, T., Wang, J., et al. (2017). Multilayered control of alternative splicing regulatory networks by transcription factors. Mol. Cell 65, 539–553.e7.

Havugimana, P.C., Hart, G.T., Nepusz, T., Yang, H., Turinsky, A.L., Li, Z., Wang, P.I., Boutz, D.R., Fong, V., Phanse, S., et al. (2012). A census of human soluble protein complexes. Cell 150, 1068–1081.

Hein, M.Y., Hubner, N.C., Poser, I., Cox, J., Nagaraj, N., Toyoda, Y., Gak, I.A., Weisswange, I., Mansfeld, J., Buchholz, F., et al. (2015). A human interactome in three quantitative dimensions organized by stoichiometries and abundances. Cell 163, 712–723.

Hosp, F., Vossfeldt, H., Heinig, M., Vasiljevic, D., Arumughan, A., Wyler, E., Genetic and Environmental Risk for Alzheimer's Disease; GERAD1 Consortium, Landthaler, M., Hubner, N., et al. (2015). Quantitative interaction proteomics of neurodegenerative disease proteins. Cell Rep. 11, 1134–1146.

Huttlin, E.L., Bruckner, R.J., Paulo, J.A., Cannon, J.R., Ting, L., Baltier, K., Colby, G., Gebreab, F.,

Gygi, M.P., Parzen, H., et al. (2017). Architecture of the human interactome defines protein communities and disease networks. Nature 545, 505–509.

Huttlin, E.L., Jedrychowski, M.P., Elias, J.E., Goswami, T., Rad, R., Beausoleil, S.A., Villen, J., Haas, W., Sowa, M.E., and Gygi, S.P. (2010). A tissue-specific atlas of mouse protein phosphorylation and expression. Cell 143, 1174–1189.

Ideker, T., and Krogan, N.J. (2012). Differential network biology. Mol. Syst. Biol. 8, 565.

Jiang, D., Zhao, L., Clish, C.B., and Clapham, D.E. (2013). Letm1, the mitochondrial Ca2+/H+ antiporter, is essential for normal glucose metabolism and alters brain function in Wolf-Hirschhorn syndrome. Proc. Natl. Acad. Sci. U S A 110, E2249–E2254.

Kadenbach, B. (2017). Regulation of mammalian 13-subunit cytochrome c oxidase and binding of other proteins: role of NDUFA4. Trends Endocrinol. Metab. 28, 761–770.

Khacho, M., Harris, R., and Slack, R.S. (2018). Mitochondria as central regulators of neural stem cell fate and cognitive function. Nat. Rev. Neurosci. 20, 34–48.

Kimura, I., Nakayama, Y., Yamauchi, H., Konishi, M., Miyake, A., Mori, M., Ohta, M., Itoh, N., and Fujimoto, M. (2008). Neurotrophic activity of neudesin, a novel extracellular heme-binding protein, is dependent on the binding of heme to its cytochrome b5-like heme/steroid-binding domain. J. Biol. Chem. 283, 4323–4331.

Kimura, I., Nakayama, Y., Zhao, Y., Konishi, M., and Itoh, N. (2013). Neurotrophic effects of neudesin in the central nervous system. Front. Neurosci. 7, 111.

Kojima, W., Kujuro, Y., Okatsu, K., Bruno, Q., Koyano, F., Kimura, M., Yamano, K., Tanaka, K., and Matsuda, N. (2016). Unexpected mitochondrial matrix localization of Parkinson's disease-related DJ-1 mutants but not wild-type DJ-1. Genes Cells 21, 772–788.

Kozjak-Pavlovic, V., Ross, K., Benlasfer, N., Kimmig, S., Karlas, A., and Rudel, T. (2007). Conserved roles of Sam50 and metaxins in VDAC biogenesis. EMBO Rep. 8, 576–582.

Kremer, L.S., Bader, D.M., Mertes, C., Kopajtich, R., Pichler, G., Iuso, A., Haack, T.B., Graf, E., Schwarzmayr, T., Terrile, C., et al. (2017). Genetic diagnosis of Mendelian disorders via RNA sequencing. Nat. Commun. 8, 15824.

Kulawiak, B., Hopker, J., Gebert, M., Guiard, B., Wiedemann, N., and Gebert, N. (2013). The

mitochondrial protein import machinery has multiple connections to the respiratory chain. Biochim. Biophys. Acta *1827*, 612–626.

Kwon, T., Choi, H., Vogel, C., Nesvizhskii, A.I., and Marcotte, E.M. (2011). MSblender: a probabilistic approach for integrating peptide identifications from multiple database search engines. J. Proteome Res. *10*, 2949–2958.

Lake, B.B., Ai, R., Kaeser, G.E., Salathia, N.S., Yung, Y.C., Liu, R., Wildberg, A., Gao, D., Fung, H.L., Chen, S., et al. (2016). Neuronal subtypes and diversity revealed by single-nucleus RNA sequencing of the human brain. Science *352*, 1586–1590.

Larsson, N.G., Wang, J., Wilhelmsson, H., Oldfors, A., Rustin, P., Lewandoski, M., Barsh, G.S., and Clayton, D.A. (1998). Mitochondrial transcription factor A is necessary for mtDNA maintenance and embryogenesis in mice. Nat. Genet. *18*, 231–236.

Lee, I., Blom, U.M., Wang, P.I., Shim, J.E., and Marcotte, E.M. (2011). Prioritizing candidate disease genes by network-based boosting of genome-wide association data. Genome Res. *21*, 1109–1121.

Leung, H.C., Xiang, Q., Yiu, S.M., and Chin, F.Y. (2009). Predicting protein complexes from PPI data: a core-attachment approach. J. Comput. Biol. *16*, 133–144.

Lim, S.C., Tajika, M., Shimura, M., Carey, K.T., Stroud, D.A., Murayama, K., Ohtake, A., and McKenzie, M. (2018). Loss of the mitochondrial fatty acid beta-oxidation protein medium-chain acyl-coenzyme a dehydrogenase disrupts oxidative phosphorylation protein complex stability and function. Sci. Rep. *8*, 153.

Liu, F., Lossl, P., Rabbitts, B.M., Balaban, R.S., and Heck, A.J.R. (2018). The interactome of intact mitochondria by cross-linking mass spectrometry provides evidence for coexisting respiratory supercomplexes. Mol. Cell. Proteomics *17*, 216–232.

Malty, R.H., Aoki, H., Kumar, A., Phanse, S., Amin, S., Zhang, Q., Minic, Z., Goebels, F., Musso, G., Wu, Z., et al. (2017). A map of human mitochondrial protein interactions linked to neurodegeneration reveals new mechanisms of redox homeostasis and NF-kappaB signaling. Cell Syst. *5*, 1–14.

Masand, R., Paulo, E., Wu, D., Wang, Y., Swaney, D.L., Jimenez-Morales, D., Krogan, N.J., and Wang, B. (2018). Proteome imbalance of mitochondrial electron transport chain in brown adipocytes leads to metabolic benefits. Cell Metab. *27*, 616–629.e4.

Nepusz, T., Yu, H., and Paccanaro, A. (2012). Detecting overlapping protein complexes in

protein-protein interaction networks. Nat. Methods *9*, 471–472.

Nunnari, J., and Suomalainen, A. (2012). Mitochondria: in sickness and in health. Cell *148*, 1145–1159.

Oliver, S. (2000). Guilt-by-association goes global. Nature *403*, 601–603.

Ottolini, D., Cali, T., Negro, A., and Brini, M. (2013). The Parkinson disease-related protein DJ-1 counteracts mitochondrial impairment induced by the tumour suppressor protein p53 by enhancing endoplasmic reticulum-mitochondria tethering. Hum. Mol. Genet. *22*, 2152–2168.

Pinero, J., Bravo, A., Queralt-Rosinach, N., Gutierrez-Sacristan, A., Deu-Pons, J., Centeno, E., Garcia-Garcia, J., Sanz, F., and Furlong, L.I. (2017). DisGeNET: a comprehensive platform integrating information on human disease-associated genes and variants. Nucleic Acids Res. *45*, D833–D839.

Ruepp, A., Waegele, B., Lechner, M., Brauner, B., Dunger-Kaltenbach, I., Fobo, G., Frishman, G., Montrone, C., and Mewes, H.W. (2010). CORUM: the comprehensive resource of mammalian protein complexes–2009. Nucleic Acids Res. *38*, D497–D501.

Sahni, N., Yi, S., Taipale, M., Fuxman Bass, J.I., Coulombe-Huntington, J., Yang, F., Peng, J., Weile, J., Karras, G.I., Wang, Y., et al. (2015). Widespread macromolecular interaction perturbations in human genetic disorders. Cell *161*, 647–660.

Schweppe, D.K., Chavez, J.D., Lee, C.F., Caudal, A., Kruse, S.E., Stuppard, R., Marcinek, D.J., Shadel, G.S., Tian, R., and Bruce, J.E. (2017). Mitochondrial protein interactome elucidated by chemical cross-linking mass spectrometry. Proc. Natl. Acad. Sci. U S A *114*, 1732–1737.

Sharma, K., Schmitt, S., Bergner, C.G., Tyanova, S., Kannaiyan, N., Manrique-Hoyos, N., Kongi, K., Cantuti, L., Hanisch, U.K., Philips, M.A., et al. (2015). Cell type- and brain region-resolved mouse brain proteome. Nat. Neurosci. *18*, 1819–1831.

Shendelman, S., Jonason, A., Martinat, C., Leete, T., and Abeliovich, A. (2004). DJ-1 is a redox-dependent molecular chaperone that inhibits alpha-synuclein aggregate formation. PLoS Biol. *2*, e362.

Szklarczyk, D., Morris, J.H., Cook, H., Kuhn, M., Wyder, S., Simonovic, M., Santos, A., Doncheva, N.T., Roth, A., Bork, P., et al. (2017). The STRING database in 2017: quality-controlled protein-protein association networks, made broadly accessible. Nucleic Acids Res. *45*, D362–D368.

Taira, T., Saito, Y., Niki, T., Iguchi-Ariga, S.M., Takahashi, K., and Ariga, H. (2004). DJ-1 has a role

in antioxidative stress to prevent cell death. EMBO Rep. *5*, 213–218.

Tang, B., Xiong, H., Sun, P., Zhang, Y., Wang, D., Hu, Z., Zhu, Z., Ma, H., Pan, Q., Xia, H., et al. (2006). Association of PINK1 and DJ-1 confers digenic inheritance of early-onset Parkinson's disease. Hum. Mol. Genet. *15*, 1816–1825.

van de Leemput, J., Boles, N.C., Kiehl, T.R., Corneo, B., Lederman, P., Menon, V., Lee, C., Martinez, R.A., Levi, B.P., Thompson, C.L., et al. (2014). CORTECON: a temporal transcriptome analysis of in vitro human cerebral cortex development from human embryonic stem cells. Neuron *83*, 51–68.

Van Hoof, D., Munoz, J., Braam, S.R., Pinkse, M.W., Linding, R., Heck, A.J., Mummery, C.L., and Krijgsveld, J. (2009). Phosphorylation dynamics during early differentiation of human embryonic stem cells. Cell Stem Cell *5*, 214–226.

Walther, D.M., and Rapaport, D. (2009). Biogenesis of mitochondrial outer membrane proteins. Biochim. Biophys. Acta *1793*, 42–51.

Wan, C., Borgeson, B., Phanse, S., Tu, F., Drew, K., Clark, G., Xiong, X., Kagan, O., Kwan, J., Bezginov, A., et al. (2015). Panorama of ancient metazoan macromolecular complexes. Nature *525*, 339–344.

Warde-Farley, D., Donaldson, S.L., Comes, O., Zuberi, K., Badrawi, R., Chao, P., Franz, M., Grouios, C., Kazi, F., Lopes, C.T., et al. (2010). The GeneMANIA prediction server: biological network integration for gene prioritization and predicting gene function. Nucleic Acids Res. *38*, W214–W220.

Yang, H., Zhou, L., Shi, Q., Zhao, Y., Lin, H., Zhang, M., Zhao, S., Yang, Y., Ling, Z.Q., Guan, K.L., et al. (2015). SIRT3-dependent GOT2 acetylation status affects the malate-aspartate NADH shuttle activity and pancreatic tumor growth. EMBO J. *34*, 1110–1125.

Zhang, L., Shimoji, M., Thomas, B., Moore, D.J., Yu, S.W., Marupudi, N.I., Torp, R., Torgner, I.A., Ottersen, O.P., Dawson, T.M., et al. (2005). Mitochondrial localization of the Parkinson's disease related protein DJ-1: implications for pathogenesis. Hum. Mol. Genet. *14*, 2063–2073.

Zhang, Y., Chen, K., Sloan, S.A., Bennett, M.L., Scholze, A.R., O'Keeffe, S., Phatnani, H.P., Guarnieri, P., Caneda, C., Ruderisch, N., et al. (2014). An RNA-sequencing transcriptome and splicing database of glia, neurons, and vascular cells of the cerebral cortex. J. Neurosci. *34*, 11929–11947.

Zhong, S., Zhang, S., Fan, X., Wu, Q., Yan, L., Dong, J., Zhang, H., Li, L., Sun, L., Pan, N., et al. (2018). A single-cell RNA-seq survey of the developmental landscape of the human prefrontal cortex. Nature *555*, 524–528.

Supplemental Information

Rewiring of the Human Mitochondrial Interactome

during Neuronal Reprogramming Reveals

Regulators of the Respirasome and Neurogenesis

Mohamed Taha Moutaoufik, Ramy Malty, Shahreen Amin, Qingzhou Zhang, Sadhna Phanse, Alla Gagarinova, Mara Zilocchi, Larissa Hoell, Zoran Minic, Maria Gagarinova, Hiroyuki Aoki, Jocelyn Stockwell, Matthew Jessulat, Florian Goebels, Kirsten Broderick, Nichollas E. Scott, James Vlasblom, Gabriel Musso, Bhanu Prasad, Eleonora Lamantea, Barbara Garavaglia, Alex Rajput, Kei Murayama, Yasushi Okazaki, Leonard J. Foster, Gary D. Bader, Francisco S. Cayabyab, and Mohan Babu

SUPPLEMENTARY TABLE LEGENDS

Table S1. Differentially expressed transcripts in DNLCs by bulk RNA-seq or scRNA-seq, and C20orf24 variants in CIV-deficient patient fibroblasts from whole exome sequencing. Related to Figures 1, 5, S1, and Transparent Methods.

Table S2. Scoring and validation of high-quality protein-protein interactions. Related to Figures 2, 3, and Transparent Methods.

Table S3. Identification of putative MPCs and orphan associations in the networks enriched for Gene Ontology (GO) processes. Related to Figures 3, S4, S5, and Transparent Methods.

Table S4. Phosphorylation sites and kinase-substrate associations detected in ECSCs and/or DNLCs. Related to Figure 4 and Transparent Methods.

TRANSPARENT METHODS

Detailed methods are provided below and include the following:

- **KEY RESOURCES TABLE**

- **EXPERIMENTAL MODEL AND SUBJECT DETAILS**

  - Cell Culture and Differentiation

  - Animal Subjects and Tissue Slice Preparation

  - Patient Information

  - Human Skin Fibroblast Cultures

- **METHOD DETAILS**

  - Preparation of Cellular Fractions from Subcellular Components

  - BF/MS

  - Phosphopeptide Enrichment by IMAC and TiO_2

  - Bulk RNA-Sequencing (RNA-Seq) and Single Cell RNA-Sequencing (ScRNA-seq)

  - Immunocytochemistry, Immunohistochemistry, and Confocal Imaging

  - IP and Immunoblotting

  - BN-PAGE and CI/III/IV Colorimetric Assays

  - Oxygen Consumption Rate (OCR) and Extracellular Acidification Rate (ECAR)

  - Structural Modeling and Docking

  - Generation of KOs and Mutagenesis

  - PDH (or PDHA2) Activity and Glutamate Excitotoxicity

  - Quantitative Real-time PCR

  - miRNA or siRNA Transfection

- o Quantification of Cellular Heme and NENF Secretion

- o Neurotrophic and Apoptotic Assays

- **QUANTIFICATION AND STATISTICAL ANALYSIS**

  - o Data Filtering, Scoring mtPPIs, and Defining MPCs

  - o Bulk RNA-seq and ScRNA-seq

  - o Identification of High-Confidence Phosphosites

  - o Enrichment Analyses

  - o Kinase-Substrate Network

  - o Statistical Tests

- **DATA AND SOFTWARE AVAILABILITY**

KEY RESOURCES TABLE

REAGENT or RESOURCE	SOURCE	IDENTIFIER
Antibodies		
Anti-DJ-1	Protein Tech, Abcam	Cat# 11681-1-AP, ab119767
Anti-PINK1	Abcam, Santa Cruz, Invitrogen	Cat# ab23707, sc-517353, PIPA518770
Anti-NENF	Abcam	Cat# ab74474
Anti-C20orf24	LsBio	Cat# LS-C81366
Anti-NDUFA4	Abcam	Cat# ab129752
Anti-NDUFS3	Abcam	Cat# ab177471
Anti-NDUFV1	Abcam	Cat# ab55535
Anti-NDUFA9	Abcam	Cat# ab181381
Anti-NDUFS8	Abcam	Cat# ab170936
Anti-UQCRC2	Abcam	Cat# ab103616
Anti-COX5A	Santa Cruz	Cat# sc376907
Anti-COX7C	Abcam	Cat# ab150953
Anti-GAPDH	Abcam	Cat# ab9485
Anti-NIPSNAP1	Santa Cruz	Cat# sc-393201
Anti-TOMM22	Santa Cruz	Cat# sc-58308
Anti-TOMM40	Abcam	Cat# ab51884
Anti-MTCH2	Abcam	Cat# ab174921
Anti-TOMM5	Abcam	Cat# ab151037
Anti-NDUFS1	Abcam	Cat# ab169540
Anti-PSEN1	Abcam	Cat# ab76083
Anti-SLC1A3	Abcam	Cat# ab416

Anti-SIRT3	Novus Bio	Cat# MAB7488
Anti-PRKACA	Cell Signaling	Cat# 2056S
Anti-GJA1	Novus Bio	Cat# MAB7737
Anti-ATP2A2	Abcam	Cat# ab2861
Anti-pS	Abcam	Cat# ab9332
Anti-pT	Abcam	Cat# ab9337
Anti-PDHA2	Novus Bio	Cat# NBP1-79536
Anti-PDHA2 (pS293)	Novus Bio	Cat#NB11093479
Anti-BCL2	Abcam, Santa Cruz	Cat# ab32124, sc-7382
Anti-DNM1L	Abcam	Cat# ab56788
Anti-PSEN2	Abcam	Cat# ab51249
Anti-PSS1 (PTDSS1)	Santa Cruz	Cat# sc-515376
Anti-FLAG	Sigma	Cat# F1804
Anti-HSPD1	Abcam	Cat# ab46798
Anti-TUBB3	Santa Cruz	Cat# sc-80005
Anti-NEFL	Santa Cruz	Cat# sc-20012
Anti-NEUN	Abcam	Cat# ab177487
Anti-VIM	Santa Cruz	Cat# sc-6260
Anti-ANXA1	Santa Cruz	Cat# sc-12740
Anti-CRMP5 (DPYSL5)	Santa Cruz	Cat# sc-58515
Anti-NRF1	Santa Cruz	Cat# sc-515360
Anti-PSAP	Santa Cruz	Cat# sc-390184
Anti-MFF	Abcam	Cat# ab81127
Anti-OPA1	Santa Cruz	Cat# sc-393296
Anti-SOX2	Santa Cruz	Cat# sc-365964
Anti-TAU	Santa Cruz	Cat #sc-32274
Anti-MAP2	Santa Cruz	Cat #sc-74421
Goat anti-rabbit IgG (H+L) secondary Ab, Alexa Fluor 488 for anti-BCL2	Abcam	Cat# ab15077
Goat anti-mouse IgG (H+L) secondary Ab, Alexa Fluor 488 for anti-TUBB3	Abcam	Cat# ab9871
Goat anti-rabbit IgG (H+L) secondary Ab, Alexa Fluor 488	Thermo Fisher Scientific	Cat# A-11034
Secondary HRP anti-rabbit	Sigma	Cat# A6154
Secondary HRP anti-mouse	Sigma	Cat# A4416
Anti-AIF (Alexa Fluor 647)	Abcam	Cat# ab196847
Anti-KDEL (Alexa Fluor 555)	Abcam	Cat# ab203420
Goat anti-rabbit IgG (H+L) Alexa Fluor 488, polyclonal, secondary Ab	Thermo Fisher Scientific	Cat# A-11034
Goat anti-rabbit IgG (H+L) Alexa Fluor 647, polyclonal, secondary Ab	Thermo Fisher Scientific	Cat# A-21244
Donkey anti-Rabbit IgG (H+L), Alexa Fluor 488, polyclonal, secondary Ab	Thermo Fisher Scientific	Cat# A-21206

Goat anti-mouse IgG (H+L) Alexa Fluor 488, polyclonal, secondary Ab	Thermo Fisher Scientific	Cat# A-11001
Donkey anti-mouse IgG (H+L), Alexa Fluor 568, polyclonal, secondary Ab	Thermo Fisher Scientific	Cat# A-10037
Donkey anti-goat IgG (H+L) Alexa Fluor 488, polyclonal, secondary Ab	Thermo Fisher Scientific	Cat# A-11055
Rabbit anti-goat IgG (H+L) Alexa Fluor 546, Polyclonal, Secondary Ab	Thermo Fisher Scientific	Cat# A-21085
Bacterial and Virus Strains		
DH5α competent cells	Thermo Fisher Scientific	Cat# 18255017
SURE 2 competent cells	Agilent Technologies	Cat #200152
E. coli NEB stable	New England Biolabs	Cat# C3040I
Biological Samples		
Mutant *PINK1* fibroblasts; subject 1 (code: F-PK386)	C. Besta, IRCCS Foundation Neurological Institute, Italy	Male with early-onset PD; homozygous mutation for c.502G>C (p.Ala168Pro); age at biopsy- 59 yrs (biopsy date: June 2003)
Control fibroblasts; subject 1 (code: F-HA498)	C. Besta, IRCCS Foundation Neurological Institute, Italy	Mutation: none; Male; age at biopsy- 54 yrs (biopsy date: Sept 2015); Healthy
Control fibroblasts; subject 2 (code: F-HA499)	C. Besta, IRCCS Foundation Neurological Institute	Mutation: none; Female; age at biopsy- 51 yrs (biopsy date: Sept 2015); Healthy
Mutant NDUFS1 fibroblasts; subject 1 (code: F-DV356)	C. Besta, IRCCS Foundation Neurological Institute, Italy	Female with CI deficiency; compound heterozygous NDUFS1 mutations: c.2083T>C/p.Tyr695His and c.2084A>G/p.Tyr695Cys; age at biopsy- 1 yr (biopsy date: Nov 2006)
Mutant NDUFV1 fibroblasts; subject 1 (code: F-MT5869)	C. Besta, IRCCS Foundation Neurological Institute, Italy	Male with CI deficiency; homozygous NDUFV1 mutation c.1268C>T/p.Thr423Met; age at biopsy- 5 yrs (biopsy date: Feb 2012)
Control fibroblasts; subject 1 (code: F- MT8796)	C. Besta, IRCCS Foundation Neurological Institute, Italy	Mutation: none; Female; age at biopsy- 50 yrs (biopsy date: April 2017); Healthy
Control fibroblasts; subject 2 (code: F- MT8534)	C. Besta, IRCCS Foundation Neurological Institute, Italy	Mutation: none; Male; age at biopsy-57 yrs (biopsy date: Oct 2016); Healthy
Human fibroblasts from CIV-deficient patients (Codes: F-MT2979; F-MT6119)	C. Besta, IRCCS Foundation Neurological Institute, Italy	CIV deficiency; F-MT2979 is a homozygous mutation for c.792_793delAG (subject 1), while F-MT6119 (subject 2) is a compound heterozygous mutation for c.588+1G>A and c.751C>T (p.Gln251Ter).

Patients with CI, CIV and combined respiratory chain complex deficiencies	Saitama Medical University Hospital and Chiba Children's Hospital, Japan	Patient codes, gender, age of onset, enzymatic deficiency, as well as clinical diagnosis and presentation are shown in Table S1 (Sheet 2).
Substantia nigra (SN) from healthy control (SK00237) and PD patient (SK00344)	Saskatoon Health Region, Bioethics Board University of Saskatchewan, Canada	Mutation none; after autopsy, one-half of the brain (SN was isolated when needed) from healthy or PD patient was frozen at -80°C, while the other half was fixed in formalin and examined by a neuropathologist.
Chemicals, Peptides, and Recombinant Proteins		
SCF (C-Kit Ligand) recombinant protein	Thermo Fisher Scientific	Cat# PHC2111
IL3 recombinant protein	Thermo Fisher Scientific	Cat# PHC0035
GM-CSF recombinant protein	Thermo Fisher Scientific	Cat # PHC2015
Basic fibroblast growth factor	Thermo Fisher Scientific	Cat# PHG0261
6-hydroxydopamine hydrobromide	Sigma-Aldrich	Cat# 162957-50MG
DSP	Thermo Fisher Scientific	Cat# 22585
DMEM	GE Healthcare	Cat# SH30243.LS
FBS	Thermo Fisher Scientific	Cat# 12483020
Penicillin/Streptomycin	Thermo Fisher Scientific	Cat# SV30010
Magnetic beads/columns	Miltenyi Biotec GmbH	Cat# 130-042-601, 130-042-701
Trypsin	Promega	Cat# V5280
Opti-MEM I	Thermo Fisher Scientific	Cat# 31985088
Lipofectamine LTX	Thermo Fisher Scientific	Cat# 15338100
Lipofectamine 2000	Thermo Fisher Scientific	Cat# 11668019
Lipofectamine RNAiMAX	Thermo Fisher Scientific	Cat# 13778075
Retinoic acid	Sigma-Aldrich	Cat# R2625
Hexadimethrine bromide	Sigma-Aldrich	Cat# H9268
Digitonin	GoldBio	Cat# D-180-2.5
Protease/phosphatase inhibitors	EMD Millipore	Cat# 539133, 524628
Coenzyme A	Calbiochem	Cat# 234101
Adenosine 5 Triphosphate disodium salt	Calbiochem	Cat# 1191
NAD, Free acid, Grade I	Roche Diagnostic GmBH	Cat # 10127965001
ß-glycerol phosphate disodium salt	Sigma	Cat # 50020
Rotenone	Sigma	Cat# R8875
Antimycin A	Sigma	Cat# A8674

Carbonyl cyanide 3-chlorophenylhydrazone	Sigma	Cat# C2759
Sodium Pyruvate	Sigma	Cat# P2256
Thiamine pyrophosphate	Sigma	Cat# C8754
Potassium cyanide	Sigma	Cat# 60178
Anti-FLAG M2 beads	Sigma	Cat# F3165
Protein A and Protein G microbeads	Milteny Biotec GmbH	Cat# 130-071-001, 130-071-101
DAPI	Sigma Aldrich	Cat# F6057
Hoechst 33342	Thermo Fisher Scientific	Cat# H3570
MitoTracker	Thermo Fisher Scientific	Cat# M7512
EasySep™ Dead Cell Removal (Annexin V) kit	Stemcell Technologies	Cat# 17899
MK-801	Santa Cruz	Cat# sc-203137
pCR-BluntII-TOPO-PDHA2	Dana Farber	HsCD00347415
pENTR223-DJ-1	Dana Farber	HsCD00383508
pPHAGE-C20orf24-C-TAP	Dana Farber	HsCD00448817
pPHAGE-PINK1-C-TAP	Dana Farber	HsCD00460786
pPHAGE-NENF-C-TAP	Dana Farber	HsCD00458563
pPHAGE-CMV-eGFP-W	Dana Farber	EvNO00061634

Critical Commercial Assays

PDH enzyme activity microplate assay kit	Abcam	Cat# 109902
MTT (3-(4, 5-dimethylthiazolyl-2)-2, 5-diphenyltetrazolium bromide cell proliferation kit	ATCC	Cat# 30-1010K
Pierce Fe-NTA or TiO_2 phosphopeptide kits	Thermo Fisher Scientific	Cat# A32992, A32993
Hs-miR-532-3p-1 miScript primer assay	Qiagen	MS00010052
Hs-miR-452*-2 miScript primer assay	Qiagen	MS00009730
Hs-SNORD68-11 miScript primer assay	Qiagen	MS00033712
RNeasy mini kit	Qiagen	Cat# 74104
Caspase-Glo 9 assay	Promega	Cat# 8210
Human NENF ELISA kit	G-Biosciences	Cat# IT4707
Heme assay kit	Sigma	Cat# MAK316
Mitocheck complex 1 kit	Cayman Chemicals	Cat#700930
Mitocheck complex III kit	Cayman chemicals	Cat #700959
Mitocheck complex IV kit	Cayman Chemicals	Cat #700990
M-MLV reverse transcriptase	Thermo Fisher	Cat#28025-013
Luna Universal qPCR mix	New England Biolabs	M3003S

Deposited Data

Experimental PPIs	BioGRID	PMID: 27980099
Experimental PPIs	HumanNet	PMID: 21536720
Protein complexes	CORUM database	PMID: 17965090
Functional PPIs	STRING	PMID: 27924014

Experimental PPIs	GeneMANIA	PMID: 20576703
Experimental PPIs	AP/MS, BF/MS and XL/MS	PMIDs: 26496610, 28514442, 27499296, 28130547, 29128334, 22939629, 29222160, 26344197
Protein localization and domain annotation	Uniprot, HPA	PMIDs: 27899622, 28495876
Protein abundance	Mouse Brain	PMID: 26523646
mRNA expression	Brain cell types	GEO: GSE52564
Disease ontology ID	Biological and clinical human disease-related data	PMID: 26093607
Mt protein assignment	MitoCarta 2.0, Malty et al	PMIDs: 26450961, 25367773
Disease annotation	DisGenNET	PMID: 27924018
Known phosphorylation sites	PhosphoSitePlus	PMID: 22135298
mRNA expression	Brain cell types	GEO: GSE52564
Protein abundance (LFQ)	Mouse Brain	PMID: 26523646
Transcriptome data of brain development	CORTECON	PMID: 24991954
Disease database	OMIM	PMID: 15608251
Disease database	HGMD	PMID: 24077912
Phenotypes and disease models	MGI	PMID: 29092072
Experimental Models: Cell Lines		
NTera2 cl.D1	ATCC	Cat# CRL-1973
SH-SY5Y	ECACC	Cat# 94030304
HEK293T	ATCC	Cat# CRL-3216
Experimental Models: Organisms/Strains		
Mus musculus (C57BL/6)	Jackson laboratory	Cat# 000664
Female Wistar rats	Charles river laboratory	Strain code: 003
Oligonucleotides		
sgRNA-Control-FOR	Sigma-Millipore	CACCGACGGAGGCTAAGCGTCGCAA
sgRNA-Control-REV	Sigma-Millipore	AAACTTGCGACGCTTAGCCTCCGTC
sgRNA-non targeting control	Sigma-Millipore	ACGGAGGCTAAGCGTCGCAA
sgRNA-PDHA2-FOR	Sigma-Millipore	CACCGATGTAATGACGTGATCCGAG
sgRNA-PDHA2-REV	Sigma-Millipore	AAACCTCGGATCACGTCATTACATC
sgRNA-NENF-FOR	Sigma-Millipore	CACCGACTACAGAGTTTTATGGACG
sgRNA-NENF-REV	Sigma-Millipore	AAACCGTCCATAAAACTCTGTAGTC
sgRNA-DJ-1-FOR	Sigma-Millipore	CACCGAGTACAGTGTAGCCGTGATG
sgRNA-DJ-1-REV	Sigma-Millipore	AAACCATCACGGCTACACTGTACTC
sgRNA-PINK1-FOR	Sigma-Millipore	CACCGCGCCACCATGGCGGTGCGAC
sgRNA-PINK1-REV	Sigma-Millipore	AAACGTCGCACCGCCATGGTGGCGC
sgRNA-PARK2-FOR	Sigma-Millipore	CACCGTCCGACTATTTGTTGCGATC
sgRNA-PARK2-REV	Sigma-Millipore	AAACGATCGCAACAAATAGTCGGAC
sgRNA-C20orf24-FOR	Sigma-Millipore	CACCGTGGACCGCGAATCAGTGTGT
sgRNA- C20orf24-REV	Sigma-Millipore	AAACACACACTGATTCGCGGTCCA
PDHA2-FOR	Sigma-Millipore	TAAGCAGCTAGCATGCTGGCCGCCTTC
PDHA2-REV	Sigma-Millipore	TAAGCAACTAGTTTAACTGACGGACTTAA ACTTGATCC

PDHA2-CR-FOR	Sigma-Millipore	GTACAAACAGAAATTCATTCGCGGTTTCTGTCACCTGTGCGATGGTCAGGAAGCTTGTTGCGTGGGCCTTGAGGCCGGCATAAACCCCTCGGATCAC
PDHA2-CR-REV	Sigma-Millipore	GTGATCCGAGGGGTTTATGCCGGCCTCAAGGCCCACGCAACAAGCTTCCTGACCATCGCACAGGTGACAGAAACCGCGAATGAATTTCTGTTT
PDHA2-mut1	Sigma-Millipore	ATGGAGCTGCAAACCTACCG TT ATCATGGACAC
PDHA2-mut2	Sigma-Millipore	CCATGATAACGGTAGGTTTGCAGCTCCATCAGT
PDHA2-mut3	Sigma-Millipore	CGAGAAGAAATTCAGGAAGTAAGAAGTAAGAGG
PDHA2-mut4	Sigma-Millipore	GATCCCTCTTACTTCTTACTTCCTGAATTTCTT
PDHA2-mut-S291D-FOR	Sigma-Millipore	GACATGAGTGATCCTGGAGTCAG TTATCGTACA
PDHA2-mut-S291D-REV	Sigma-Millipore	CTCGTGTACGATAACTGACTCCAGGATCACTCATGTCGTGT
PDHA2-mut-S293D-FOR	Sigma-Millipore	AGTATGGACGATCCTGGAGTCAG TTATCGTACA
PDHA2-mut-S293D-REV	Sigma-Millipore	CTCGTGTACGATAACTGACTCCAGGATCGTCCATACTGTGT
PDHA2-mut-S291A-FOR	Sigma-Millipore	GCCATGAGTGATCCTGGAGTCAG TTATCGTACA
PDHA2-mut-S291A-REV	Sigma-Millipore	CTCGTGTACGATAACTGACTCCAGGATCACTCATGGCGTGT
PDHA2-mut-S293A-FOR	Sigma-Millipore	AGTATGGCCGATCCTGGAGTCAG TTATCGTACA
PDHA2-mut-S293A-REV	Sigma-Millipore	CTCGTGTACGATAACTGACTCCAGGATCGGCCATACTGTGT
DJ-1-outer-FOR	Sigma-Millipore	CTGGTCATCCTGGCTAAAGG
DJ-1-outer-REV	Sigma-Millipore	TGTCCTGGCTGGTCTAGAGG
DJ-1-V51G-FOR	Sigma-Millipore	GTGATGTGGGCATTTGTCCTGATG
DJ-1-V51G-REV	Sigma-Millipore	ACAAATGCCCACATCACGGCTAC
DJ-1-C53A-FOR	Sigma-Millipore	GTGGTCATTGCCCCTGATGCCAGC
DJ-1-C53A-REV	Sigma-Millipore	AGGGGCAATGACCACATCACGGC
DJ-1-H126A-FOR	Sigma-Millipore	GTAAAGTTACAACAGCCCCTCTTGCTAAAGAC
DJ-1-H126A-REV	Sigma-Millipore	GCAAGAGGGGCTGTTGTAACTTTACTTCC
DJ-1-E163K-FOR	Sigma-Millipore	ACCAGCTTCAAGTTTGCGCTTG
DJ-1-E163K-REV	Sigma-Millipore	CGCAAACTTGAAGCTGGTCC
DJ-1-FOR	Sigma-Millipore	CAAAATCAACGGGACTTTCC
DJ-1-REV	Sigma-Millipore	CAGGTTGAACAGCTCTCTGG
CR-DJ-1-FOR	Sigma-Millipore	GTGATGTAGTCATTTGTCCTGATGCC
CR-DJ-1-REV	Sigma-Millipore	AATGACTACATCACGGCTACAC
DJ-1 V51G-CR-FOR	Sigma-Millipore	GTGATGTAGGCATTTGTCCTGATGC
DJ-1 V51G-CR-REV	Sigma-Millipore	TGCCTACATCACGGC
DJ-1 C53A-CR-FOR	Sigma-Millipore	GTGATGTAGTCATTGCCCCTGATG
SpeI-EF1a_F	Sigma-Millipore	ATTACAGGGACAGCAGAGATCCAGTTTGGAGGCTCCGGTGCCCGTCAG

NcoI_EF1a_R	Sigma-Millipore	CCTTTCTTTATGTTTTTGGCGTCTTCCATG TCACGACACCTGAAATGGAAGAAAAAAAC
C20orf24-3UTR_F	Sigma-Millipore	GGATCATCTTTTACACTGCCATC
C20orf24-3UTR_R	Sigma-Millipore	ACTGGTTCCCAAGCTACAGG
BamHI-3UTR_F	Sigma-Millipore	CCAAGAAGGGCGGAAAGATCGCCGTGTA AGTGGTGTACAGCTCCCAAGTGC
BamHI-3UTR_R	Sigma-Millipore	GGCGCCAAAACCCGGCGCGGAGGCCGG ATCGGCTTTATCAGGTATCATCAACAGGT TCTC
C20orf24-outer_F	Sigma-Millipore	GCACAGGAACTTGATCGTTG
C20orf24-outer_R	Sigma-Millipore	GGGCGGAAGGATCAGGAC
C20orf24-inner_F	Sigma-Millipore	AAACAACATGGCTGTATGTGC
C20orf24-inner_R	Sigma-Millipore	CATGTTGTTTCAGAAGACTTGAAATGC
C20orf24-3'UTR-transf_F	Sigma-Millipore	TACCCCTACGACGTGCCCGACTACGCCT AGTGGTGTACAGCTCCCAAGTGC
C20orf24-3'UTR-transf_R	Sigma-Millipore	GGGGGGGGGGGCGGAATTTTCTCAATTAA AGATTTGATTTATTCAAGTATGTGAAAACA TTC
PINK1-outer_F	Sigma-Millipore	ATCCACGCTGTTTTGACCTC
PINK1-outer_R	Sigma-Millipore	AAGAAGCGGAGACGGTTAGG
PINK1-inner_F	Sigma-Millipore	GACAAGCGCTGGGCCGC
PINK1-inner_R	Sigma-Millipore	CGCTTGTCGCACCGCC
miRIDIAN miRNA human hsa-miR-532-3p -hairpin inhibitor	Dharmacon	IH-301109-02-0002
miRIDIAN miRNA human hsa-miR-452-3p -hairpin inhibitor	Dharmacon	IH-300736-08-0002
miRIDIAN miRNA hairpin inhibitor transfection control with Dy547	Dharmacon	Cat # CP-004500-01-05
siGENOME human C20orf24 siRNA	Dharmacon	Cat # 55969
siGENOME non-targeting siRNA	Dharmacon	Cat # D-001206-13-05
Recombinant DNA		
pLEX307_PDHA2-WT	This study	Addgene #115192
pLEX307_PDHA2-S291A	This study	Addgene #115196
pLEX307_PDHA2-S293A	This study	Addgene #115197
pLEX307_PDHA2-S291A S293A	This study	Addgene #115198
pLEX307_CR-PDHA2	This study	Addgene #115199
pLEX307_CR-PDHA2-S291A	This study	Addgene #115203
pLEX307_CR-PDHA2-S293A	This study	Addgene #115204

pLEX307_CR-PDHA2-S291A S293A	Thus study	Addgene #115205
pENTR223-DJ-1-V51G	This study	Addgene #115178
pENTR223-DJ-1-C53A	This study	Addgene #115179
pENTR223-DJ-1-H126A	This study	Addgene #115180
pENTR223-DJ-1E163K	This study	Addgene #115181
pLD-Cc-puro-DJ-1-WT-VA	This study	Addgene #115182
pLD-Cc-puro-DJ-1-V51G-VA	This study	Addgene #115183
pLD-Cc-puro-DJ-1-C53A-VA	This study	Addgene #115184
pLD-Cc-puro-DJ-1-H126A-VA	This study	Addgene #115185
pLD-Cc-puro-DJ-1-E163K-VA	This study	Addgene #115186
pLD-puro-Cc-CR-DJ-1-WT-VA	This study	Addgene # 115187
pLD-puro-Cc-CR-DJ-1-V51G-VA	This study	Addgene #115188
pLD-puro-Cc-CR-DJ-1-C53A-VA	This study	Addgene #115189
pLD-puro-Cc-CR-DJ-1-H126A-VA	This study	Addgene #115190
pLD-puro-Cc-CR-DJ-1-E163K-VA	This study	Addgene # 115191
pLD-puro-CcVA	Moffat Laboratory	Addgene #24588
pPHAGE-C20orf24-C20orf24-3'UTR-WT	This study	Addgene # 128508
pPHAGE-C20orf24-C20orf24-3'UTR-VAR	This study	Addgene # 128509
pPHAGE-CR-PINK1-C-TAP	This study	Addgene # 128510
pPHAGE-CR-NENF-C-TAP	This study	Addgene # 128511
Software and Algorithms		
I-TASSER	Protein structure and function prediction	PMID: 25549265
Kallisto	RNA-seq quantification	PMID: 27043002
PIPER	Schrödinger, LLC	Protein-protein docking
Ascore	Probability score	http://ascore.med.harvard.edu/download.php
SEQUEST	Search engine	PMID: 24226387; In house
STATQUEST	Peptide assignment	PMID: 12644571; In house
Comet	Search engine	PMID: 26115965 Version 2016.01 rev. 0
MS-GF+	Search engine	PMID: 25358478 Version 43
X! Tandem	Search engine	PMID: 14976030 Version: 2007.07.01.3
MSblender	Integration of multiple search engine results	PMID: 21488652
DESeq2	R function	Stats: R package
GO sematic similarity	R package	PMID: 20179076
Student's *t*-test	R function	Stats: R package
HiSeq analysis (ver. 2-2.5. 55.1311)	Variant calling	Illumina
GPS 3.0 software	Kinase-specific phosphosite	http://gps.biocuckoo.org/download.php

CoreMethod	MATLAB code	PMID: 19193141
ClusterONE	Cytoscape app	PMID: 22426491
Gene Set Enrichment Analysis (GSEA)	GSEA (using g:Profiler)	PMID: 16199517
Hypergeometric test	R function	Stats: R package
Fishers exact test	R function	Stats: R package
Wilcoxon signed-rank test.	R function	Stats: R package
Student's t-test	R function	Stats: R package
glmQLFTest	R function	Stats: R package
Network visualization	Cytoscape ver. 3.5.1	PMID: 14597658
miRTarbase	miRNA identification	PMID: 29126174
Band quantification and Neurite outgrowth	ImageJ plugin	PMIDs: 26153368, 22743772; FIJI plugin win64
Four-parameter logistic curve	Quantification of NENF secretion	http://www.myassays.com/four-parameter-logistic-curve.assay
Cell Ranger ver. 3.0.2	10x Genomics	Single cell software downloaded from 10x genomics
Scater ver. 1.12.0	Bioconductor	Stats: R package
Scran ver. 1.12.0	Bioconductor	Stats: R package
DropletUtils ver. 1.4.0	Bioconductor	Stats: R package
Igraph ver. 1.2.4.1	Bioconductor	Stats: R package
Other		
Proteomics data deposition	PRIDE	PXD009831-34
Single cell and bulk RNA-seq data (ECSCs, DNLCs)	NCBI	PRJNA474206

EXPERIMENTAL MODEL AND SUBJECT DETAILS

Cell Culture and Differentiation

NTera2 ECSCs were grown under standard conditions (37°C, 5% CO_2) in DMEM medium (Dulbecco's Modified Eagle's Medium) containing 4 mM L-glutamine, 1 mM sodium pyruvate, 10% fetal bovine serum (FBS), penicillin (100 U/mL), and streptomycin (100 µg/mL). The harvested ECSCs were differentiated into neuron-like cells by seeding at 30% confluency in DMEM containing 10 µM retinoic acid (RA), and changing the medium daily for 4 weeks. After confirming the morphological characteristics of ECSCs and DNLCs using an EVOS cell imaging system, harvested cells were cross-linked as with SH-SY5Y neuronal cells (Malty et al., 2017).

Animal Subjects and Tissue Slice Preparation

All experimental procedures were carried out in accordance to guidelines of the Canadian Council for Animal Care under the supervision of the University of Saskatchewan Animal Care and Supply Committee as well as the University of Regina President's Committee for Animal Care. Female Wistar rats and adult C57BL/6 mice were housed in the pathogen-free laboratory animal care-certified barrier facility maintained at 20-24°C with a natural 12 h light-dark cycle. All animals had unlimited access to standard pelleted diet and tap water.

Female Wistar rats were anaesthetized at 12-14 weeks with halothane and rapidly decapitated, with the brains immediately excised and submerged in oxygenated, ice-cold high-sucrose dissection medium (87 mM NaCl, 25 mM NaHCO$_3$, 25 mM glucose, 75 mM sucrose, 2.5 mM KCl, 1.25 mM NaH$_2$PO4, 7.0 mM MgCl$_2$, 0.5 mM CaCl2). Hippocampal slices taken at 400 µm thickness using a vibrating tissue slicer (Vibram Instruments) was processed in the dissection medium as stated above. Likewise, mice were euthanized by cervical dislocation and brains were quickly removed and washed twice with ice-cold phosphate buffered saline (PBS) containing protease inhibitor cocktail (PIC) and flash-frozen in liquid nitrogen for later use.

Patient Information

Human skin biopsies from healthy and patients harboring the complex I (CI; *NDUFS1/VI*) or Parkinson's disease (PD; *PINK1*) mutations, and deficient for complex IV (CIV) were obtained from IRCCS Foundation Neurological Institute 'C. Besta' (Italy). Likewise, clinically affected tissues (skeletal muscle, liver, heart) or fibroblasts from 295 patients with childhood-onset and mt respiratory chain complex deficiencies were obtained from the Saitama Medical University Hospital and Chiba Children's Hospital (Japan). In all cases, informed written consent from family members was obtained prior to participation in the study, and approval was sought by the

institutional ethics committee. Consent for autopsy is approved by the Saskatoon Health Region and use of autopsy brain for PD research is approved by the University of Saskatchewan Bioethics Board. Autopsy consent is granted by the next-of-kin. Immediately after autopsy, one-half of the brain was frozen at -80°C, while the other half was fixed in formalin and examined by a neuropathologist. Autopsy is performed within 24 h of death.

Human Skin Fibroblast Cultures

Primary skin fibroblasts from healthy and patients with mt respiratory chain complex deficiencies or CI (*NDUFS1, VI*) or PD (*PINK1*) mutations were grown as we previously described (Kohda et al., 2016; Malty et al., 2017). Fibroblasts from healthy (F-HA499) and CIV-deficient patients (F-MT6119, F-MT2979) were cultured in DMEM, supplemented with 15% fetal bovine serum (FBS), 1% penicillin/streptomycin, and 1% L-glutamine (Euroclone). Fibroblast cells maintained at 37°C with 5% CO_2 were detached with trypsin, centrifuged at 500 xg for 10 min at 25 °C, and then harvested at 80-90% confluency.

METHOD DETAILS

Preparation of Cellular Fractions from Subcellular Components

Mitochondria (Mt), endoplasmic reticulum (ER), and mitochondria-associated membrane (MAM) fractions from NTera2 (ECSCs, DNLCs), mouse brain, and healthy or PD patient fibroblasts with *PINK1* mutation were isolated as outlined previously (Wieckowski et al., 2009; Williamson et al., 2015). Isolation of mitoplasts and OMM, carbonate or NaCl extraction, osmotic shock and proteinase K treatment were performed as described (Perciavalle et al., 2012).

BF/MS

A total of 200 µg mt extracts isolated from NTera2 (ECSCs, DNLCs) was subjected to SEC and IEC techniques using an Agilent 1100 HPLC system with 700 fractions collected. SEC was carried out with a 300×7.8 mm BioSep4000 Column (Phenomenex) as per our recently published protocol (Babu et al., 2018), with 84 fractions collected. IEC was performed using a PolyWAX LP column (200 x 4.6 mm id, 5 µm, 1000Å), equilibrating 5 min with buffer A (20 mM Tris-HCl pH 7.8, 0.015% Triton X-100, 1% glycerol) and 30 min linear gradient from 0 to 100% buffer B (Buffer A with 0.6 M NaCl), which resulted in the elution of 87 and 95 fractions in DNLCs and ECSCs, respectively. The fractions were digested with trypsin and analyzed by an Easy-nanoflow liquid chromatography 1000 (Easy nLC; Proxeon) system coupled to an Orbitrap Elite mass spectrometer (ThermoFisher Scientific). Detailed procedures for processing digested samples, chromatographic separation, and control settings for full scanning of mass spectrometry (MS) spectra acquisition are described in our earlier study (Malty et al., 2017).

Phosphopeptide Enrichment by IMAC and TiO₂

Phosphopeptide enrichment by IMAC and TiO_2 was performed as per the protocol from Pierce Fe-NTA or TiO_2 phosphopeptide enrichment kits (ThermoFisher Scientific). Enriched phosphopeptides were analyzed in triplicate by MS on an Orbitrap Elite mass spectrometer using the procedure described (Malty et al., 2017). All samples were acidified with 1% trifluoroacetic acid, desalted (TopTip C-18 columns) and speed-vacuum dried.

Bulk RNA-Sequencing (RNA-Seq) and Single Cell RNA-Sequencing (ScRNA-seq)

Bulk RNA-sequencing was conducted on the NTera2 (ECSCs, DNLCs) cell line, as well as from the fibroblast of a CIV-deficient patient (F-MT6119) and healthy individual (F-HA499) in triplicate at Network Biology Collaborative Centre located at the Lunenfeld-Tanenbaum

Research Institute in Mount Sinai Hospital, or at TCAG (The Centre for Applied Genomics) Toronto Hospital for Sick Children sequencing facility. RNA library was prepared essentially following the protocol of Illumina's NEBNext Ultra II Directional RNA Library Preparation kit.

In brief, double-stranded cDNA synthesized from 800 ng of DNAse-I treated total RNA that was extracted from the indicated samples using a Qiagen Plus mini kit were fragmented into 250-300 bp, end-repaired and adenylated at the 3' end to allow for ligation of Illumina adapters. Library fragments were amplified by initial denaturation at 98°C for 10 s, followed by 8 cycles of 98°C for 10 s, 60°C for 30 s and 72°C for 30 s, and final extension step for 5 min at 72°C. During amplification, each sample was barcoded with a distinct adapter to allow multiplex sequencing. RNA libraries were quantitated by qPCR (KAPA Biosystems), pooled in equimolar quantities, and sequenced on an Illumina HiSeq2500 to generate paired-end reads.

ScRNA-seq was performed on NTERA-2 (ECSCs, DNLCs) cells by thawing approximately 1 million cryopreserved cells and resting in PBS, followed by centrifugation at 400 xg for 7 min. The supernatants were discarded, and cells were resuspended in PBS with BSA, and centrifuged again at 400 xg for 7 min. The dead ECSCs or DNLCs was immunomagnetically removed using the EasySep™ Dead Cell Removal (annexin V) kit. We loaded ~8,000 lives cells each from the negatively-selected suspensions onto the chip to recover ~5,000 cells. Each sample was diluted to a concentration of 700-1200 cells per μl and loaded into individual wells of the 10x Chromium chip following manufacturer's procedures. These includes generation of droplets with encapsulated cells, lysing each cell and reverse transcribing its RNA, and recovering the barcoded cDNA through bead purification and demulsification. The libraries from the pre-amplified cDNA generated using the manufacturer's instructions were sequenced to a depth of 50,000 reads per cell using a S4 flow cell run on the Illumina NovaSeq 6000 system.

Immunocytochemistry, Immunohistochemistry, and Confocal Imaging

Staining to examine the expression of stemness/neuronal markers was carried out as previously described (Malty et al., 2017). Coronal sections were blocked for 1 h in phosphate buffer (PB) solution (pH 7.4) containing 5% horse serum and 0.3% Triton X-100 (Bio-Rad). Proteins of interest were labeled with appropriate primary antibody at 4°C and incubated overnight. Slices were washed three times (10 min) and incubated for 1 h at room temperature with secondary antibody, followed by three 10 min washes in PB. After labeling the slices with DAPI and rinsing three times, it is mounted on gelatin-coated microscope slides and dried overnight at 4°C, followed by treating slices with ProLong Gold Antifade Tissue Mountant (Invitrogen) and sealing under glass coverslips. Imaging was performed using a Zeiss LSM700 laser scanning confocal microscope using a Plan-Apochromat 63X/1.4 oil objective lens. Z-stack images were taken at 1 µm intervals and data was collected using Zeiss Zen 2009 ver. 5.5 (Carl Zeiss).

IP and Immunoblotting

The lysates from NTera2 cells and mouse brain were adjusted to 1 ml with RIPA buffer (Malty et al., 2017) containing PIC and to which 3 µl of antibody was added. After 1 h agitation at 4°C, 100 µl of µMACS protein A magnetic microbeads (Miltenyi) was added with continued agitation for an additional 4 h at 4°C. Microbeads suspension was passed through µMACS columns (Miltenyi), washed 2 times with 1 ml of 0.1% RIPA and PIC, followed by another wash with 1ml detergent free RIPA. Proteins were eluted using 100 µl of 2x Laemmli buffer heated at 95°C. Eluates were analyzed by immunoblotting as described (Malty et al., 2017).

BN-PAGE and CI/III/IV Colorimetric Assays

About 200 µg of mt from control and *C20orf24* knockout (KO) DNLCs solubilized in a sample buffer (Thermo Fisher) with 2% digitonin was centrifuged at 20,000 *xg* for 10 min, followed by

separation of mt respiratory complex assemblies on NativePAGE™ 3-12% Bis-Tris gel at 150V for 30 min and 250V for 150 min. Gel was stained and destained using standard BN-PAGE protocol. The respirasome activity was measured either in DNLCs or in healthy or CIV-deficient fibroblasts (CDFs) transfected with constructs described in Figures 5 and S6, along with appropriate controls, using Mitocheck CI/III/IV kits following the manufacturer's protocol. By calculating the slope from the kinetic measurements of experimental samples over control, the fold change of respirasome activity was determined.

Oxygen Consumption Rate (OCR) and Extracellular Acidification Rate (ECAR)

DNLCs stably expressing *C20orf24* KOs or non-targeting control sgRNA were seeded in Agilent Seahorse XF96 V3 PS culture microplates at a density of 9,000 cells per well. After 24 h, the growth media was replaced with DMEM and processed in the Agilent Seahorse XFe96 analyzer to test for OCR and ECAR. For OCR measurement, cells were treated with a final concentration of 1 μM oligomycin, followed by 0.25 μM FCCP, as well as 0.5 μM rotenone and 0.5 μM antimycin A. In the case of ECAR, the growth media was replaced with Agilent Seahorse XF base medium, and the cells sequentially treated with 10 mM glucose, 1 μM oligomycin, and 50 μM 2-deoxyglucose were analyzed using the Agilent Seahorse Wave software.

Structural Modeling and Docking

Iterative Threading ASSEmbly Refinement (I-TASSER) was used to predict unresolved structures of C20orf24 and NENF proteins. Structure with lowest energy was refined using a fragment-guided molecular dynamic procedure to optimize hydrogen-bonding and remove steric clashes. The resolved human structures of DJ-1 (3SF8), CI (5XTD), CIII (5XTE), and CIV (5XTH) were obtained from protein data bank. The protein models were prepared using the Schrödinger modeling software, and the root mean square deviation was set to 0.3 Å with any

deviation below this was considered negligible. The docking analyses was carried out using PIPER, and for high-scoring docked structure, residues at the complex interface was determined using Schrödinger to measure the change in solvent-accessible surface area between bound and unbound forms of two proteins. Residues with a minimum 15% solvent-accessible surface area in the unbound state were considered as a potential interface between interacting proteins.

Computational Analysis of Off-target Effects of sgRNAs Targeting Select Genes of Interest

Potential off-target effects of sgRNAs designed to target the genes (see Table below) was computationally analyzed using Cas-OFFinder (Bae et al., 2014) and CHOPCHOP (Labun et al., 2019). We found that each of the chosen sgRNAs (results from Cas-OFFinder shown) has a single hit in the human genome with perfect complementarity to its target gene. With the exception of sgRNAs for PDHA2 or PINK1, all other sgRNAs had off-targets with 3 mismatches between sgRNA and genomic DNA, indicating low efficiency of editing. Conversely, CHOPCHOP showed no mismatches or off-target genes. These results suggest that chosen sgRNAs are highly selective and efficient. Nevertheless, to avoid the effects from off-target genes, wherever the gene of interest has been disrupted via CRISPR/Cas9, an add-back/rescue experiment was performed by overexpressing the CRISPR-resistant form of the gene.

Gene	CRISPR sgRNA	DNA targets (mismatches in small case)	Chromosome (Position/ Direction)	Mis matches	Gene at this locus	Seed region mismatch (Y/N)
C20orf24	TGGACC GCGAAT CAGTGT GTNGG	TGGACCGCG AATCAGTGT GTTGG	chr20 (36612167/+)	0	C20orf24	N
		TGGACCGCG AATCAGaGcc TCGG	chr5 (151566267/-)	3	FAT2	Y
		TGaACaGCcA ATCAGTGTG TAGG	chr1 (93923371/+)	3	MTND4P11	N
		TGGAgCGgGA AaCAGTGTGT AGG	chr1 (170669618/-)	3	PRRX1	Y
		TGGACCcCcA				

		ATgAGTGTGT TGG	chr20 (53797878/+)	3	intergenic region	Y
DJ-1	AGTACA GTGTAG CCGTGA TGNGG	AGTACAGTG TAGCCGTGA TGTGG	chr1 (7965361/+)	0	DJ-1	N
		AGTtCAGTGT AaCCGTGgTG GGG	chr8 (137806036/+)	3	intergenic region	Y
		AGTACAGgG TAGatGTGAT GAGG	chr1 (56311500/-)	3	RNA gene (AC119674.1)	Y
		AGTACAGTGa AGCCGTGgTt GGG	chr20 (58234162/-)	3	PPP4R1L	Y
		AGTACAGTG TAtaCGTGATt AGG	chr18 (74900133/+)	3	ZNF407	Y
		AGTgCAGTGT gGCCcTGATG TGG	chr11 (117203117/+)	3	TAGLN	Y
NENF	ACTACA GAGTTT TATGGA CGNGG	ACTACAGAG TTTTATGGAC GAGG	chr1 (212444331/+)	0	NENF	N
		ACTACAtAGg TTTATGGACa AGG	chr3 (24603810/-)	3	RNA gene (THRB-AS1)	Y
		ACcACAGAG TTTTATtGAaG GGG	chr1 (48784413/-)	3	AGBL4	Y
		ACTACAGtGT TTTcTGGACt GGG	chr11 (17958547/+)	3	SERGEF	Y
PINK1	CGCCAC CATGGC GGTGCG ACNGG	CGCCACCAT GGCGGTGCG ACAGG	chr1 (20633541/+)	0	PINK1	N
PDHA2	ATGTAA TGACGT GATCCG AGNGG	ATGTAATGA CGTGATCCG AGGGG	chr4 (95840470/-)	0	PDHA2	N

Generation of KOs and Mutagenesis

CRISPR KOs were generated using the oligonucleotide pairs encoding 20-nt guide RNAs (sgRNAs) targeting sequence for genes encoding interacting proteins using the standard procedure we described earlier (Malty et al., 2017). For selecting *PINK1* or *DJ-1* single KOs, puromycin-resistance selectable marker was used, whereas *NENF* KO was with blasticidin resistance. To generate *PDHA2* phosphomimetic and non-phosphorylatable mutants, sequence

verified plasmid encoding cDNA of PDHA2 (HsCD00347415) from the human ORFeome collection (Dana Farber/Harvard Cancer Center DNA Resource Core) was cloned using the forward and reverse PDHA2 primers into pLEX-307 at the NheI and SpeI restriction sites.

The canonical protospacer adjacent motif (PAM) GGG was mutated to GGA, rendering the PAM site resistant to Cas9 recognition. The pLEX-307-PDHA2 was cut using BsrGI and BmgBI, gel purified, annealed with PDHA2-CR (CRISPR-resistant) oligos, and ligated to generate CR PDHA2 (pLEX PDHA2-CR). This CR PDHA2 was cut using BstXI and BamHI, and the resulting fragments were annealed using the oligos of PDHA2-mut1 and 2, PDHA2-mut3 and 4, which was combined with either PDHA2-mut S291D/S293D (phosphomimetic), or PDHA2-mut S291A/S293A (non-phosphorylatable) listed in **Key Resource Table**. Cut vector and annealed oligos 1 and 2, 3 and 4 and each of the phosphomimetic or non-phosphorylatable mutants were annealed at 16°C overnight. Ligation products were transformed into bacteria and colonies selected. All mutants were verified by sequencing at TCAG.

Additionally, sequence verified Gateway cloning-compatible plasmid (pENTR223) encoding cDNA of DJ-1 (HsCD00383508) from the human ORFeome was mutated using the PCR-driven overlap extension method (Malty et al., 2017). Briefly, two sets of PCR reactions were carried out using DJ-1 outer forward and inner reverse primers corresponding to the desired mutation. For each mutation, a third PCR reaction was run using the forward and reverse PCR reactions mixed along with the outer primers. After digesting the PCR product or plasmid with BsmBI and XbaI, the purified amplicons and plasmid were ligated and sequence verified. Wild type or mutant *DJ-1* was then Gateway cloned into the plasmid pLD-puro-CcVA (Addgene), with a C-terminal versatile affinity (VA) tag containing 3× Flag, 6× histidine, and 2× Streptactin

epitopes (Flag and His separated by dual tobacco etch virus protease cleavage sites). After confirming the resulting clones by sequencing at TCAG they were transfected into *DJ-1* KOs.

Next, the 3'UTR C20orf24 variant was generated using the C20orf24-outer_F, C20orf24-outer_R, C20orf24-inner_F and C20orf24-inner_R primers, and followed the procedure as previously described (Heckman and Pease, 2007). To construct vectors encoding the C20orf24 coding sequence with the ectopic expression of wild type or (c.398G>G) variant (c.*398G>A) 3'UTR of C20orf24 in healthy fibroblasts, we used C20orf24-3'UTR-transf_F and C20orf24-3'UTR-transf_R primers to PCR amplify the wild type or variant 3'UTR of C20orf24. Plasmid (pPHAGE-CMV-C20orf24-C-TAP) encoding the C20orf24 coding sequence (Dana Farber, HsCD00448817) after digesting with EcoRI was combined with the above PCR fragments at appropriate molar ratios, ligated using Gibson assembly, and transformed colonies validated using Sanger sequencing. To generate PINK1-CR, silent synonymous mutations to the PAM site was introduced using PINK1-outer_F, PINK1-outer_R, PINK1-inner_F, and PINK1-inner_R primers, while NENF-CR was created with silent synonymous mutations to the sgRNA seed region in Phe81, Tyr82, Gly83 and Arg84 using a gBlock (IDT) designed with desired mutations. All the resulting mutants were verified by Sanger sequencing. C20orf24, PINK1, and NENF constructs obtained from Dana Farber Plasmid ID repository were c-TAP-tagged, which contains hemagglutinin A (HA) and FLAG epitope tags.

PDH (or PDHA2) Activity and Glutamate Excitotoxicity

The assay mixture contained 25 mM sodium phosphate (pH 7.8), 0.1% digitonin, 0.2 mM CoA, 0.5 mM pyruvate, 0.5 mM NAD, 0.2 mM thiamine pyrophosphate, 1 mM $MgCl_2$, 1 mM DTT, and 50 μL of mt extract from the ECSC or DNLC cultures, or cells stably expressing the wild type *PDHA2,* and phosphomimetic or non-phosphorylatable *PDHA2* mutants in *PDHA2* KO.

The enzyme reaction for PDH (or PDHA2) activity was carried out by incubating the assay mixture every 10 min up to 60 min at 37°C. After terminating the reaction at each time point by the addition of 50 μL of 25 % 5-sulfosalicylic acid, the assay mixture was centrifuged at 12,000 *xg* for 5 min and the supernatant (50 μl) was injected directly into the Agilent 1100 HPLC system. The method employed a Tosoh TSK-GEL ODS-100V column (250 × 4.6 mm i.d., particle size 5 μm) eluted with 100 mM NaH2PO4 and 75 mM CH3COONa (pH adjusted to 4.6 by the addition of H_3PO_4)-acetonitrile (94:6, v/v) at a flow rate of 1.0 ml/min, and an ultraviolet detector set at 259 nm. The standards of CoA and acetyl-CoA were eluted at roughly 11.0 and 25.1 min, respectively, and the enzymatic reaction product was quantified using a calibration curve built with acetyl-CoA. The specific activity of PDH (or PDHA2) was also measured following the method as previously described (Zhou et al., 2008). Susceptibility of ECSC and DNLC cultures expressing the aforesaid constructs to glutamate excitotoxicity was determined using the protocol described previously (Younkin et al., 1993).

Quantitative Real-time PCR

Total RNA was extracted either from the CDFs of two subjects (F-MT6119, F-MT2979) or transfected with constructs (described in Figures 5 and S6) in healthy or CDFs using the RNeasy Mini Kit (Qiagen) as per the manufacturer's protocol. The cDNA was synthesized from 50 ng of total RNA isolated from the aforesaid samples using the M-MLV reverse transcriptase and C20orf24 or beta actin (control) specific primers. PCR reaction was set up using the cDNA mixture, C20orf24 (or beta actin) primers, water, and LUNA universal SYBR green mix. The cycling parameters includes initial holding at 95°C for 10 min, followed by 60 cycles at 95°C for 25 s and 60°C for 1 min. The expression level of each construct normalized to the housekeeping gene was expressed as mean $2^{-\Delta CT}$ or $2^{-[CT\,(construct)\,-\,CT\,(ACTIN)]}$.

siRNA or miRNA Transfection

Healthy or CDFs transfected with pHAGE-eGFP (Harvard Cancer Center DNA Resource Core), C20orf24-FLAG overexpression plasmid (HsCD00448817) from the human ORFeome collection, and with constructs described in Figures 5 and S6, along with controls, was performed using lipofectamine RNAiMAX following manufacturer's instructions. Cells were harvested after 48 h incubation for total RNA and mt extraction.

Quantification of Cellular Heme and NENF Secretion

About 100 µg of proteins from the extracts of DNLCs was used to measure heme production in Synergy plate reader at an absorbance of 400 nm using Sigma's heme assay kit. The NENF secretion from the supernatant of cultured ECSCs or DNLCs (5×10^6 cells) in opti-MEM1 reduced-serum medium with 2% FBS was measured in Synergy plate reader at an absorbance of 450 nm using the human NENF enzyme-linked immunosorbent assay kit (G-Biosciences). The amount of NENF secreted was calculated using a four-parameter logistic curve fit.

Neurotrophic and Apoptotic Assays

Cell viability was assessed following the tetrazolium MTT (3-(4, 5-dimethylthiazolyl-2)-2, 5-diphenyltetrazolium bromide) cell proliferation kit (ATCC) by plating NTera2 DNLCs (5×10^3 cells) and measuring the absorbance (formazan) at 570 nm using a Synergy microplate reader. Neurite outgrowth was examined by plating DNLCs onto 6-well plates coated with poly-L-lysine (20 µg/ml) at a density of 1×10^4 cells/well in DMEM supplemented with 2% FBS. DNLCs were stained with mitotracker, exposed to β3-tubulin primary antibody and counterstained with Alexa 488 anti-mouse secondary antibody. The cells were imaged using the Zeiss Observer Z1 inverted microscope with Colibri 2 epifluorescence, and analyzed for the extension of dendrites and axons with at least two cell body lengths in diameter to score for a positive neurite outgrowth.

The caspase-9 activity was measured using luminescent caspase-Glo 9 assay following the manufacturer's procedure (Promega), periodically for 3 h using Synergy luminescence plate reader. Likewise, the BCL-2 activity was determined by treating DNLCs, plated at a density of 1 x 10^4 cells, with BCL-2 primary antibody for 1 h followed by incubation with Alexa 488 anti-rabbit secondary antibody for 1 h, and with Hoechst 33342 for 10 min. The cells were then read using synergy plate reader at 360 nm for Hoechst and 480 nm for BCL-2 expression level.

QUANTIFICATION AND STATISTICAL ANALYSIS

Data Filtering, Scoring mtPPIs, and Defining MPCs

Prior to generating the high-quality interactions using the integrated log-likelihood scores (ΣLLS), the MS/MS spectra of each biochemical fraction collected from two distinct cell states (ECSCs, DNLCs) was searched against the reference human target-decoy protein sequences (UniProt). As we previously described (Wan et al., 2015), to improve peptide-spectral matching sensitivity and accuracy, we used Sequest (ver. 27 - rev.9) and MS-blender (encompassing X! Tandem ver. 2013.09.01, Comet ver. 2016.01 rev. 3, MS-GF+ ver. 2017.01.13) search engines with default parameter settings to define high-confidence peptide-spectral matches at <1% FDR. Search parameters were set to allow for two missed cleavage sites, precursor mass tolerance ranged from -2 to 4 Da, variable modification of methionine oxidation, protein N-terminal acetylation, and one fixed modification of cysteine carbamidomethylation.

The Sequest search results were evaluated by the Statquest probability algorithm, whereas matches from the other three search engines were integrated with MS-blender, which uses a probabilistic approach to extract the best hits detected by each search method for integration. Prior to scoring, we retained only proteins from both replicates of the same elution techniques (SEC, IEC), and filtered proteins present in only one fraction or more than half of the eluted

fractions. The co-fractionation profile from each replicate of SEC or IEC was scored using PCC, WCC, and co-apex metric as previously reported (Havugimana et al., 2012; Wan et al., 2015). By compiling the curated human protein complexes containing mtPPIs from CORUM database as a reference set, true positive (interacting proteins annotated within the same complex) and true negative PPIs (interacting proteins annotated between complexes) were defined.

For all protein combination pairs, we considered only a PCC or WCC score of at least 0.5 or co-apex of 1, as we reported previously (Havugimana et al., 2012; Wan et al., 2015) to compute the LLS (Babu et al., 2018) against the reference dataset using the following formula:

$$LLS = ln\frac{P(L|E)/{\sim}P(L|E)}{P(L)/{\sim}P(L)}$$

Where *P(L/E)* denotes the frequency of interactions (L) in dataset E (i.e. from each replicate of SEC-MS or IEC-MS) containing the true-positive set, while *~P(L/E)* signifies the frequency of interactions L in the true-negative set. *P(L)/~P(L)* represents the prior odds ratio of true-positive and true-negative PPIs in the reference set. The LLS was computed within a cell state independently for each pairwise interaction in each replicate of SEC-MS or IEC-MS, and then used a weighted sum to produce a final score by averaging all replicates across techniques. The resulting 145,797 scored interactions in DNLCs, and 110,478 in ECSCs that was benchmarked using ROC analysis allowed us to choose a ΣLLS cut-off of ≥1.45 to generate 3,567 high-confidence mtPPIs in DNLCs, and 3,320 in ECSCs, respectively.

To validate interactions in ECSC or DNLC network (**Table S2**), we performed IP/MS (Malty et al., 2017) experiments using antibodies targeting 37 endogenous proteins in the mt extracts of mouse brain lysates, 21 from NTera2 DNLCs, and 79 from SH-SY5Y neuronal cells. Additional validation includes PPIs from BF/MS (84 fractions from SEC; 96 from IEC) performed in duplicate with 200 µg of mt extracts isolated from the mouse brain. As well,

alternate SEC method was conducted by the group of Leonard Foster (British Columbia, Canada) using a reduced quantity of mt extracts (100 µg) from DNLCs and fractionated using 300 x 7.8 mm BioSep4000 Column (Phenomenex) equilibrated with different SEC mobile phase (50 mM KCl, 50 mM NaCH₃COO, pH 7.2) than described above. The samples were separated into 81 fractions in triplicate, for a total of 243 fractionations by an Agilent 1200 series semi-preparative HPLC at a flow rate of 0.5 ml/min at 8°C. The trypsin digested fractions were analyzed using an Orbitrap Elite mass spectrometer, and the resulting MS spectra was acquired and processed as recently described (Malty et al., 2017). Lastly, using mtPPIs from DNLC network, we predicted putative MPCs by CoreMethod algorithm (Leung et al., 2009) with at least one MP, which was overlapped with mtPPIs from ECSC to identify the extent of rewiring within a complex.

Bulk RNA-seq and ScRNA-seq

The raw sequence reads (in FASTQ files) of the DNLCs or fibroblasts of CDFs and healthy individuals were processed using the Kallisto software. The resulting count value X_i for transcript *i* was normalized to CPM_i (Counts per Million) using the formula: $\frac{X_i}{N} \times 10^6$; where N is the number of sequenced fragments. The fold change between DNSCs and ECSCs, as well as between CDFs and healthy samples, and their corresponding Benjamini-Hochberg (BH) adjusted *p*-value for each differentially expressed transcript was computed using DESeq2 in R package.

Cell Ranger from the Chromium Single Cell Software Suite (ver 3.0.2; 10x Genomics) was used to demultiplex the raw base call files from the sequencer; extract, filter, and correct cell barcodes and unique molecular identifiers (UMIs); and remove cDNA PCR duplicates. Cell Ranger was then used to align the single cell sequencing reads (*.fastq.gz) generated for ECSCs and DNLCs to the human reference transcriptome (Sequence: GRCh38). The raw UMI (unique molecular identifiers) counts from each cell state were then aggregated using the 'cellranger

aggr' pipeline into one unified gene-cell matrix file. The aggregation process avoided the batch effects by normalizing the read depth between cell states. The Bioconductor 'scran' (ver 1.12.0) package was used to filter empty droplets, low quality cells (i.e. large proportion of mitochondrial UMI counts above the median of all captured cells), cell multiplets, and genes not expressed in any cells, resulting in a final dataset consisted of 6,583 single cells (3,631 ECSCs, 2,952 DNLCs). UMI counts for each transcript in each cell was measured, and the total number of UMI counts were then averaged from all cells for a given transcript in each cell state. Differential gene expression analysis was calculated between DNLCs and ECSCs datasets, and BH adjusted p-value (i.e. $q \leq 0.01$) was considered significant.

The cell subtype assignments for 2,952 DNLCs was conducted by implementing a shared nearest neighbour-cliq (Xu and Su, 2015), followed by graph-based community detection algorithm (i.e. Walktrap) to identify putative clusters. We then performed pairwise differential gene expression analysis using Welch's t-test for each cluster relative to all other clusters, and chose top 50 significantly ($P \leq 0.05$) ranked genes (with $\log_2$ fold change greater than 0) as gene markers for a given cluster. These were then mapped to known neuronal or glial marker genes from the recently published studies (Lake et al., 2016; Zhong et al., 2018) to assign distinct cell subtypes. Each differentially expressed genes from DNLCs to a major cell subtype was assigned only when their expression level is significantly ($q \leq 0.05$) higher than in other cell subtypes.

Identification of High-Confidence Phosphosites

Peptides were identified using Sequest and filtered at a stringent 1% FDR using the target-decoy approach based on XCorr (>1.5 for +2, +3 and +4 charged precursor ions) and mass accuracy (< 10 ppm) parameters. Each phosphosite was scored using Ascore (Beausoleil et al., 2006), which measures correct phosphosite based on the intensity of site-determining ions in MS/MS spectra.

Only phosphosites with Ascore $\geq$13 ($p \leq 0.05$) and measured in at least two of the three replicates were considered as genuine. In few cases where phosphosites measured in one replicate, exception was made as long as they are detected in PhosphoSitePlus database.

Enrichment Analyses

To identify which bioprocesses the proteins interacting with orphans were enriched in static or DF networks, we used g:Profiler that executes a gene-set enrichment analysis to identify statically enriched annotations on a seed gene list using hypergeometric significance estimation. We considered a process to be enriched when the adjusted p-value was less than 0.05 (or $q \leq$ 0.05) after BH correction. Disease enrichment among the high-confidence phosphoproteins during differentiation was performed by downloading disease annotations from HGMD (Human Gene Mutation Database), genetic variants (single nucleotide polymorphism; SNP) from Uniprot, and disease entries from OMIM ID to disease ontology database. After integrating SNPs and HGMD, we annotated each phosphosite with all non-synonymous mutations that had at least 7 amino acid positions away from the modification site. Disease terms, computed using a Fisher's exact test after BH correction ($q \leq 0.05$) were considered significant.

Kinase-Substrate Network

Kinase-substrate relationships during differentiation were identified by combining all known kinase-substrate interactions from the PhosphoSitePlus database and predicting additional kinase-specific phosphorylation site by GPS 3.0 software with the threshold parameter set to high (FDR 2% for serine/threonine kinases, FDR 4% for tyrosine kinase). We allowed only a kinase-substrate interaction that was either specific or common to each cell state.

Statistical Tests

The results from the functional assays were obtained with enough statistical power by including a minimum of three independent biological and/or technical replicates to draw reasonable conclusions. Significance was determined using standard statistical tests, and wherever possible, non-parametric tests, mean ± SD and number of replicates were outlined in the figure legends.

DATA AND SOFTWARE AVAILABILITY

All raw proteomic data from this work is submitted to the PRIDE repository (Accession: PXD009831-34) at the European Bioinformatics Institute, in accordance with the data sharing policy. As well, scRNA-seq and bulk RNA-seq datasets were deposited at NCBI sequence read archive repository (PRJNA474206). Codes used in generating the results are aforesaid in detail.

SUPPLEMENTARY REFERENCES

Babu, M., Bundalovic-Torma, C., Calmettes, C., Phanse, S., Zhang, Q., Jiang, Y., Minic, Z., Kim, S., Mehla, J., Gagarinova, A*., et al.* (2018). Global landscape of cell envelope protein complexes in Escherichia coli. Nat. Biotechnol. *36*, 103-112.

Bae, S., Park, J., and Kim, J.S. (2014). Cas-OFFinder: a fast and versatile algorithm that searches for potential off-target sites of Cas9 RNA-guided endonucleases. Bioinformatics *30*, 1473-1475.

Beausoleil, S.A., Villen, J., Gerber, S.A., Rush, J., and Gygi, S.P. (2006). A probability-based approach for high-throughput protein phosphorylation analysis and site localization. Nat. Biotechnol. *24*, 1285-1292.

Havugimana, P.C., Hart, G.T., Nepusz, T., Yang, H., Turinsky, A.L., Li, Z., Wang, P.I., Boutz, D.R., Fong, V., Phanse, S*., et al.* (2012). A census of human soluble protein complexes. Cell *150*, 1068-1081.

Heckman, K.L., and Pease, L.R. (2007). Gene splicing and mutagenesis by PCR-driven overlap extension. Nat. Protoc. *2*, 924-932.

Kohda, M., Tokuzawa, Y., Kishita, Y., Nyuzuki, H., Moriyama, Y., Mizuno, Y., Hirata, T., Yatsuka, Y., Yamashita-Sugahara, Y., Nakachi, Y*., et al.* (2016). A Comprehensive Genomic Analysis Reveals the Genetic Landscape of Mitochondrial Respiratory Chain Complex Deficiencies. PLoS Genet. *12*, e1005679.

Labun, K., Montague, T.G., Krause, M., Torres Cleuren, Y.N., Tjeldnes, H., and Valen, E. (2019). CHOPCHOP v3: expanding the CRISPR web toolbox beyond genome editing. Nucleic Acids Res. pii: gkz365.

Lake, B.B., Ai, R., Kaeser, G.E., Salathia, N.S., Yung, Y.C., Liu, R., Wildberg, A., Gao, D., Fung, H.L., Chen, S*., et al.* (2016). Neuronal subtypes and diversity revealed by single-nucleus RNA sequencing of the human brain. Science *352*, 1586-1590.

Leung, H.C., Xiang, Q., Yiu, S.M., and Chin, F.Y. (2009). Predicting protein complexes from PPI data: a core-attachment approach. J. Comput. Biol. *16*, 133-144.

Malty, R.H., Aoki, H., Kumar, A., Phanse, S., Amin, S., Zhang, Q., Minic, Z., Goebels, F., Musso, G., Wu, Z.*, et al.* (2017). A Map of Human Mitochondrial Protein Interactions Linked to Neurodegeneration Reveals New Mechanisms of Redox Homeostasis and NF-kappaB Signaling. Cell Syst. *5*, 1-14.

Perciavalle, R.M., Stewart, D.P., Koss, B., Lynch, J., Milasta, S., Bathina, M., Temirov, J., Cleland, M.M., Pelletier, S., Schuetz, J.D.*, et al.* (2012). Anti-apoptotic MCL-1 localizes to the mitochondrial matrix and couples mitochondrial fusion to respiration. Nat. Cell. Biol. *14*, 575-583.

Wan, C., Borgeson, B., Phanse, S., Tu, F., Drew, K., Clark, G., Xiong, X., Kagan, O., Kwan, J., Bezginov, A.*, et al.* (2015). Panorama of ancient metazoan macromolecular complexes. Nature *525*, 339-344.

Wieckowski, M.R., Giorgi, C., Lebiedzinska, M., Duszynski, J., and Pinton, P. (2009). Isolation of mitochondria-associated membranes and mitochondria from animal tissues and cells. Nat. Protoc. *4*, 1582-1590.

Williamson, C.D., Wong, D.S., Bozidis, P., Zhang, A., and Colberg-Poley, A.M. (2015). Isolation of Endoplasmic Reticulum, Mitochondria, and Mitochondria-Associated Membrane and Detergent Resistant Membrane Fractions from Transfected Cells and from Human Cytomegalovirus-Infected Primary Fibroblasts. Curr. Protoc. Cell Biol. *68*, 3 27 21-33.

Xu, C., and Su, Z. (2015). Identification of cell types from single-cell transcriptomes using a novel clustering method. Bioinformatics *31*, 1974-1980.

Younkin, D.P., Tang, C.M., Hardy, M., Reddy, U.R., Shi, Q.Y., Pleasure, S.J., Lee, V.M., and Pleasure, D. (1993). Inducible expression of neuronal glutamate receptor channels in the NT2 human cell line. Proc. Natl. Acad. Sci. U S A *90*, 2174-2178.

Zhong, S., Zhang, S., Fan, X., Wu, Q., Yan, L., Dong, J., Zhang, H., Li, L., Sun, L., Pan, N.*, et al.* (2018). A single-cell RNA-seq survey of the developmental landscape of the human prefrontal cortex. Nature *555*, 524-528.

Zhou, Q., Lam, P.Y., Han, D., and Cadenas, E. (2008). c-Jun N-terminal kinase regulates mitochondrial bioenergetics by modulating pyruvate dehydrogenase activity in primary cortical neurons. J. Neurochem. *104*, 325-335.
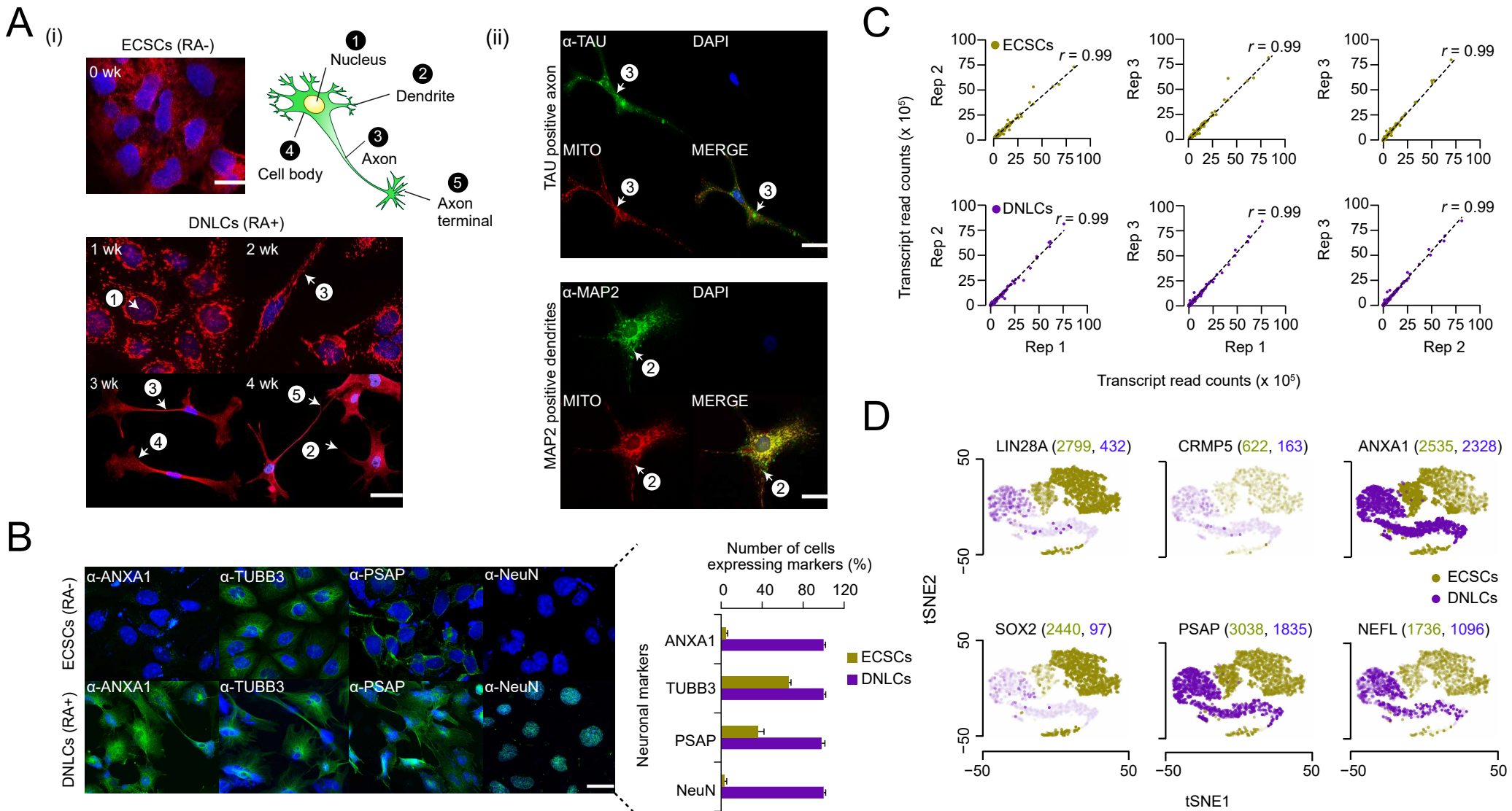
Figure S1. Morphological Characterization and Transcriptome Profile Changes in ECSCs and DNLCs. Related to Figure 1 and Transparent Methods.

(A) Micrographs portraying ECSCs in the absence (-) of retinoic acid (RA), and DNLCs with its various neuronal parts as indicated in the presence (+) of RA each week over a differentiation period of 4 weeks (i). Cells were stained with mitotracker (red) and DNA visualized by DAPI (blue). Images of DNLCs positive for Tau axonal and MAP2 dendritic markers (ii); scale bar, 10 μm.

(B) Micrographs and quantitation on the number of ECSCs and DNLCs (n = 300 cells per replicate; 4 weeks after differentiation) expressing neuronal markers. DNA visualized by DAPI (blue); scale bar is 20 μm. Data are mean ± SD (n = 3 technical replicates).
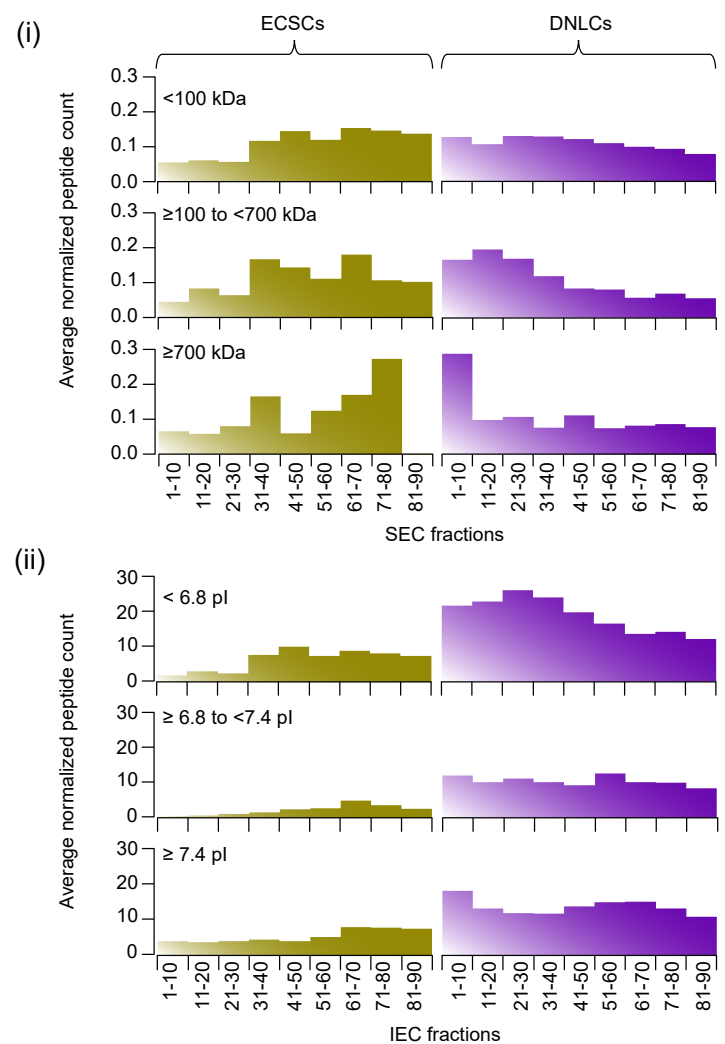
(C) Average correlation of all transcript read counts between replicates in each cell state.

(D) T-SNE plots showing the distribution of cell states (number of single cells shown in parentheses) for each of the indicated stemness/neuronal markers.
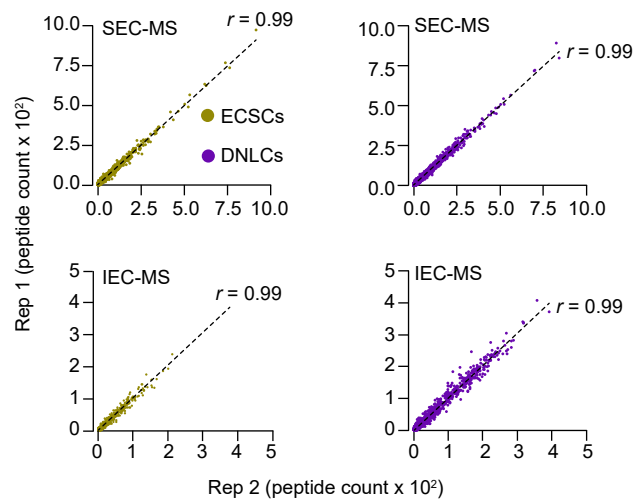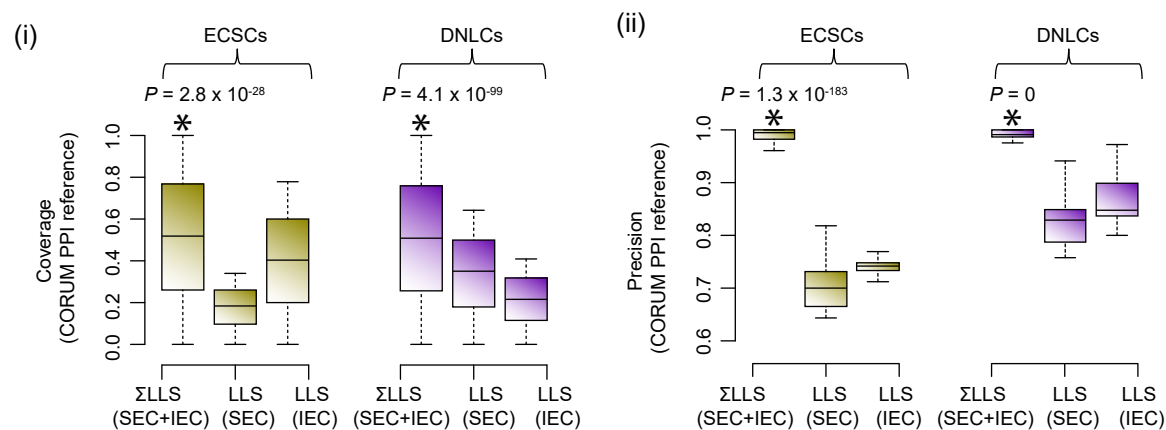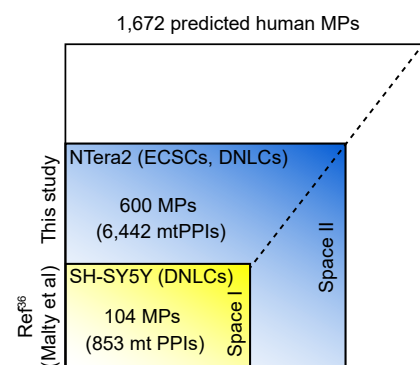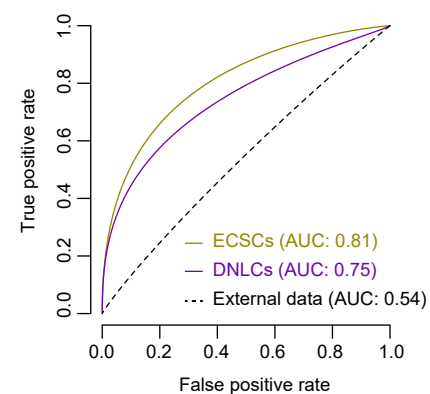
Figure S2. Co-elution profiles, scoring, and validating mtPPIs in ECSCs and DNLCs. Related to Figures 1-3 and Transparent Methods.

(A) Average correlation (peptide counts; ii) of replicate SEC- or IEC-MS analyses.

(B) Agreement of co-eluting proteins with molecular weights (kDa) or isoelectric points (pI) inferred from SEC (i) and IEC (ii) profiles.

(C) Coverage and accuracy of mtPPIs against reference CORUM complexes containing mt interacting proteins; *p-value (ΣLLS vs LLS scores from SEC or IEC) computed by Wilcoxon signed-rank test.

(D) Experimental scale-up (blue; space II) relative to our previous (yellow; space I) human mt proteins and interactions derived from SH-SY5Y neuronal cells (Malty et al., Cell Systems, 2017).

(E) Peformance measures of the true positive rate vs false positive rate using 5-fold cross validation is shown by comparing area-under-the ROC (AUC) for co-complex interactions detected in ECSC or DNLC networks against external data derived from large-scale studies (references cited in Fig 2B).
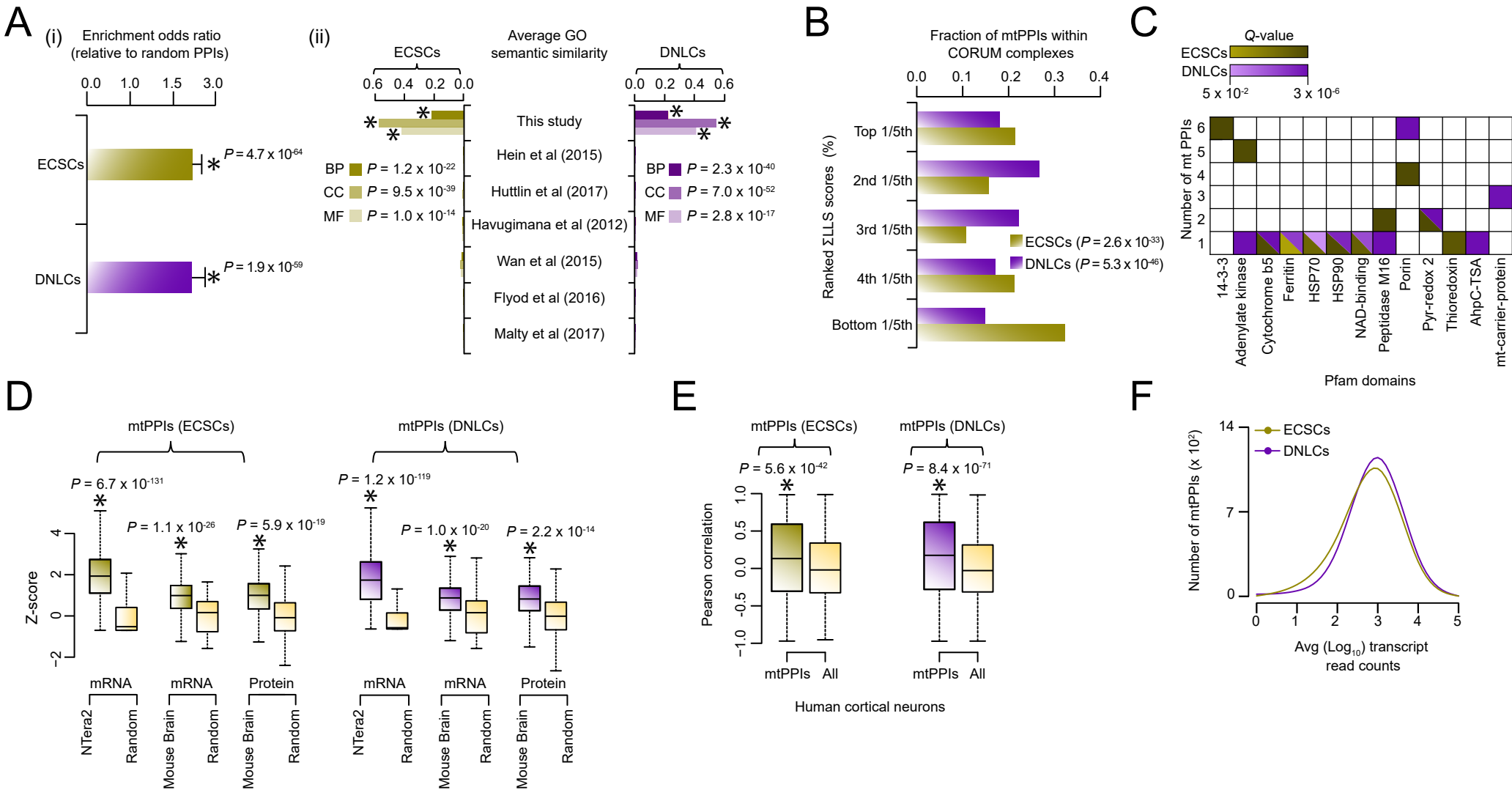
Figure S3. Benchmarking mtPPIs in ECSC or DNLC Network. Related to Figures 2-3 and Transparent Methods.

(A) Putative interacting proteins sharing phenotypic annotations (i) derived from MGI database (http://www.informatics.jax.org) of mouse orthologs compared to random set of protein interacting pairs, as well as to gene ontology (GO; ii) annotations (associated with BP, biological processes; CP, cellular components; and MF; molecular functions) compared to indicated large-scale PPI studies in ECSC or DNLC network. *p-value by Fisher's exact test (i) and Student's t-test (ii).

(B) MtPPIs in top or bottom 20th percentile of ranked ΣLLS scores from ECSC or DNLC network enriched within the CORUM protein complex; *p-values (top or bottom 20th percentile mtPPIs of ranked ΣLLS scores within CORUM complexes compared to randomly drawn PPI pairs) by Wilcoxon signed-rank test.

(C) Interacting proteins in ECSC or DNLC network enriched for shared Pfam domains (representative ones shown); False discovery rate (FDR; Benjamini-Hochberg correction) adjusted p-value (or Q-value) of the hypergeometric test.

(D) Box plots showing mRNA transcript and protein levels (Z-score transformed) of mtPPIs in ECSC or DNLC network vs randomly generated protein pairs (bootstrapped 1000 times) using RNA-seq (NCBI GEO: GSE52564; PMID: 25186741) and label-free quantification (PMID: 26523646) of mouse brain; *p-values by Wilcoxon signed-rank test.

(E) Correlation of mt interacting proteins in ECSCs or DNLC network vs all protein pairs co-expressed in human cortical neurons (NCBI GEO: GSE56796; PMID: 24991954); *p-values by Wilcoxon signed-rank test.

(F) MtPPIs in ECSC or DNLC networks is plotted against the mRNA transcript abundance derived from RNA-sequencing of Ntera2 ECSCs and DNLCs.
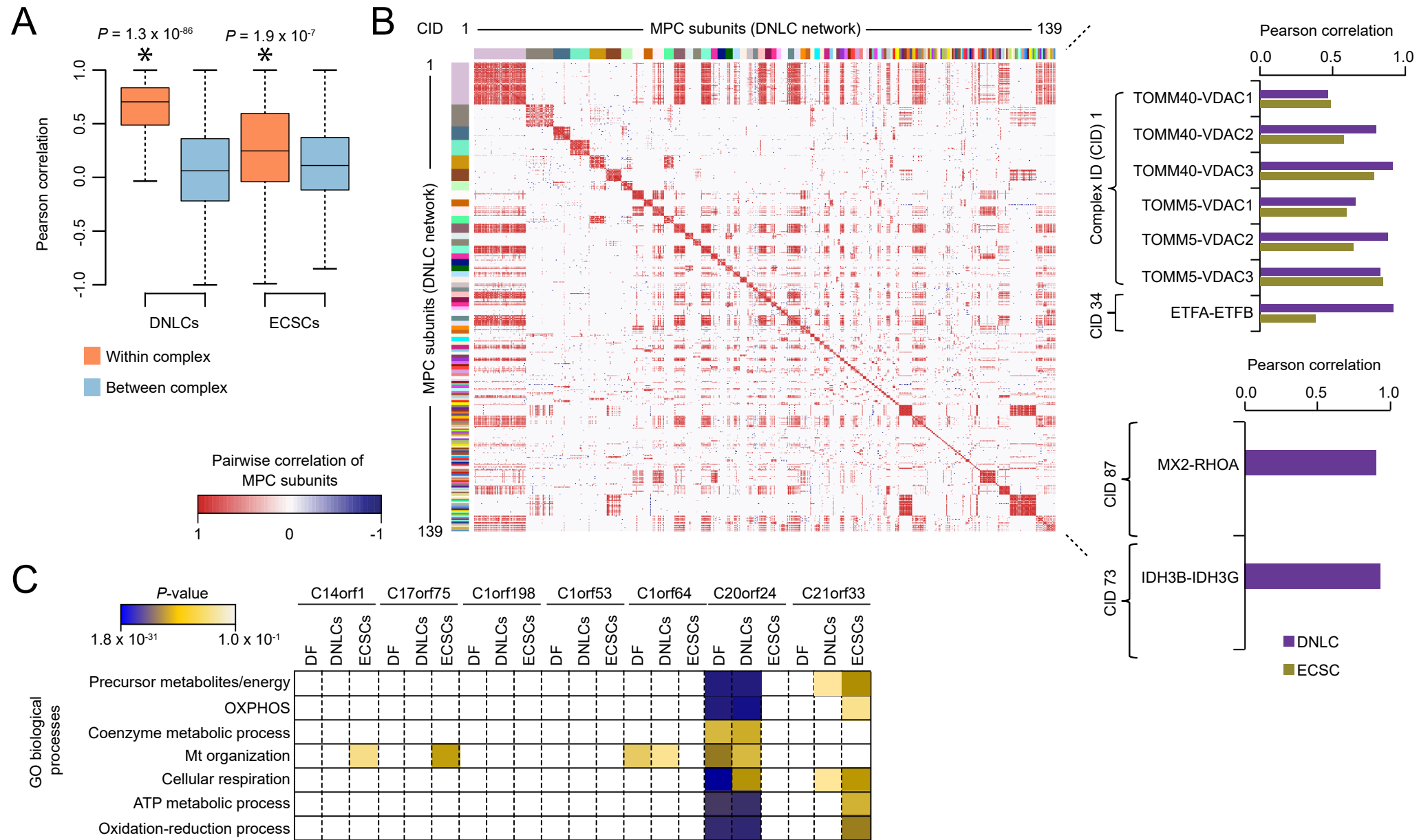
Figure S4. Evaluation of MPCs Predicted in DNLC Network. Related to Figures 2 and 3 and Transparent Methods.

(A) Scatterplot of representative hub proteins from the indicated process is shown based on connectivity with 50 or more MPs in either one of the static networks.

(B) Distribution of PPIs associated with orphan proteins and their overlap in static networks.

(C) Degree distribution (i) and seperation (ii) of interacting protein pairs in DNLC network.

(D) MPCs predicted by various clustering algorithms as indicated was compared against reference CORUM complexes; *p-value by Wilcoxon signed-rank test.

(E) Maximum overlap between predicted MPCs and reference set of CORUM complexes.

Figure S5. Evaluation of MPCs Predicted in Static and/or DF (Differential) Networks. Related to Figures 2 and 3 and Transparent Methods.

(A) Correlation of interaction profiles for proteins within and between complexes in ECSC and DNLC network; *p-value by Wilcoxon signed-rank test.

(B) Symmetrical heat map showing pairwise correlation of interacting proteins using their respective LLS score within the MPC predicted in DNLC network (left). Bar graphs (right) show correlated profiles for protein interacting pairs within the indicated cluster.

(C) Orphan association with proteins from ECSC, DNSC, and DF networks enriched in representative Gene ontology (GO) biological processes as indicated; p-value by hypergeometric test.
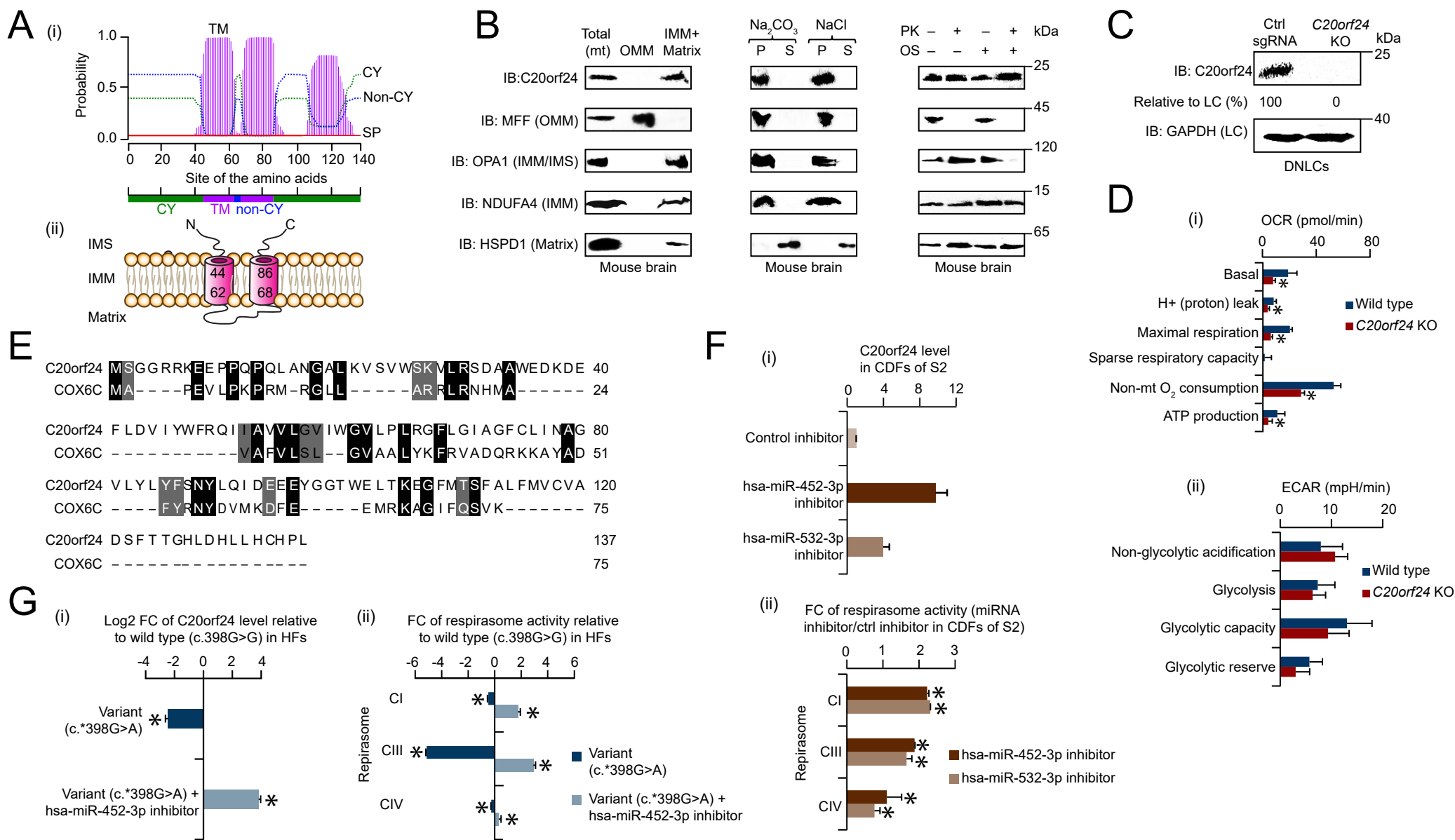
Figure S6. Characterization of C20orf24 and its Role in Respirasome. Related to Figure 5 and Transparent Methods.

(A) Transmembrane (TM) prediction for C20orf24 using Phobius (i) is shown with start and stop amino acid position of two transmembrane helix (ii) in the inner mt membrane (IMM); IMS, inter membrane space; SP, signal peptide; CY, cytoplasmic region.

(B) C20orf24 (along with mt compartmental markers as controls) in the indicated subcellular fractions of mouse brain, and in soluble (S) or membrane pellet (P) fraction of mouse brain extracts with NaCl or Na$_2$CO$_3$, as well as in the extracts of mouse brain treated with proteinase K (PK) in the presence of osmotic shock (OS) was immunoblotted (IB) using the indicated protein-specific antibodies; OMM, outer mt membrane.

(C) C20orf24 level in the control (ctrl) sgRNA and *C20orf24* CRISPR knockout (KO) of NTera2 DNLCs immunoblotted with anti-C20orf24 antibody. Band intensities normalized to GAPDH loading control (LC).

(D) Oxygen consumption rate (OCR, i) and extracellular acidification rate (ECAR, ii) measurements of KO and wild type cells; data represented as mean ± SD (n = 5 technical replicates; *$p \leq 0.05$ by Student's *t*-test).

(E) Amino acid sequence alignment of C20orf24 and COX6C using ClustalW software. Conserved sequences are shaded in black, while amino acid similarity groups (ILV, FWY, KRH, DE, GAS, TNQM) in grey.

(F, G) C20orf24 mRNA level and respirasome (Fold change, FC) activity measured by qRT-PCR or colorimetric assays in the CIV-deficient fibroblasts (CDFs) of subject 2 (S2, panel F) transfected with hsa-miR-452 or 532 miRIDIAN hairpin inhibitor vs. non-targeting miRIDIAN miRNA hairpin inhibitor control, or in healthy fibroblasts (HFs; panel G) transfected with variant (c.*398G>A) vs. wild type (c.398G>G), or variant (c.*398G>A) + hsa-miR-452-3p inhibitor vs. wild type (c.398G>G) or variant + non-targeting miRIDIAN miRNA hairpin inhibitor control (data shown for wild type c.398G>G); data represented as mean ± SD (n = 3-6 technical; *$p \leq 0.05$ by Student's *t*-test).
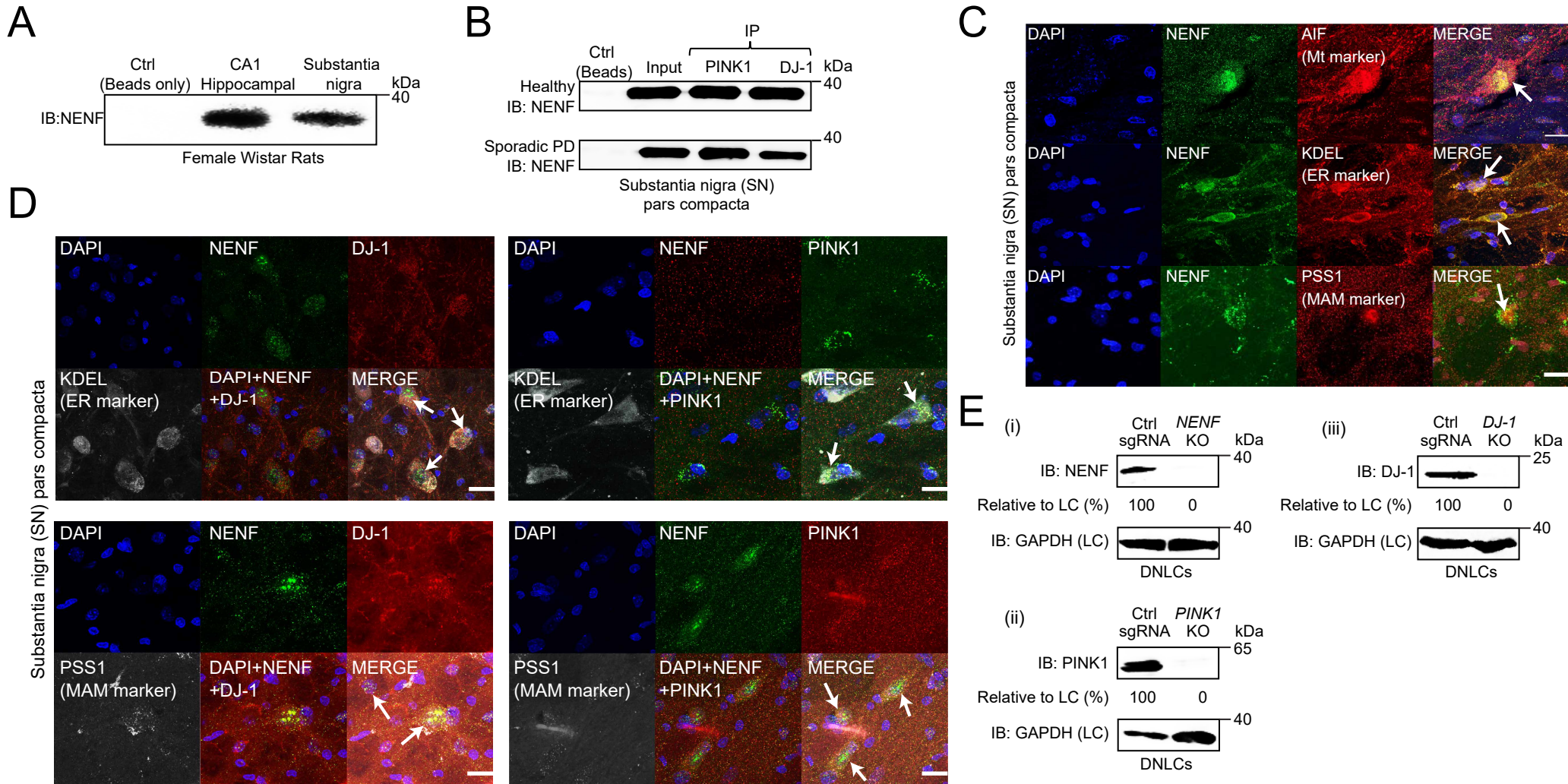
Figure S7. Characterization of NENF and its Association with DJ-1 and PINK1. Related to Figure 6 and Transparent Methods.

(A) Endogenous NENF level in the indicated brain regions of female Wistar rats; protein G beads alone (without antibody) served as negative control. Molecular masses (kDa) of marker proteins are indicated.

(B) PINK1 and DJ-1 immunoprecipitates (IPs) in the SN of healthy and sporadic PD patient using anti-PINK1 and DJ-1 antibodies were immunoblotted (IB) with anti-NENF antibody.

(C) Representative confocal micrographs of NENF localization (arrow heads) in the SN of rat brain using antibodies specific to NENF and indicated mt, ER, and MAM markers; DNA visualized by DAPI (blue), scale bar is 20 μm.

(D) Representative confocal micrographs of NENF colocalization (arrow heads) with DJ-1 and PINK1 in the SN of rat brain using antibodies specific to the indicated native proteins and ER or MAM markers; DNA visualized by DAPI (blue), scale bar is 20 μm.

(E) NENF (i), PINK1 (ii) and DJ-1 (iii) levels in the control (ctrl) sgRNA and indicated knockout (KO) of NTera2 DNLCs immunoblotted with anti-NENF, PINK1, or DJ-1 antibodies. Band intensities normalized to GAPDH loading control (LC).